ICFO - The Institute of Photonic Sciences
UPC - Universitat Politècnica de Catalunya

Single-atom motional dynamics in an optical dipole trap

Natália Domingues Alves

Supervisor: Prof. Dr. Morgan W. Mitchell

A thesis submitted in partial fulfillment for the
degree of Doctor of Philosophy

May 2023

"A trilha abri a facão, carne, osso e coração."

Pitty e Tassia Reis

Abstract

This thesis studies, using simulation and experiment, the motional dynamics of a single atom in an optical dipole trap. The optical dipole trap we study is a single-beam, red-detuned, far-off-resonance trap (FORT). This FORT is located at the centre of an arrangement of four high-NA lenses in the "Maltese cross" geometry, which facilitates measurements based on atomic fluorescence.

We make a detailed study, combining simulation with experimental measurements, of the temperature of the atom in this system. We note reasons why a single-temperature description could fail to describe the motional statistics of the atom in the trap. We then study the sensitivity of an established method, the release-and-recapture, to a possible anisotropic temperature distribution of the atom.

We also measure the extinction produced by the atom, from which we extract a lower bound on the strength of interaction. Finally, we show with simulation results and experiments, how parametric excitation of the atom in the FORT can be used to manipulate its phase-space distribution, which can lead to an effective decrease or increase of the atom's kinetic energy.

Resumen

Esta tesis estudia, mediante simulación y experimentos, la dinámica del movimiento de un solo átomo en una trampa de dipolo óptico. La trampa de dipolo óptico que estudiamos es una trampa fuera de resonancia (far-off-resonance trap, FORT) de un solo haz, desintonizado hacia el rojo. Esta FORT está ubicada en el centro de cuatro lentes de alta apertura numérica en la configuración "Maltese cross", que facilita las mediciones basadas en la fluorescencia del átomo.

Realizamos un estudio detallado, combinando simulaciones y experimentos, de la temperatura del átomo en este sistema. Señalamos las razones por las que el modelo del átomo con una temperatura única puede fallar al describir las estadísticas de su movimiento en la trampa. Además, estudiamos la sensibilidad del ya establecido método "release and recapture" a una posible distribución anisotrópica de la temperatura del átomo.

También medimos la extinción causada por el átomo, a partir de la cual extraemos un límite inferior de la fuerza de interacción. Finalmente, demostramos con resultados experimentales y de simulaciones, cómo la excitación paramétrica del átomo en la FORT puede ser utilizada para manipular la distribución de su espacio de fase, llevando a una disminución o aumento efectivo de su energía cinética.

Resum

Aquesta tesi estudia, mitjançant simulació i experiments, la dinàmica del moviment d'un sol àtom en un parany de dipol òptic. El parany de dipol òptic que estudiem és un parany fora de ressonància (far-off-resonance trap, FORT) d'un sol feix, dessintonitzat cap al vermell. Aquesta FORT està situada en el centre de quatre lents d'alta obertura numèrica en la configuració " Maltese cross" , que facilita els mesuraments basats en la fluorescència de l'àtom.

Realitzem un estudi detallat, combinant simulacions i experiments, de la temperatura de l'àtom en aquest sistema. Assenyalem les raons per les quals el model de l'àtom amb una temperatura única pot fallar en descriure les estadístiques del seu moviment en el parany. A més, estudiem la sensibilitat del ja establert mètode "release and recapture" a una possible distribució anisotròpica de la temperatura de l'àtom.

També mesurem l'extinció òptica causada per l'àtom, a partir de la qual extraiem un limiti inferior de la força d'interacció. Finalment, vam demostrar amb resultats experimentals i de simulacions, com l'excitació paramètrica de l'àtom a la FORT pot ser utilitzada per a manipular la distribució del seu espai de fase, portant a una disminució o augment efectiu de la seva energia cinètica.

Acknowledgements

First of all, I would like to thank my mom, Janayna, for having a lot of patience and supporting, in all possible ways, her only kid doing Physics far far away from home. To Morgan Mitchell, my advisor, who offered me the position that changed my life, thank you for believing in me. To my previous advisor, Daniel Felinto, who introduced me to Atomic Physics, thank you for giving me the opportunity to help build a lab from scratch.

To my dear lab mates, I'm grateful that we managed to build an environment where we feel acknowledged, valued and respected. And I am very glad that I could make friends for life that I had the honour and the pleasure to work with. You've made all the difference.

To all my friends and loved ones: all that I tried to write seemed wrong and not enough. You know who you are, and I'm extremely grateful for all you have done for me. I wouldn't be here today if it weren't for you. You've made me feel like I belonged somewhere by being my chosen family. Thank you for offering me physical and emotional shelter and welcoming me into your lives. Our *invisible string* will always be there, tying us together, wherever we are in the world.

List of publications

Lorena C. Bianchet, Natalia Alves, Laura Zarraoa, Tomas Lamich, Vindhiya Prakash, and Morgan W. Mitchell, Phys. Rev. Research **4**, L042026 (2022)

Bianchet LC, Alves N, Zarraoa L *et al.* Manipulating and measuring single atoms in the Maltese cross geometry [version 2; peer review: 2 approved]. Open Res Europe 2022, **1**:102 (https://doi.org/10.12688/openreseurope.13972.2)

Natalia Bruno, Lorena C. Bianchet, Vindhiya Prakash, Nan Li, Natália Alves, and Morgan W. Mitchell, "Maltese cross coupling to individual cold atoms in free space," Opt. Express **27**, 31042-31052 (2019)

Contents

To my mom, Janayna

Chapter 1

Introduction

1.1 Motivation and state-of-the-art

Light-matter interaction is a topic that has been extensively studied since the advent of the laser. Although radiation pressure has been known since Kepler's explanation for the fact that the tails of comets always point away from the sun, and Otto Frisch in 1933 was able to deflect an atomic beam of sodium using light from a sodium lamp [1], it was the laser that boosted this field. The laser enables a controlled interaction, in which light frequency, polarization, and power can be tailored to produce remarkable effects on matter. In 1970, Arthur Ashkin demonstrated the use of the optical dipole force to accelerate and trap micron-sized particles [2]. After this milestone, other proposals for using radiation pressure to confine atoms appeared, culminating in the work of Raab et al. [3], who, in 1987, reported the first magneto-optical-trap (MOT) for neutral sodium atoms.

Studies of individual trapped atoms began in the 1970s, with the work of Wolfgang Paul [4] and Hans G. Dehmelt [5, 6] on single trapped ions, which was recognized with the Nobel Prize in Physics in 1989. It wasn't until much later, in 2001, that the development of the optical dipole trap for single neutral

atoms started with Schlosser et al. [7], which demonstrated a diffraction-limited (numerical aperture, NA = 0.7) focusing objective inside a vacuum chamber that allowed for a sub-micrometer trap and fluorescence collection from a single ^{87}Rb atom. They later used this same system to trap two atoms in separate dipole traps and interfere the emitted photons [8], and also to manipulate a qubit stored in the atom [9]. The multi-lens objective was afterward replaced by a simpler system by Sortais et al. [10] that consisted of a single high-NA aspheric lens (NA = 0.5), and this new setup was used to show the coherent transfer of a qubit between two dipole traps [11].

In 2008, Tey et al. [12] implemented a system with two co-axial high-NA lenses aligned to a mutual focus, and reported a 9.8% extinction of a light beam by a single ^{87}Rb atom. The same group later studied single-atom-single-photon interaction and demonstrated that envelope tailoring of the single photons enabled precise control of the photon–atom interaction [13]. By illuminating coherently through both lenses, similarly to what is done in so-called 4π microscopy, the same group observed an extinction of 36.6% [14].

In the work of Nogrette et al. a similar setup was implemented, where they demonstrated single-atom trapping in two-dimensional arrays of microtraps with arbitrary geometries [15], that later allowed for a setup of single Rydberg atom arrays, opening the way to investigate the physics of spin systems with tens of particles [16].

Other groups, using similar systems, have reported the use of a standing-wave to trap a single Cesium atom [17]; investigation of state-dependent fluorescence in ^{87}Rb [18]; new cooling mechanisms that can be applied to a single atom in a dipole trap [19]; the near-complete control over all the internal and external degrees of freedom of two laser-cooled ^{87}Rb atoms trapped in two optical tweezers [20] and the entanglement of remote qubits using spin-exchange interactions [21].

Potential applications of these single-atom trapping techniques range from fundamental atomic physics and quantum optics to quantum technologies. In

single-atom quantum optics, interesting phenomena remain to be investigated, including the unconventional quantum correlations of light emitted by a single atom [22], the Hong-Ou-Mandel effect with a single atom as the beam-splitter and one- and two-photon processes such as stimulated emission.

Most of the previously shown configurations for the single-atom trap involved one or two high-NA lenses. The "Maltese cross" configuration, demonstrated by our group in [23] and used for the experiments in this Thesis, employs four lenses, one along each of the cardinal directions, positioned to have a mutual focus. Similar four-lens systems have been built both before [18] and after [24] ours. Interestingly, no two of these systems were aligned with the same method: [18] employed a reference sphere, [24] employed precision-machined lens-mounts, and our experiment employed wavefront measurements [23] to position the lenses for a diffraction-limited mutual focus. Although all of these systems have similar collection solid angles, and collect light emitted into four directions, to our knowledge our system was the first to demonstrate that this multi-axis collection can be diffraction limited when using a significant part of the lenses' numerical aperture [23].

1.2 Atom temperature

For both quantum science and quantum technology, the simplicity of the single trapped atom is one of its most appealing features. Typically, the internal state of the atom can be described by just a few discrete quantum observables, for example the hyperfine quantum number F and the magnetic quantum number m_F. The motional state of the atom is described by six continuous-valued observables, the position and momentum of the atom in three dimensions. A typical laser-cooled atom in a FORT has a mean energy far above the motional zero-point energy, meaning that many motional quantum states can be occupied. To avoid the complexities of describing this motion, it is common to 1) represent the motional state by a single number, a temperature, and 2)

treat the center of mass motion classically[1]. This preserves the simplicity of the atomic description, but also implies assumptions about the atomic motion, namely that it can be described statistically by a Boltzmann distribution.

At the same time, there are reasons to expect that a single laser-cooled atom in a FORT should not be described by an isotropic Boltzmann distribution. The reasons, discussed in greater detail in later chapters, derive from the lack of interaction of the atom with a macroscopic reservoir, and the asymmetry of the trapping and cooling processes. A portion of the thesis is thus dedicated to discussion of the concept of temperature itself, and its application to a single atom in an optical dipole trap.

The statistical distribution of the atom's position is important for many topics in single-atom science and technology. To name a few: 1) ac Stark shifts, proportional to the intensity of the FORT light at the position of the atom, cause position-dependent level shifts. Spectral line shapes and their interpretation thus depend on the atomic position distribution [25]. 2) The Rydberg blockade is used in quantum computation and quantum simulation with neutral atoms, and is based on dipole-dipole coupling at microwave frequencies. Movement of the atoms in their respective traps creates fluctuations in the strength of the dipole-dipole potential that can affect gate fidelity [26]. 3) Optical dipole-dipole coupling ordered atomic arrays, of interest for creating optical media with extraordinary properties not found in random media, is even more strongly dependent on atom position [27].

For these reasons, measurement of atomic temperature is important, and a great many single-atom experiments report a temperature. The most commonly used method is known as "release-and-recapture." We study the sensitivity of this technique to possible anisotropies in the position/momentum distribution. We'll also show how the motional dynamics of the atom in the

---

[1]With exceptions for techniques like sideband cooling, that are best described using quantized motional states.

trap can be manipulated and used for extra heating and cooling. The characterization of the strength of the light-atom interaction in our system will also be presented.

1.3   Thesis outline

The Thesis is organized as follows:

- In Chapter 2 the background theory is presented. Key concepts are explained, such as the main features of the atom used in the experiments described in this Thesis, ^{87}Rb; the brief overview on magneto-optical-traps; the optical dipole trap potential and light shifts; and finally the discussion regarding the concept of "temperature" in atom cooling and in particular for a single-atom in a dipole trap.

- In Chapter 3 the experimental setup is presented. We describe the implementation of the single-atom trap, including the Maltese cross configuration for the lenses, the magneto-optical-trap (MOT), the far-off-resonance trap (FORT), the locking of the cooler, repumper and FORT lasers. We describe a photon-counter implmented in arduino and explain the alignment for the collection of atom fluorescence from the four lenses.

- In Chapter 4 the temperature measurements and simulations are discussed. We present the available techniques, their implementation in our system, and show the limitations of the release-and-recapture technique.

- In Chapter 5 an extinction measurement is reported. The geometry, with linearly polarized FORT orthogonal to the applied bias magnetic field, is novel. We discuss its relation to the previously-studied geometry with parallel magnetic field, FORT circular polarization, and circular probe

polarization. This new geometry gives a lower limit of the light-atom coupling strength.

- In Chapter 6 the parametric excitation measurement and simulations are reported, where the modulation of the FORT power at twice the resonant frequency can be used for heating or cooling of the atom.

- Chapter 7 presents the conclusions and outlook of this Thesis.

Chapter 2

Background theory

Atom cooling and optical dipole traps have been extensively reviewed in the literature and textbooks [28–30]. In this Chapter we introduce the concepts that are pertinent and often appear in this Thesis, following the above-cited references. We also discuss the concept of "temperature" for a single-atom in a dipole trap.

2.1   Rubidium

In experimental atomic physics alkali metals are widely used. Their electronic structure with one valence electron allows a simple theoretical model for its energy levels, which follows similarly the level structure of hydrogen. Alkali metals also allow cycling transitions, which facilitates the implementation of atom cooling proposals by radiation pressure.

Rubidium (Rb) is an alkali metal with atomic number $Z = 37$. It is naturally found in two isotopes, ^{85}Rb (72.17%) and ^{87}Rb (27.83%), the first being stable. The lifetime of ^{87}Rb is 4.9×10^{10} yr, and this is the isotope used in the experiments described in this Thesis. Its mass is $m = 1.443\,161 \times 10^{-25}$ kg,

its nuclear spin is $I = 3/2$, and the transition hyperfine structure is shown in Figure 2.1.
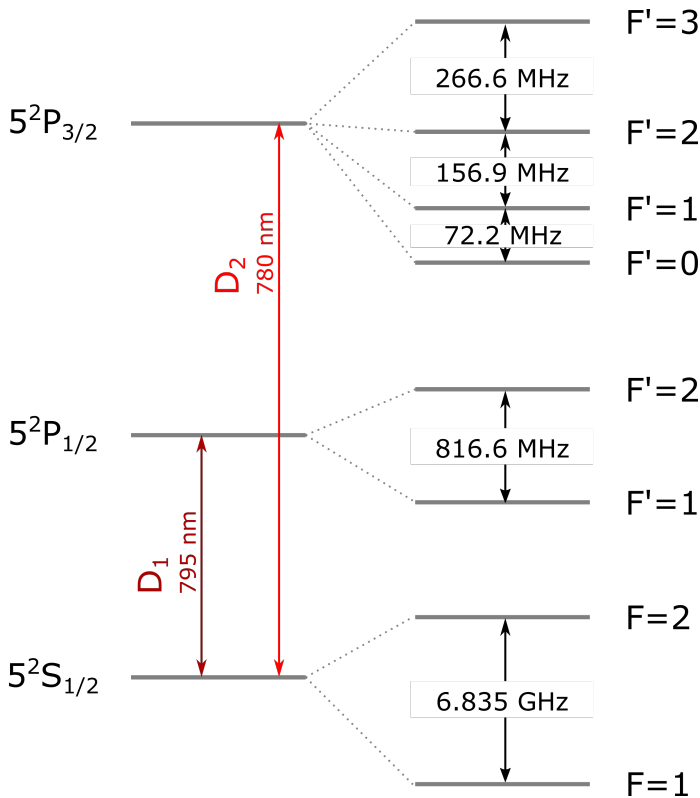
FIGURE 2.1: ^{87}Rb D_1 and D_2 transition hyperfine structures. Frequency values taken from [31].

2.2 The magneto-optical trap (MOT)

To have a single-neutral-atom trap is necessary to have a reservoir of cold atoms from which the trap can be loaded. The technique we employ to have such a reservoir is a magneto-optical trap (MOT). In the classic MOT geometry, which we use in our experiment, three pairs of red-detuned "cooler" laser beams propagate along the Cartesian axes. Along each axis, the beams counter-propagate, with opposite circular polarization, which leads to a velocity-dependent force directed opposite to the atom's direction of movement. A

quadrupole magnetic field is applied, which gives (in lowest order) a linear gradient around the point with zero field. By the Zeeman effect, the shift of the atom's internal energy levels will lead to a restorative force that will push it towards the zero of the magnetic field. By combining these two elements, light and magnetic fields, the MOT can cool and trap an ensemble of atoms.

2.3   The far-off-resonance trap (FORT)

Optical dipole traps generate a trapping potential using the interaction of a laser field with the oscillating electric dipole moment induced in the atom by that same field. In an approximation that is more accurate when the laser is farther off resonance, the resulting force can be described by a conservative potential proportional to the intensity of the driving laser field, plus a scattering force due to the (infrequent) scattering of laser photons by the atom. By choosing a proper beam shape, this interaction can be used to create a tight trap potential. For a far-detuned laser field (far-off-resonance trap, FORT), the effective potential and the scattering rate are given by

$$U_{\text{FORT}}(\mathbf{r}) = \frac{3\pi c^2}{2\omega_0^3} \frac{\Gamma}{\Delta} I(\mathbf{r}), \tag{2.1}$$

$$\Gamma_{\text{sc}}(\mathbf{r}) = \frac{3\pi c^2}{2\hbar\omega_0^3} \left(\frac{\Gamma}{\Delta}\right)^2 I(\mathbf{r}), \tag{2.2}$$

where $\mathbf{r} = (x, y, z)$, c is the speed of light, ω_0 is the two-level transition frequency, Γ is the natural linewidth of the two-level transition, $I(\mathbf{r})$ is the light intensity and $\Delta = \omega - \omega_0$ is the detuning from the laser field frequency ω [30].

By tightly focusing a single far-red-detuned Gaussian beam, one creates a potential well where atoms can be confined[1]. In this scenario, the intensity

---

[1]In the experiment described in this Thesis, only one atom is confined, and the reason will be explained in the next Section.

distribution $I(x, y, z)$ is given by

$$I(x, y, z) = \frac{2P}{\pi w^2(z)} \exp\left[-2\frac{x^2 + y^2}{w^2(z)}\right], \tag{2.3}$$

where P is the total power of the beam,

$$w(z) \equiv w_{\text{FORT}}\sqrt{1 + \left(\frac{z}{z_R}\right)^2}, \tag{2.4}$$

w_{FORT} is the beam waist defined as the $1/e^2$ radius of intensity and $z_R = \pi w_{\text{FORT}}^2/\lambda$ is the Rayleigh range, with λ the wavelength of the FORT. For practical values of w_{FORT}, the FORT potential is tighter in the radial direction (x, y) than in the longitudinal one (z), as illustrated in Figure 2.2.

The same field-dipole interaction used to trap the atoms also introduces a shift in the internal energy levels of the atom: the ac Stark shift. For a two-level atom, the ground state ac Stark shift shift is $\Delta E = U_{\text{FORT}}$, and the excited state shift is $\Delta E = -U_{\text{FORT}}$, meaning that if the ground state experiences a trapping potential, the excited state experiences an anti-trapping potential. For ^{87}Rb, which is not a two-level atom, the ground state ac Stark shift coefficient can be calculated from second-order perturbation theory [32] or using Floquet methods [33]. Both values are present in this Thesis, denoted by β' and β, respectively. If we assume the latter, the trapping potential can be written as

$$U_{\text{FORT}}(x, y, z) = \beta\frac{2P_{\text{FORT}}}{\pi w^2(z)} \exp\left[-2\frac{x^2 + y^2}{w^2(z)}\right], \tag{2.5}$$

where $\beta \approx -6.39 \times 10^{-36}\,\text{Jm}^2\text{W}^{-1}$ for $\lambda = 852\,\text{nm}$.

A common approximation that is done for the trapping potential is called the harmonic approximation: if $k_B T_{\text{atom}}/U_{\text{FORT}}(0, 0, 0) \ll 1$, meaning that the thermal energy of the atom $k_B T_{\text{atom}}$ (k_B is the Boltzmann constant and T_{atom} is the atom's temperature, to be discussed later), is much less than the potential depth, we can assume that the atom only explores the bottom of the
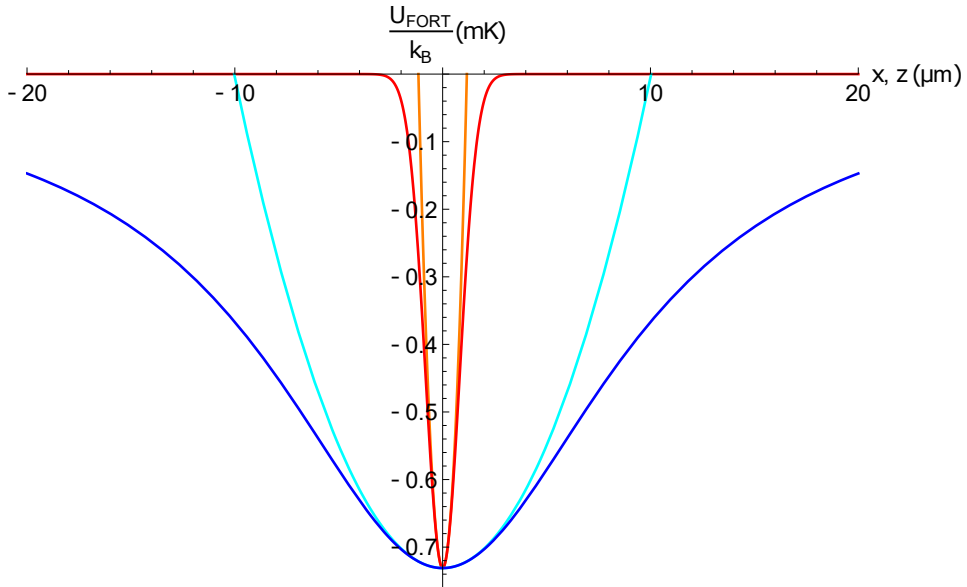
FIGURE 2.2: The FORT potential in mK as a function of position (x, z) for its true function (red and blue, respectively) and the harmonic approximation (orange and cyan, respectively), for $P_{\text{FORT}} = 7.0\,\text{mW}$, $w_{\text{FORT}} = 1.65\,\mu\text{m}$ and $\lambda = 852\,\text{nm}$.

FORT potential, and therefore we can expand U_{FORT} in a power series and take the second order approximation, which leads to the FORT potential

$$U_{\text{FORT}}(x, y, z) \approx U_0 \left[-1 + 2\frac{x^2 + y^2}{w_{\text{FORT}}^2} + \frac{z^2}{z_R^2} \right], \tag{2.6}$$

where $U_0 = -U_{\text{FORT}}(0, 0, 0)$. The trap depth is often given in temperature units, i.e., as $T_{\text{FORT}} = U_0/k_B$.

This harmonic approximation of the FORT potential is thus the sum of a constant $-U_0$ and harmonic oscillator potentials $U(x) = m\omega_\perp^2 x^2/2$, $U(y) = m\omega_\perp^2 y^2/2$ and $U(z) = m\omega_\parallel^2 z^2/2$. The atom will have two frequencies of oscillation, one parallel to the propagation axis of the FORT, $\omega_\parallel$ (longitudinal), and one perpendicular to it, $\omega_\perp$ (transverse), that can be written as

$$\omega_\perp = \sqrt{\frac{2U_0}{mz_R^2}}, \quad \omega_\parallel = \sqrt{\frac{4U_0}{mw_{\text{FORT}}^2}}, \tag{2.7}$$
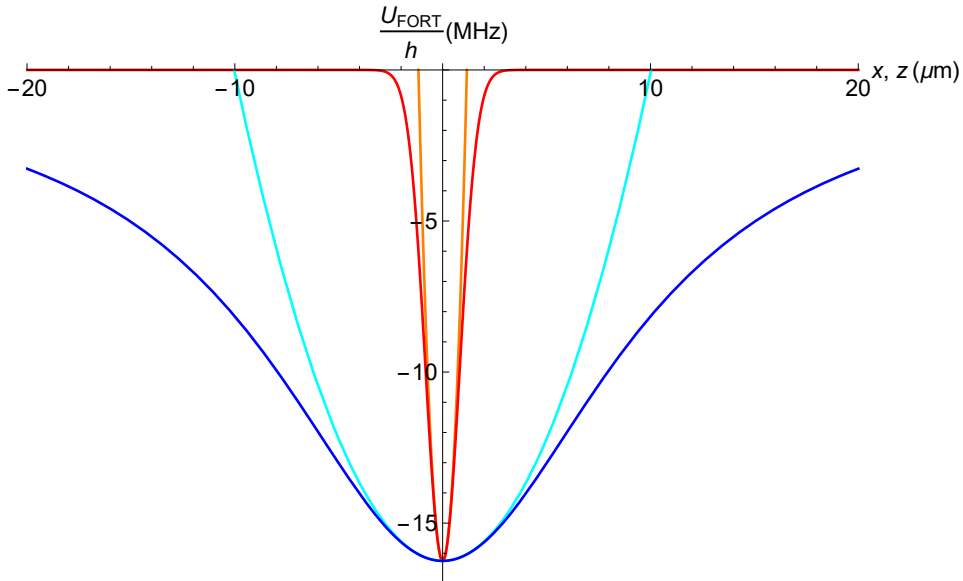
FIGURE 2.3: The FORT potential in MHz as a function of position (x, z) for its true function (red and blue, respectively) and the harmonic approximation (orange and cyan, respectively), for $P_{\text{FORT}} = 7.1\,\text{mW}$ and $w_{\text{FORT}} = 1.65\,\mu\text{m}$.

where m is the ^{87}Rb mass.

2.3.1 The single-atom trap: light-assisted collisions

By tightly focusing the FORT beam, to a size comparable to its wavelength, and having the FORT being illuminated by a red-detuned near-resonant light, we can achieve a "collisional blockade" regime [34] where light-assisted collisions (LACs) [35] guarantee, at any given time, either the presence of one or no atom in the FORT. The reason for this is the following: if two atoms enter the FORT, and both are in the ground state S, they interact via the van der Waals potential $V \sim -1/r^6$ (where r is the interatomic distance). However, due to the presence of the near-resonant red-detuned light, one of the atoms can get excited to the P state, which will cause the two atoms to form a loosely bound pair with one atom in the S state and the other in the P state. This leads instead to an interaction through the long-range dipole-dipole attractive
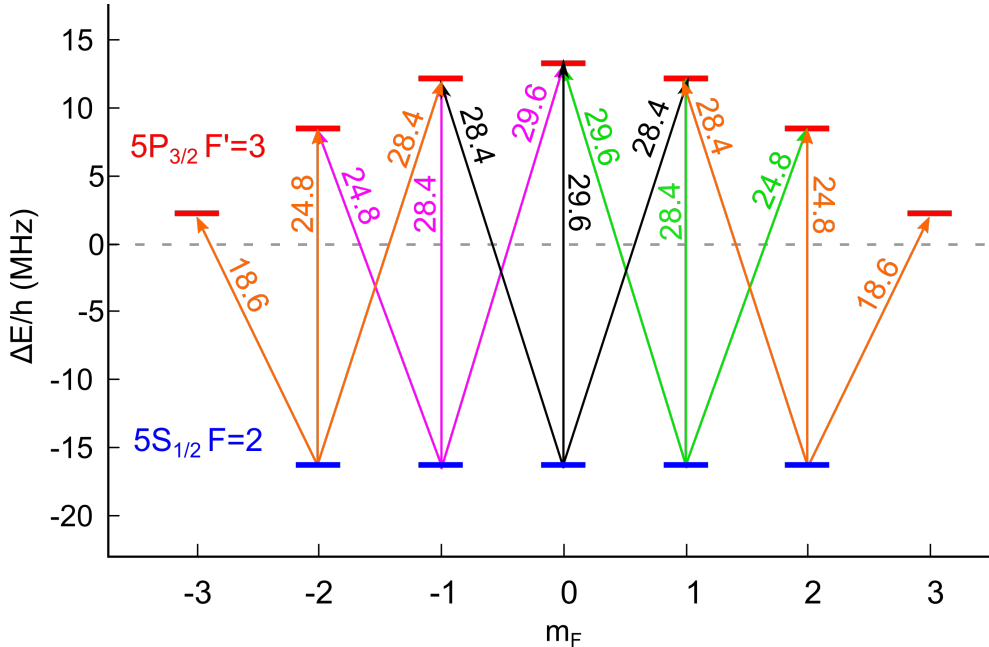
FIGURE 2.4: Energy level shifts of the ground $F = 2$ and excited state $F' = 3$ of ^{87}Rb D_2 line caused by the ac-Stark shift, computed as in [33] for our typical FORT configuration $P_{\text{FORT}} = 7.1\,\text{mW}$ and $w_{\text{FORT}} = 1.65\,\mu\text{m}$, linearly polarized. Arrows indicate the blue shift in MHz of the $|F = 2, m_F\rangle \rightarrow |F' = 3, m_{F'}\rangle$ transitions. Quantization axis along the polarization direction of the FORT beam.

potential of the form $V \sim -1/r^3$. The difference of energy ΔE, showed in Figure 2.5, that the pair experiences, before it decays to the ground state, can cause it to gain enough kinetic energy that exceeds the FORT depth U_0, thus leading to the loss of both atoms and guaranteeing that we have only a single atom in the FORT.

2.4 The concept of temperature in cold atom systems

A large part of this Thesis concerns the temperature of single trapped atoms and the measurement of these temperatures. In macroscopic systems, temperature is an intuitive concept that has been given a rigorous formulation
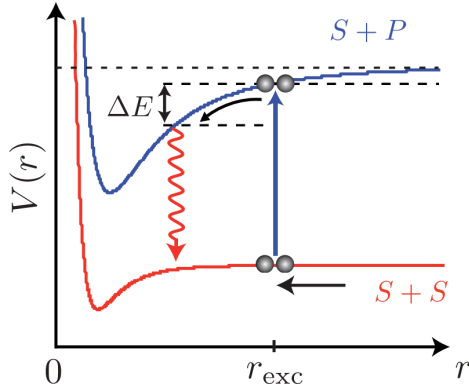
FIGURE 2.5: The LACs process scheme, details in the text. Reproduced from [35].

in the theories of thermodynamics and statistical physics. The situation is not so clear for microscopic systems such as single atoms. Nonetheless, the concept of temperature is useful and very widely used. In this section I make several observations about temperature and its applicability in the context of single-atom experiments.

2.4.1 Thermodynamic temperature

Temperature is a basic concept in statistical mechanics and thermodynamics, and strictly speaking is only defined for systems in equilibrium. Macroscopic systems reach an internal thermal equilibrium by sharing energy and entropy among many degrees of freedom. The resulting state is characterized by a temperature, which is defined as the partial derivative of the internal energy with respect to the entropy. This formulation of temperature implies, among other things, that heat will flow only from hotter objects to colder ones, because flow in the reverse direction would reduce the net entropy, in violation of the second law of thermodynamics. A microscopic system in thermal contact with a macroscopic system (a "bath") will also reach an equilibrium characterized by a temperature, which will be equal to the temperature of the bath [36].

At equilibrium, the probability distribution for the energy of the microscopic system will be described by the Boltzmann distribution. In a quantum mechanical description, the corresponding state is described by a density matrix

$$\rho = \mathcal{Z}^{-1} e^{-H/k_B T} \tag{2.8}$$

where H is the Hamiltonian, T is the temperature, k_B is the Boltzmann constant, and $\mathcal{Z}$ is a normalization constant known as the partition function. In a classical description, the system will be described by a phase-space probability distribution with a density function given by

$$f(\mathbf{q}, \mathbf{p}) = \mathcal{Z}^{-1} e^{-H(\mathbf{q},\mathbf{p})/k_B T} \tag{2.9}$$

where $\mathbf{q}$ is a vector of coordinates, and $\mathbf{p}$ is the vector of corresponding conjugate momenta. The probability for the system to be found in a small region of size $d^n q \, d^n p$ around $(\mathbf{q}, \mathbf{p})$ is $f(\mathbf{q}, \mathbf{p}) d^n q \, d^n p$.

2.4.2 "Temperature" of optical molasses

It is common in many contexts of cold atom physics to encounter a "temperature" for an atom or a collection of atoms. In some circumstances, for example ensembles of atoms held in a conservative potential and interacting by elastic collisions [37], the atomic system does have many coupled degrees of freedom and can in fact reach equilibrium. In such situations, the classical concept of temperature applies, just as it does to classical gases. In contrast, a single trapped atom has only a few degrees of freedom, and in most circumstances is not in thermal equilibrium with a reservoir. In such situations, there is no temperature in the orthodox sense described above. Nonetheless, the statistical properties of an atom can often be correctly inferred from a "temperature," in the sense of the parameter in a Boltzmann or Maxwell-Boltzmann distribution. One important and early example is optical molasses [38], in which atoms experience optical cooling forces in the absence of trapping forces. The

logic behind assigning a "temperature" in this situation is described by Lett
et al, which reviewed the understanding of optical molasses in 1989 [39]:

> One may ask whether a laser-cooled atom or collection of atoms
> can be said to have a temperature. Normally one considers a sys-
> tem with a temperature to be in equilibrium with a reservoir, and
> in this case the identity of that reservoir is not clear. Even if there
> are many atoms, they do not interact with one another but only
> with the radiation field. The radiation field, including the vac-
> uum, may in some sense be a reservoir, but the sense in which
> this may be true has not been made rigorous. Nevertheless, it
> can be shown [F. Reif, Fundamentals of Statistical and Thermal
> Physics (McGraw-Hill, New York, 1965)] that the solution of the
> Fokker–Planck equation for a system acted on by a friction force
> proportional to velocity ... and with a random noise input in-
> dependent of velocity, such as is provided by the random nature
> of photon absorption and emissions in the small recoil limit, is a
> Maxwell–Boltzmann distribution. Furthermore, our own Monte
> Carlo simulations of the laser-cooling process for a single atom, in
> which every emission and absorption is treated as a random event,
> leads to a Maxwell–Boltzmann distribution, when averaged over
> time... For this reason, we believe that we are justified in saying
> that even a single Doppler-cooled atom, under the conditions of
> small recoil velocity and small thermal velocity, has a tempera-
> ture.

The small-velocity conditions referred to in the above quote can be found in
Dalibard et al. [40], which provides simple models of 1D polarization-gradient
cooling [2]. These early works also suggest that a 3D molasses should be char-
acterized by a single "temperature," and thus with a momentum distribution

---

[2]The conditions are, more precisely: the atom's velocity $v_{atom} \ll \Gamma/k$, where Γ is the Ein-
stein A coefficient, $k = 2\pi/\lambda$, and λ the transition wavelength, and low saturation parameter
[40].

that is isotropic, if the cooling is provided by beams with equal detuning and intensity along the three Cartesian axes.

More recent works describe how non-Maxwell-Boltzmann velocity distributions can arise in laser cooling [41, 42], and stress that that isotropic momentum distributions are only expected for low velocities ($v \ll \Delta/k$, where $\Delta = \omega - \omega_0$ is the detuning from the resonance) [43]. An analysis of the time evolution of the velocity distribution for the 1D non-saturated case is given in [44], which shows that even if initially Gaussian, the velocity distribution evolves to become non-Gaussian. There have been observations of non-Gaussian velocity distributions in laser-cooled atoms and proposals for other velocity distribution functions [45, 46] . To our knowledge, there have been no studies of the precise velocity distribution for atoms in a 3D molasses in the σ^+-σ^- configuration with significant saturation of the cooling transition, which is the most common case for experiments.
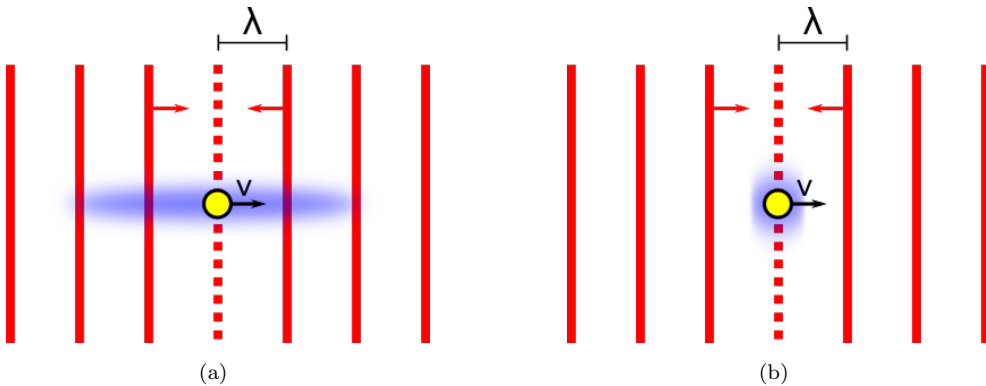

FIGURE 2.6: Wavefronts of cooler beams (in solid red) and the atom (in yellow) moving towards the right and the constraint on its movement (blue area) for the longitudinal (a) and transverse (b) motion.

2.4.3 "Temperature" of a laser-cooled atom in a single-beam FORT

As just described, the velocity distribution of a laser-cooled atom in free space is already a fairly complex problem that may or may not lead to Gaussian distributions accurately described with a "temperature." The situation becomes still more complex when the atom is trapped. Trapping implies some kind of restoring force, and thus a coupling between position and momentum degrees of freedom. In practice, nearly all traps are spatially anisotropic, which then suggests that the momentum distribution may also become anisotropic. We thus expect to find different statistical distributions (and if these are Gaussian, different "temperatures") for different momentum components.

To illustrate this in the context of our experiments, we consider a strongly-focused single-beam FORT like that described in chapter 3, and consider how the anisotropic trap shape can influence the laser cooling mechanisms that determine the momentum distribution.

The FORT is formed by a circular Gaussian beam with wavelength $\lambda = 852\,\mathrm{nm}$ and beam waist $w_0 = 1.65\,\mu\mathrm{m}$, and thus Rayleigh range $z_R = \pi w_0^2 / \lambda \approx 9.4\,\mu\mathrm{m}$. At a power of $7.1\,\mathrm{mW}$ the longitudinal and transverse trap frequencies are $\omega_\parallel = 2\pi \times 6\,\mathrm{kHz}$ and $\omega_\perp = 2\pi \times 51.4\,\mathrm{kHz}$, respectively. Considering a typical sub-Doppler cooling temperature of $T_{\mathrm{atom}} = 37\,\mu\mathrm{K}$ and making the harmonic approximation for the trapping potential, a Boltzmann-distributed position has r.m.s. widths[3] of $\sigma_x = \sigma_y \approx 0.2\,\mu\mathrm{m}$ in the radial directions (x and y) and $\sigma_z \approx 1.6\,\mu\mathrm{m}$ in the longitudinal direction (z).

The cooling lasers are pairs of counter-propagating beams with a σ^+-σ^- polarization scheme. Considering just one pair for the moment, these produce a corkscrew of linear polarizations with a spatial period of $\lambda/2 \approx 0.4\,\mu\mathrm{m}$. For an atom with a typical thermal energy, it is thus possible to travel by multiple polarization periods along the longitudinal direction, whereas for the same atom

---

[3]The given values are standard deviations of the Maxwell-Boltzmann distribution: $\sigma_x = \sigma_y = \sqrt{k_B T_{\mathrm{atom}}/m\omega_\perp^2}, \sigma_z = \sqrt{k_B T_{\mathrm{atom}}/m\omega_\parallel^2}$.

this is not possible in the transverse direction. This is illustrated in Figure 2.6. We may thus expect that cooling mechanisms such as Doppler cooling [47] and polarization-gradient cooling [40], each of which requires sustained motion on the scale of the optical standing wave, could act differently on the longitudinal and transverse directions.[4]

A second reason to expect an anisotropic momentum distribution comes from the theory of optical dipole forces. The optical dipole force arises due to intensity-dependent light shifts [48]. For red-detuned trapping light, as in the FORT, this light shift is toward lower energies for the $5S_{1/2}$ ground states, but toward higher energies for the $5P_{3/2}$ excited states involved in the cooling transition. So, while the FORT light produces a trapping potential for the ground states, it also produces for the excited states an anti-trapping potential, i.e., a force away from the center of the trap [49, 50]. If the atom spends some time in the excited state, for example due to excitation by the FORT light [48] or by cooler light [51], the time spent in the excited state both alters the mean restoring force, and makes it noisy. The latter effect is known as dipole force fluctuations (DFF) [52]. Both effects can be explained qualitatively if the atom spends a fraction of its time on the anti-trapping potential, with the precise timing of transitions between the two potentials determined by a combination of coherent processes, e.g. laser-driven Rabi oscillation, and stochastic processes, e.g. spontaneous emission.

An interesting characteristic of DFF is that it adds noise along the optical gradient, which is to say, parallel to the trapping force. Because the optical gradient is much stronger along the radial directions than along the longitudinal direction, this is a second way in which trap anisotropicity can produce an anisotropic momentum distribution.

---

[4]Other phenomena could also lead to a disturbance in the cooling process, such as aberrations on the FORT beam, but will not be discussed in this Thesis.

Chapter 3

Experimental setup

The single-atom is trapped by means of a far-off-resonance trap (FORT). This FORT, at 852 nm, is loaded stochastically from a small atomic cold cloud of ^{87}Rb provided by a magneto-optical-trap (MOT). Unlike other single-atom trap configurations [53–55] which have one or two lenses, ours has four lenses, which doubles the available solid angle and is versatile for experiments that require new access and collection angles. The experiments described in this thesis use an experimental system that was constructed starting in 2016, and is described in two journal publications [23, 56] and a PhD thesis [57]. In this Chapter, we give brief descriptions of each component of the system, and also provide additional details, including the alignment process for the FORT and the MOT, the layouts of optical setups for laser stabilization, the construction of a photon-counter based in an Arduino Due board and the lenses path alignment.

3.1 The Maltese cross four-lens configuration

The starting point of the experimental setup is the four-lens system geometry developed mainly by Dr. Natalia Bruno in 2017 and published in [23]. This

system has four high Numerical Aperture (NA=0.5) lenses in the cardinal directions aligned to a mutual focus in a configuration that we call the *Maltese cross*. They were glued to a Macor base (a type of ceramic) and the alignment procedure, described in [23] and [57], accomplished high-NA common diffraction-limited foci, see Figure 3.1. The lenses are anti-reflection coated to cover the wavelengths used in the experiments, namely, 780 nm, 795 nm and 852 nm. Similar setups were realized in [24, 58].
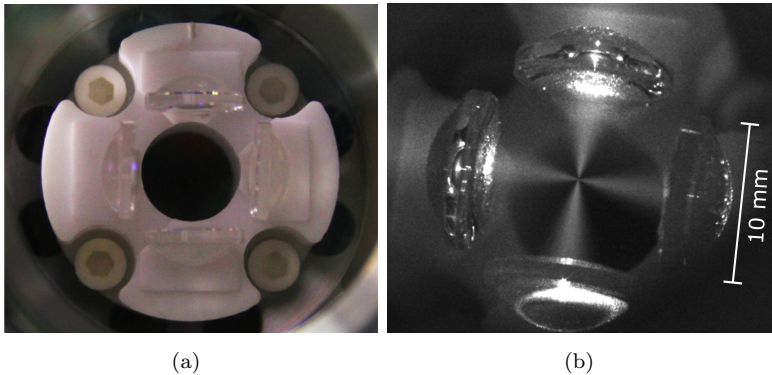

(a)   (b)

FIGURE 3.1: The Maltese cross configuration. (a) Top view: The four lenses are glued to the Macor base following the procedure described in [23]. (b) Top view: The Maltese cross name comes from the fluorescence pattern in the Figure above when 780 nm resonant light is sent through two orthogonal lenses while the vacuum chamber is filled with ^{87}Rb vapor. Reprinted with permission from [23] ©Optica Publishing Group.

The placement of the four-lens system inside the UHV (ultra-high vacuum) chamber defines the coordinates used to describe the system in this thesis, as can be seen in Figure 3.2. For more details on the UHV chamber and the vacuum system, see [57].

3.2   The far-off-resonance trap (FORT)

The far-off-resonance trap (FORT) we employ is at 852 nm, for which we use a distributed feedback laser DFB (Toptica Eagleyard EYPDFB0852), frequency locked to the D2 line of ^{133}Cs, specifically the transition $6^2S_{1/2}, F = 4 \rightarrow$
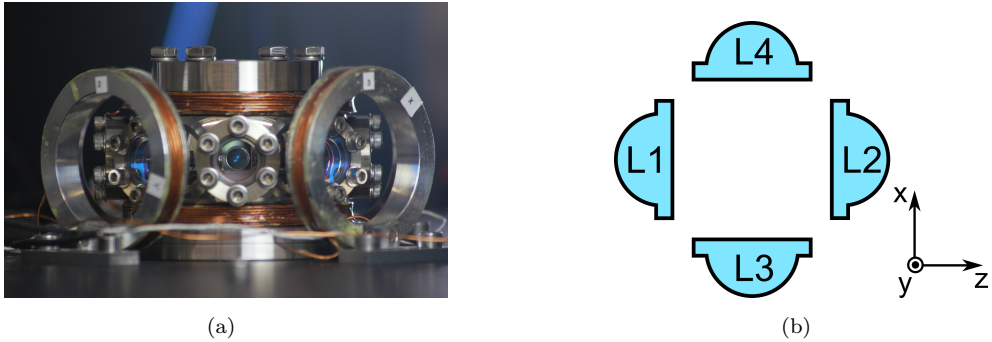
FIGURE 3.2: (a) The four-lens system placed inside the UHV chamber with the MOT magnetic field compensation coils surrounding the former. (b) Definition of the coordinate system for the Maltese cross configuration. Gravity is in the negative y direction.

$6^2P_{3/2}, F' = 5$, using the modulation transfer spectroscopy (MTS) technique[1] [59], and its polarization is vertical.

Once the four-lens system is placed inside the vacuum chamber, we have the reference for the FORT alignment. The FORT has five parameters for alignment: position and direction (for both vertical and horizontal directions) and divergence angle (focusing position). The first (see Figure 3.4a), which is for the beam to pass straight through the center of L1 and L2, is set with the help of the shearing interferometer (SI) and two cameras, the top camera (shows the image of Figure 3.4b, Blackfly BFLY-PGE-03S2M, fixed) and a non-fixed camera (Thorlabs DCC1545M-GL) that we place before the second dichroic mirror (see Figure 3.3). The first image shows us roughly if the beam is passing through L1 (by the scattering it could have in the ceramic base) and the second if it's being cropped by L1 or L2 (the image of the beam should be a clean gaussian profile without any cropping from the lens' edge). By doing beam walking with the two mirrors before the first dichroic mirror, the beam is roughly aligned to pass through the center of both of these lenses. After this, we check with the SI (see Figure 3.5, right) if the beam has any aberrations, which would be translated as a wavy pattern in the image, if it has, we do fine alignment with beam walking and again check that the beam is not being

---

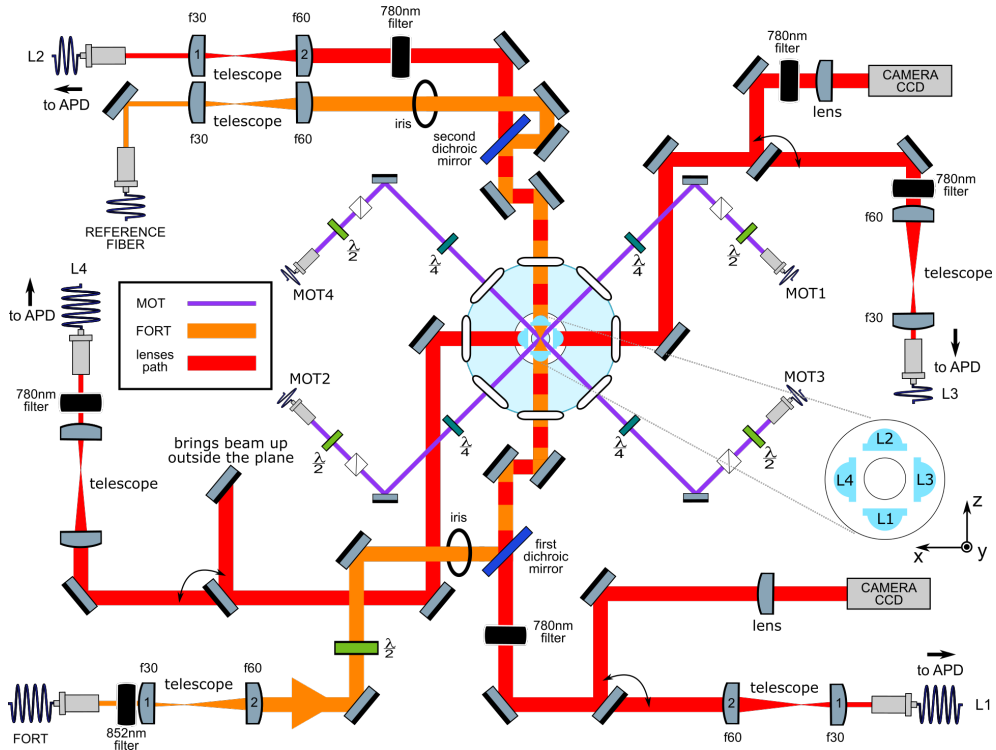[1]Explained for the cooler laser in Section 3.3.1.1.

FIGURE 3.3: Optical setup for the main part of the experiment, with the UHV chamber and the four-lens system placed inside it. Magneto-optical-trap beams (in purple) pass through the gaps in between the lenses. The far-off-resonance trap (FORT) beam is increased in size by a telescope and its polarization is set to be vertical. The FORT beam shares its optical path with the 780 nm light collected from L1 and L2, and they are frequency split by dichroic mirrors (Semrock FF825-SDi01). $\lambda/2$ stands for half-waveplate and $\lambda/4$ quarter-waveplate. Cubes are polarizing beamsplitters (PBS). Fiber collimators/couplers Schäfter+Kirchhoff 60FC-4-M15-02. Filter: bandpass filters centered in the indicated wavelength. APD: avalanche photodetector. MOT 5 and 6 (positive and negative propagation y direction, respectively) not shown.

cropped by the lenses. This process is done iteratively until the fringes are straight as possible. Another option is to center the FORT beam to both irises that are placed on its path, again, making use of the non-fixed camera and the mirrors before the first dichroic mirror. This alignment holds for weeks in typical laboratory working conditions.

The divergence angle is set by a telescope (see Figure 3.3, in front of the FORT
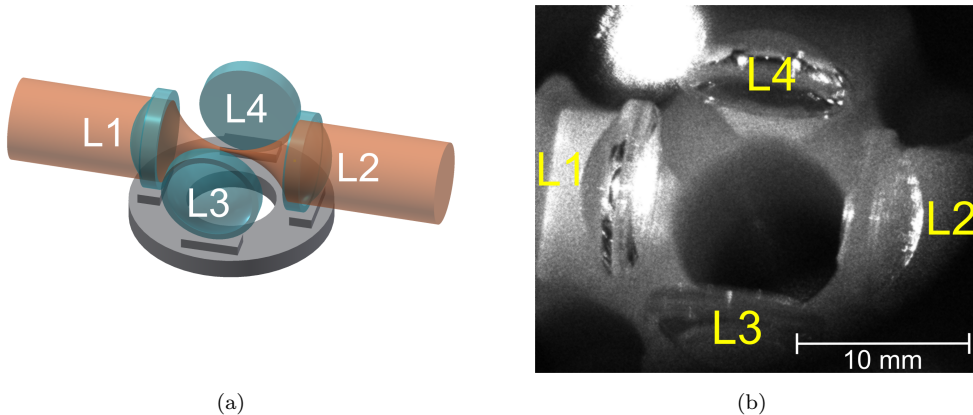
FIGURE 3.4: (a) Illustration of the four-lens system glued to a base and the FORT beam (in orange). (b) Representative image from the top camera that shows the bright FORT beam passing through the middle of L1, which we use as a reference for the first step of its alignment.

collimator) with the help of the SI and the non-fixed camera (see Figure 3.5). With the image of the non-fixed camera, it's possible to see the typical SI fringes that shows if the beam is convergent, divergent or collimated, depending on its tilt. It also shows the presence of spherical aberrations, seen as curvatures of the fringes (wavy pattern). Due to the fact that the lenses were commercially made to collimate a laser beam, they were designed to be diffraction limited when collimating the light emitted by a laser that is behind a glass window. Since no window exists in our geometry, we need to send a slightly convergent beam to eliminate the spherical aberration that appears in the focus spot if we send a collimated beam. For this, the angles in the SI image (measured as the yellow angle on the SI image of Figure 3.5) need to be set equal and opposite by moving the second lens of the telescope. The waist of the beam (at $1/e^2$ intensity level) at the lens position is $w_{\text{lens}} = 1.85 \, \text{mm}$, measured by fitting its intensity profile in the non-fixed camera (propagated outside the UHV chamber by the same distance it would propagate to reach L1) to a gaussian, and the typical power used for the FORT is $7 \, \text{mW}$.
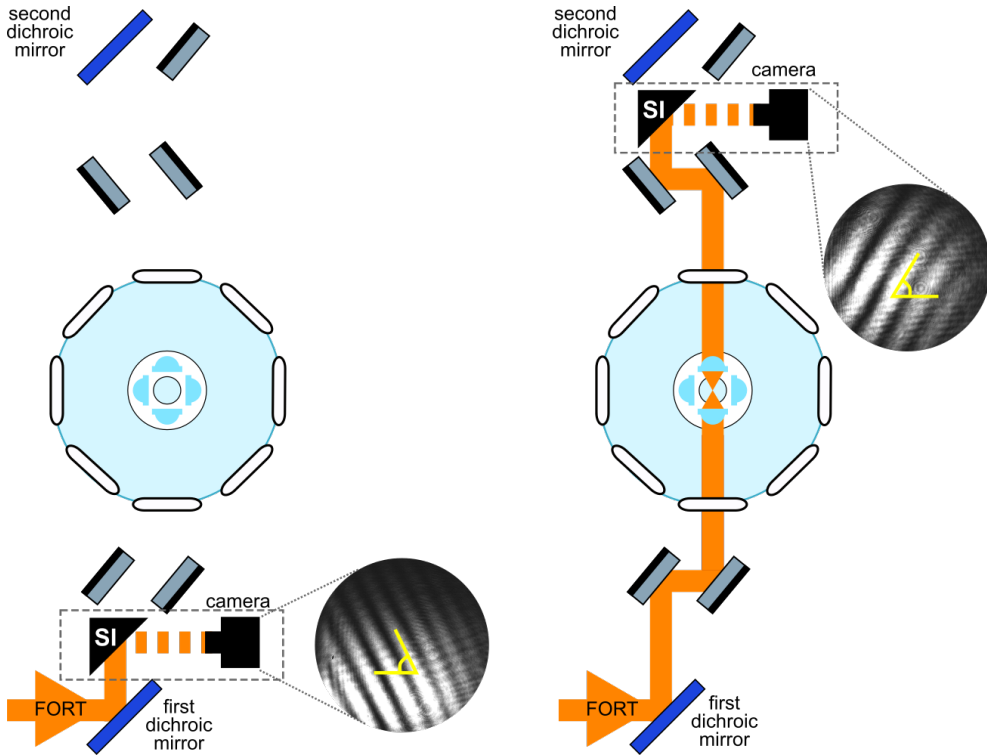
FIGURE 3.5: Setup for measurement and optimization of FORT convergence angle. Compare to central region of Figure 3.3: shearing interferometer (SI) images of the FORT beam before and after the UHV chamber in its optimal condition. Angles (in yellow, in the SI images) are $\approx 60°$ in optimal configuration. The SI is not a permanent part of the setup, but rather is placed in the indicated positions for these measurements.

3.3 The magneto-optical trap (MOT)

In this Section, I'll explain how we set up the magneto-optical trap that will produce the small cloud of cold ^{87}Rb atoms from which the FORT is loaded.

3.3.1 Laser system

As described in Section 2.2, the MOT needs the cooler and repumper beams (see Figure 3.6). In this Section, I'll describe the laser system, published in [56], mainly developed by Dr. Lorena Bianchet that generates these beams.
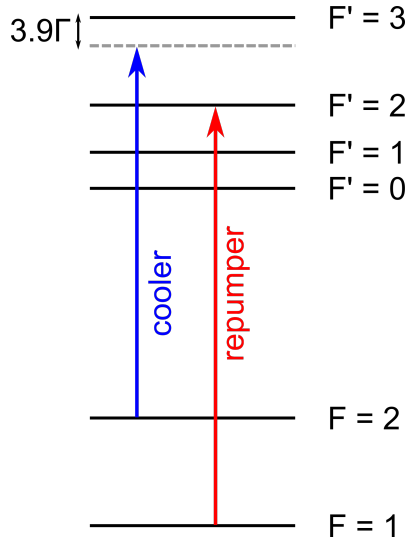
FIGURE 3.6: Frequency scheme for cooler and repumper lasers used in the MOT. F states are the hyperfine ground states $5^2 S_{1/2}$ and F' the hyperfine excited states $5^2 P_{3/2}$ of ^{87}Rb [31]. The typical value for the detuning of the cooler beam is 3.9Γ, where Γ is the natural decay rate of the D2 line $\Gamma = 2\pi \times 6.065\,\text{MHz}$.

3.3.1.1 Cooler laser

As described in Section 2.2, the MOT configuration used in our experiment is the classic geometry with six counter-propagating cooler beams and a single repumper beam. These six cooler beams are derived from a distributed Bragg reflector (DBR) laser (Photodigm PH780DBR080T8) locked using the modulation transfer spectroscopy (MTS) technique. This laser is at 780 nm and its current and temperature are controlled with a Thorlabs LDC202C current supply and Thorlabs TED200C temperature controller, respectively.

3.3.1.2 Modulation transfer spectroscopy

MTS is a nonlinear spectroscopy method that is particularly well-suited to sub-Doppler stabilization of lasers to closed transitions of gases and vapors [60, 61]. In a common implementation (and in this thesis, see Figure 3.7), MTS passes two beams, a frequency-modulated "pump" beam, and an unmodulated

"probe" beam, through a vapor cell in opposite directions with spatial overlap of the beams and a power ratio between beams (pump/probe) bigger than 1. When the two beams are properly tuned, they compete to excite a specific velocity group, and via this competition the frequency modulation of the pump induces amplitude modulation of the outgoing probe. The probe beam is detected with a photodiode and demodulated to recover an error signal that can be used as a sub-Doppler frequency reference.

The theory of MTS is well described in [61], with the specific case of the ^{87}Rb D2 line described in [60]. Here we describe in detail the implementation of the experiments described in this Thesis. See also [57, 62, 63] for related MTS work with ^{87}Rb.
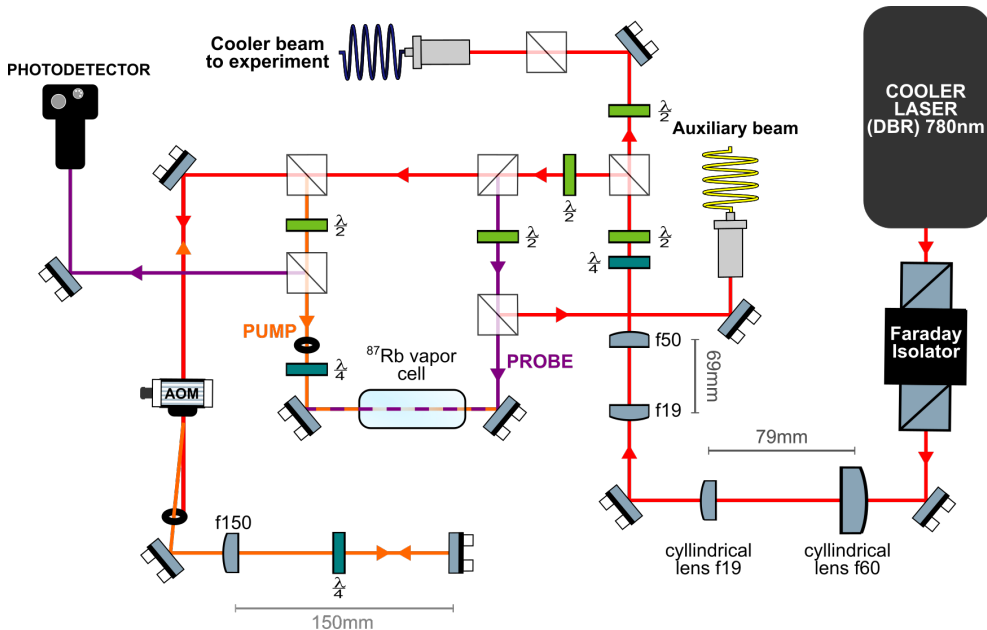
FIGURE 3.7: Setup for locking of the cooler laser. $\lambda/2$ stands for half-waveplate and $\lambda/4$ quarter-waveplate. Cubes are polarizing beamsplitters (PBS). The power after the Faraday Isolator is 60 mW, power of the probe (in purple) is 109 μW, power of the modulated pump beam (in orange) is 200 μW. The power input in the auxiliary beam is 0.9 mW and the output is 500 μW. The power input in "cooler beam to experiment" is 50 mW. The power that goes to the photodetector is 40 μW.

In the setup shown in Figure 3.7, the first two telescopes after the Faraday isolator are there to correct the shape and increase the size of the beam, respectively. The quarter-waveplate ($\lambda/4$) that follows corrects the slight circular polarization of the laser beam and then this beam is split into two: one that goes to the experiment to cool the atoms and one that goes to the locking part of this setup. The beam that goes to the locking is also split in two: a probe and a pump beam. The pump beam (in orange) needs to be modulated, as explained before, and for this, we pass it through an acousto-optical modulator (AOM, Gooch&Housego 3100-125) in a double-pass configuration where we take the -1 order. The AOM is controlled by a voltage controlled oscillator (VCO, Mini-Circuits ZX95-148-S) where we set the VCO tuning voltage to have its carrier frequency at 114.9 MHz and a frequency modulation of 1.85 MHz. The probe beam (in purple) in also split in two: one part is fiber coupled as an auxiliary beam, that will be later used to lock the repumper laser, and the other part overlaps with the modulated pump beam. Their power ratio is $P_{\mathrm{pump}}/P_{\mathrm{probe}} = 200\,\mu\mathrm{W}/109\,\mu\mathrm{W} = 1.84$. The $\lambda/4$ quarter-waveplate between the iris and before the vapor cell behaves as if a half-waveplate, and is used to optimize the error signal afterwards by controlling the power of the probe beam that goes to the photodetector. The resulting amplitude-modulated probe beam is sent to a photodetector (Thorlabs PDA 10A-EC) and the output signal is later demodulated (by mixing it with the modulation signal itself) to extract the error signal. The error signal is sent to a digital PID controller implemented in a FPGA-based data acquisition board (National Instruments PCIe-7842R) which outputs the signal that controls the current driver of the laser and sets its frequency. This locking system achieves 2 MHz full-width at half-maximum (FWHM) laser linewidth and frequency stability for days.

It is important to note that the cooler laser is locked to the closed $5^2S_{1/2}F = 2 \rightarrow 5^2P_{3/2}F' = 3$ ^{87}Rb transition with respect to the pump light, that has a red-shifted optical frequency (due to double-passage through the AOM) of -2×114.9 MHz, but the MTS only transfers the modulation at half of that

frequency, so the "cooler beam to experiment" is blue-shifted from the closed transition by $+114.9\,\mathrm{MHz}$.

For the MOT, the cooler beam[2] needs to be red-detuned from the closed transition $5^2S_{1/2}F = 2 \rightarrow 5^2P_{3/2}F' = 3$ by a few natural linewidths (Γ), and in our case, we chose it to be $3.94\Gamma = 3.94 \times 2\pi \times 6.065\,\mathrm{MHz} = 2\pi \times 23.9\,\mathrm{MHz}$. To set the cooler detuning to this proper value, we use another AOM in a double-pass configuration at $-2 \times 69\,\mathrm{MHz}$.

3.3.1.3 Repumper laser

The repumper laser (Photodigm PH780DBR080T8, same current and temperature controller models as the cooler laser) it is frequency stabilized with respect to the cooler laser using a beat-note offset lock. The optical setup for this can be seen in Figure 3.8, where again the telescope is there to correct the laser output beam shape and we later split this light in two, one part that is "Repumper beam to experiment" (input power of $46\,\mathrm{mW}$) and the "Beam to lock repumper" (input power of $2.5\,\mathrm{mW}$). For the beat-note signal, we interfere the last with the cooler "Auxiliary beam" in a 50/50 fiber beam-splitter, with respective powers of $1.5\,\mathrm{mW}$ and $500\,\mu\mathrm{W}$. One of the fiber beam-splitter outputs, which carries the information of their frequency difference, is sent to a photoreceiver (Oclaro PT10DC) that outputs a signal that is amplified and later compared to a programmable frequency by a phase-locked loop (PLL) board (Analog Devices EV-AD41020) that outputs the error signal used by the same type of digital PID controller used in the cooler lock . With this, it is possible to lock the repumper laser with a specific frequency difference from the cooler. Since the repumper has to address the $5^2S_{1/2}F = 1 \rightarrow 5^2P_{3/2}F' = 2$ transition, it needs to be $+6453\,\mathrm{MHz}$ blue detuned from the cooler. For this, the PLL lock is set at $+6320\,\mathrm{MHz}$ and the remaining needed frequency comes from the AOM in double-pass configuration that controls the on/off of the

---

[2]For the sake of brevity, since the six beams are identical in their properties, I'll refer to the them as "cooler beam", singular.

repumper at $+66.5\,\mathrm{MHz}$. This locking system achieves $2\,\mathrm{MHz}$ full-width at half-maximum (FWHM) laser linewidth and frequency stability for days.
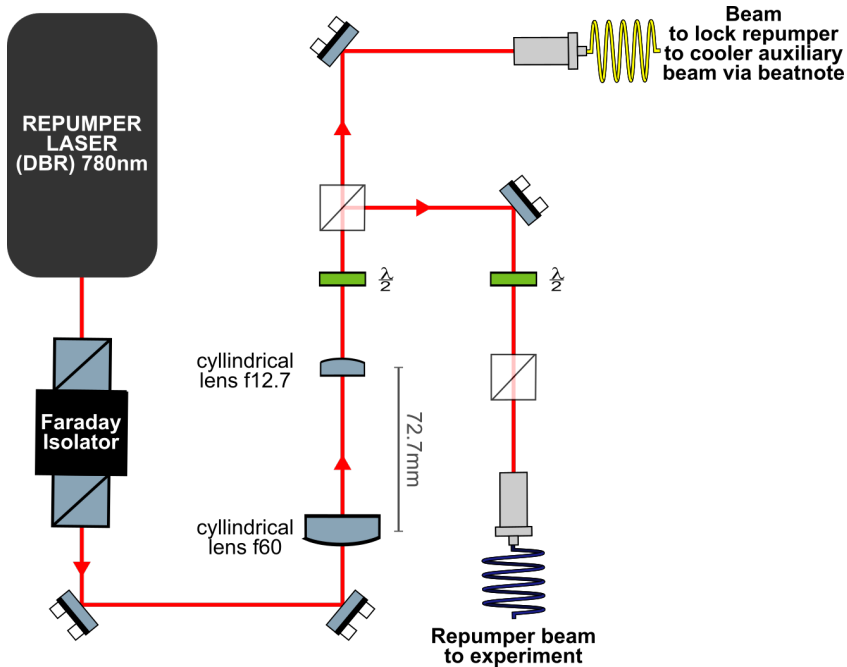

FIGURE 3.8: Setup for the locking of the repumper laser. The output of the Faraday isolator is reflected by two mirrors to a telescope and later split by a $\lambda/2$ half-waveplate and a polarizing beamsplitter (PBS) cube in two beams, one that goes to single-atom experiment and the one that is used to lock the repumper laser via the beat-note.

For more details on the laser system, see [57].

3.3.2 MOT alignment

To split this one cooler beam into six, we use half-waveplates and PBS cubes in a way that we can independently control their powers. Each of the MOT beams, namely MOT 1,2,3,4,5 and 6, is fiber coupled and sent to the main setup of the experiment depicted in Figure 3.3. In this way, just before the UHV chamber, we set their powers (Thorlabs S121C photodiode power sensor and PM100D digital monitor) to be $(20 \pm 1)\,\mu\mathrm{W}$ for the horizontal beams and $(163 \pm 8)\,\mu\mathrm{W}$ for the vertical beams. Their diameters (defined as the

$1/e^2$ intensity level) are respectively $0.7\,\mathrm{mm}$ and $2.0\,\mathrm{mm}$, measured by fitting their intensity profile in the non-fixed camera to a gaussian. This gives an cooler beam intensity I of $I/I_{\mathrm{sat}} \approx 3.2$ with $I_{\mathrm{sat}} = 16.69\,\mathrm{W/m^2}$ the saturation intensity of the D_2 closed transition for $\sigma^\pm$ polarization. The repumper beam is sent mostly through MOT 3, and its power is set to be at $20\,\mu\mathrm{W}$.
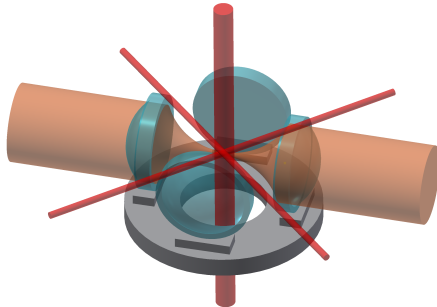

FIGURE 3.9: MOT beams illustration (in red) in the Maltese cross configuration. Horizontal beams ($\varnothing_{\mathrm{H}} = 0.7\,\mathrm{mm}$, $1/e^2$ diameter) are smaller than vertical ($\varnothing_{\mathrm{V}} = 2.0\,\mathrm{mm}$, $1/e^2$ diameter) ones due to the spatial constraint of $1.2\,\mathrm{mm}$ gap in between lenses.

Once the FORT beam is aligned to L1 and L2, we have the reference in height for the horizontal MOT beams (MOT 1 and 3, see Figure 3.3). The horizontal alignment for the MOT beams 1 and 3 is done by first passing the beam through the middle of the UHV chamber window (rough alignment) and observing with the non-fixed camera the output beam image and minimizing the scattering from the lenses (fine alignment). Once these horizontal beams are set, their counterpropagating counterparts (respectively, MOT 2 and 4) are aligned to its respective pair fibre to fibre. Two $50\,\mathrm{mm}$ diameter irises, centred with respect to the upper and lower windows of the UHV chamber, are used to align the vertical MOT beams. The vertical downward beam (MOT 6, not shown in Figure 3.3) is aligned to be centered with these irises, and its counterpart, MOT 5, is aligned to it fibre-to-fibre. This procedure aligns MOT 5 and MOT 6 along the vertical axis of the vacuum system to within mechanical tolerances in positioning the irises and assembling the vacuum

system. The four-lens assembly is similarly centered on this axis to within mechanical tolerances. In practice, it is observed that when thus aligned, these MOT beams overlap with the other MOT beams and a MOT can be formed.

The optics for the MOT beams surrounding the UHV chamber are there to ensure proper circular polarization. Once the MOT beam polarization is cleaned by a PBS cube and its power maximized by the half-waveplate before it, the $\lambda/4$ quarter-waveplate is set to have right circular (σ^+) polarization for MOT 2,4 and 6 and left circular (σ^-) for MOT 1,3 and 5 measured by a polarimeter (Thorlabs PAN5710IR1).

The magnetic fields necessary for the proper functioning of the MOT, namely, compensation and gradient coils, are depicted in Figure 3.2a. The compensation coils are responsible to cancel any surrounding bias magnetic fields, and each of the three pairs was designed to produce a constant magnetic field of 1.26 G in each coil axis x', y' and z[3] when fed by a current of 1 A. The current values used are 0.2 G, 0.02 G, and 1.1 G, respectively. The gradient coils, responsible for giving a constant gradient in the trap region, are the pair of coils that are adjacent to the z compensation coils in its innermost layer in Figure 3.2a, were designed to give 11 G/cm with 2.7 A in the y direction. For the MOT phase, this gradient is set to be 9.2 G/cm (y direction) and 4.6 G/cm (x and z directions). For more details on the design of these coils, see [57].

3.4 Photon-counter in Arduino

To count and plot in real time the number of photons detected by the APD in a chosen time bin, we use a combination of an Arduino Due microcontroller and a LabView program. This is possible because the APD outputs TTL pulses that can be detected by the Arduino Due in-built counters. The maximum voltage

---

[3]Note that the x', y' axes of the coils are rotated by $45°$ when compared to the coordinates system of Figure 3.2b.

that the Arduino Due board can take is 3.3 V, and since the TTL pulses are at 5 V, the APD output signal needs to pass through a voltage attenuator that brings this voltage down to the necessary value. The Arduino-based photon-counter was first tested with a square-wave input from a function generator at 10 kHz, and this gave counting values of 100 ± 1. This was the average amount of photon counts for a time bin of 10 ms of the previous photon counting system, a Fast ComTec P7888 Time-of-Flight photon counter.

The value of the counts for each subsequent time bin is shown in the serial monitor of the Arduino IDE, and a LabView program imports it to make a plot in real time. With the TTL pulses from the APD, the mean values of the background counts, measured for the same duration, but not simultaneously, were compared with both counters (Arduino Due and Fast ComTec), and they agreed within their statistical uncertainty (standard deviation of the mean).

The Arduino Due can also output digital signals of 5 V, and therefore the number of counts can be used as a condition for a trigger signal that starts experimental sequences upon the presence of atom in the trap. For more details on the control system, see [57].

3.5 Alignment of beams passing through the high-NA lenses and single-atom signal

With the FORT and MOT beams aligned as described above, we set the cooler detuning to 1.94Γ and the x, z magnetic gradient to 6 G/cm. The region of the MOT is imaged through L1 onto a CCD camera. If the imaging system is properly focused, something that can be accomplished using the lens before the camera, a single atom in the FORT can be seen as a bright and stationary spot against the diffuse and moving background fluorescence created by the MOT. This image of the single atom then provides a reference for alignment of the optical fibre behind L2, as follows: We send light through the L2 fiber in the direction of the atom. This light is focused by L2 to approximately the

location of the atom, before being collected by L1 and imaged on the CCD camera. Two spots, one from the atom and one from the fiber, are seen on the CCD camera, and the L2 beam can be aligned so that they overlap. The focus of the L2 beam is also adjusted, using the second lens (lens number 2 in front of L2 fiber coupler in Figure 3.3) to minimize the spot as seen at the CCD. This should produce a L2 focus at the location of the atom. The alignment of L2 is then refined by collecting single-atom fluorescence into fiber and detecting with an APD. Using the Arduino to count detections (as described in the preceding section), it is possible to align the L2 path using single-atom fluorescence in real time. Once this L2 alignment is optimized, the L1 path is aligned to the L2 path. The same procedure with the CCD camera is performed for the L4 and L3 path. With this, we can collect the fluorescence signal emitted by the atom from these four directions and plot it in real time, as shown in Figure 3.10. We note that the cooler detuning and magnetic gradient used for these operations is different from the values used in other tasks with the single atom, since in this stage of alignment it is necessary to maximize its brightness. Regarding the loading rate, it can be changed by displacing the MOT, by adjusting its compensation coils' current. The background gas loss rate is controlled by changing the current of the dispenser, which sets the flux of atoms into the UHV chamber.
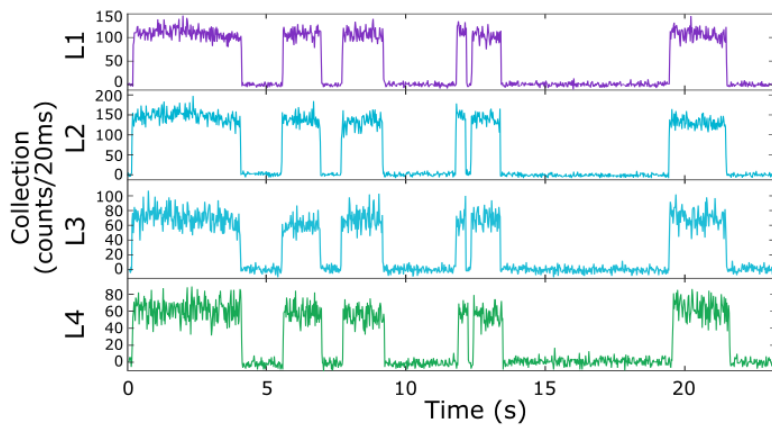
FIGURE 3.10: Fluorescence collection from the four lenses (averaged background subtracted) showing the single atom being stochastically loaded in the FORT. The atom's presence is determined when the signal jumps to a step level.

Chapter 4

Temperature Measurements

Considering all the disclaimers of the previous Section 2.4, measuring a single atom's "temperature" in the FORT is still important for its characterization. With this information, one can know what is the average kinetic energy of the atom inside the FORT, and verify if the harmonic approximation ($T_{\text{atom}} \ll T_{\text{FORT}}$) is justified and the confining potential can be approximated by an anisotropic quadratic function. It also determines how the AC Stark-shift is perceived by the atom: since it will always have a finite temperature and therefore will explore a certain region of the FORT, its resonant frequency will change according to its position. Also, to check if a certain cooling technique is effective in reducing the atom's kinetic energy in the FORT and to understand what is the cooling mechanism that is taking place, it is necessary to measure this "temperature".

To perform such measurement in our FORT in its typical configuration, we used two techniques, namely, "release and recapture" and "adiabatic lowering of the trap depth". Each of them will be explained in the next Sections and are widely used in single-atom traps [17, 64–66].

4.1 Available techniques for temperature measurement

In this section I'll discuss and show the experimental results for the available techniques to measure the single atom's temperature in a FORT: release and recapture and adiabatic lowering of the trap depth.

4.1.1 Release and recapture

The most common technique used to measure a single atom's temperature in a FORT is release and recapture, see for example [64]. Its experimental implementation is rather simple: once the atom is trapped, the FORT is turned off for a certain amount of time (Δt), after this release time, the FORT is turned back on and it is checked if the atom was recaptured. Since there is only a single atom in the FORT, there are only two possible outcomes, either it's recaptured or it's lost. Which of these outcomes occurs depends on the initial position and momentum of the atom, as well as on Δt. In particular, the position at the time the FORT is turned back on depends strongly on the initial momentum of the atom. If this later position is sufficiently far from the trap centre, the optical trapping forces will not be sufficient to recapture the atom. Because of this, the probability of recapture P_R gives information about the phase-space distribution of the atom prior to release.

By repeating release and recapture trials for a number N of atoms, the probability of recapture P_R can be estimated as

$$P_R = \frac{N_R}{N},\tag{4.1}$$

where N_R is the number of recaptured atoms. In this way, P_R is measured for several values of the release delay Δt. The resulting $P_R(\Delta t)$ data can be fit with a model for $P_R(\Delta)$ computed using the known trap potential.

It is common to follow [64] and assume a Maxwell-Boltzmann distribution for the atom's position and momentum coordinates prior to release. With this assumption, the atom's phase-space distribution, and thus the model for $P_R(\Delta t)$, has only a single parameter, the temperature T that appears in the Boltzmann distribution. In practice, it is convenient to numerically compute P_R as a function of T and Δt by a Monte Carlo (MC) simulation.

The MC simulation calculates the atom's ballistic motion after the FORT is turned off. Assuming that we are in the harmonic approximation ($T \ll T_D$), the MC simulation first selects randomly from a normal distribution a position-velocity starting condition $(x_i, y_i, z_i, v_{x,i}, v_{y,i}, v_{z,i})$, with the standard deviations given by $\Delta x = \Delta y = \sqrt{k_B T / m \omega_\perp^2}$, $\Delta z = \sqrt{k_B T / m \omega_\parallel^2}$ and $\Delta v = \sqrt{k_B T / m}$, where m is the ^{87}Rb mass. After the atom's initial condition in the FORT is set, the atom's final position-velocity vector is calculated by the ballistic motion equations during Δt,

$$
\begin{aligned}
x_f &= x_i + \frac{1}{m} p_{x,i} \Delta t \\
y_f &= x_i + \frac{1}{m} p_{y,i} \Delta t - g(\Delta t)^2 / 2 \\
z_f &= x_i + \frac{1}{m} p_{z,i} \Delta t \\
p_{f,x} &= p_i, x \\
p_{f,y} &= p_i, y - mg\Delta t \\
p_{f,z} &= p_i, z
\end{aligned}
\tag{4.2}
$$

where g is gravity's acceleration. If, after Δt, the atom has a total mechanical energy $E_{\text{tot}} \leq 0$, where

$$
E_{\text{tot}} \equiv \frac{1}{2m} |\mathbf{p}_f|^2 + U_{\text{FORT}}(\mathbf{x})
\tag{4.3}
$$

and $U_{\text{FORT}}(\mathbf{x})$ is FORT potential energy (not in the harmonic approximation), the atom is considered recaptured. Repeating this sequence for a total of $N_{\text{sim}} = N$ number of atoms at a given T, the recaptured fraction f_R is

calculated as

$$f_R = \frac{N_{R,\text{sim}}}{N_{\text{sim}}}, \tag{4.4}$$

where $N_{R,\text{sim}}$ is the number of recaptured atoms in the simulation. Repeating this sequence for different values of Δt and T, we have the simulated probability distribution $f_R(T, \Delta t)$.

4.1.2 Fitting

We would now like to fit the model f_R to the data P_R to estimate T. We note, however, that f_R is only known by MC simulation, and thus is noisy. Also, P_R is described by a binomial distribution, not a normal distribution. Nonetheless, we can justify a χ^2 fitting under the conditions we encounter in practice. We first note that, for the binomial distribution with probability of recapture P and N trials, the population variance in the fraction recaptured is

$$\text{var}(P_{\text{sample}}) = \frac{P(1-P)}{N}. \tag{4.5}$$

and thus the population standard deviation is

$$\sigma_P \equiv \sqrt{\text{var}(P_{\text{sample}})} = \sqrt{\frac{P(1-P)}{N}}. \tag{4.6}$$

Second, we note that if $\text{var}(P_{\text{sample}}) \ll P$, then P will be approximately normally distributed.

We can then identify the conditions under which we can apply the below χ^2 analysis, which is strictly speaking only appropriate for fitting normally-distributed data. Using Equation 4.5, we compute the variances $\sigma_{f_R}^2$ and $\sigma_{P_R}^2$ from the corrsponding values for P and N. Then if $\sigma_{f_R}^2 \ll \sigma_{P_R}^2$, the noise from the simulation is small and can be ignored. And if $\sigma_{f_R}^2 \ll f_R^2$ and $\sigma_{P_R}^2 \ll P_R^2$, the distributions of f_R and P_R are approximately normal. We can then approximate the maximum-likelihood estimator for T by the χ^2 estimate. That

is, we find T_{atom}, the value of T that minimizes

$$\chi^2(T) \equiv \sum_{\Delta t} \frac{[f_R(T, \Delta t) - P_R(\Delta t)]^2}{\sigma_{\text{R}}^2(\Delta t)}. \tag{4.7}$$

The uncertainty of this estimate is given by [67]

$$\delta T_{\text{atom}} = \sqrt{2 \left| \frac{\partial^2 \chi^2(T)}{\partial T^2} \right|^{-1}_{T=T_{\text{atom}}}}, \tag{4.8}$$

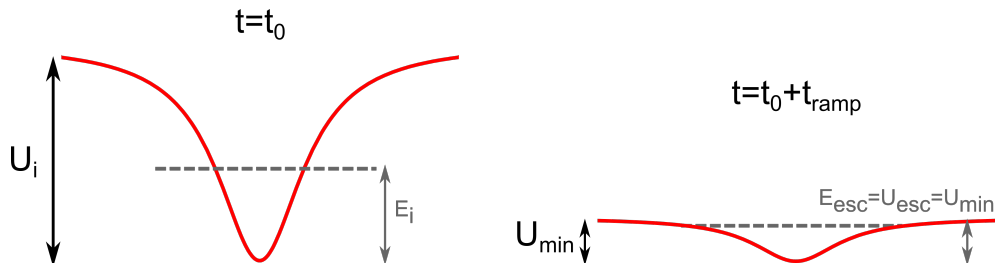assuming that $\chi^2(T)$ is a quadratic function around T_{atom}.

FIGURE 4.1: An atom that initially had an energy E_0 after being adiabatically cooled by the reduction in the potential energy during t_{ramp}, will leave the trap if its energy E is higher than the minimum potential energy U_{min}.

4.1.3 Measuring the atom's energy distribution with adiabatic cooling *or* adiabatic lowering of the trap depth

Another technique that has been used to infer the atom's temperature is measurement of the probability that the atom survives an adiabatic lowering of the trap depth. This technique was first proposed and implemented in [17] and later also used in [64] and it is illustrated in Figure 4.1.

Reducing the FORT depth[1] from U_{i} to U_{min}, under the condition that the rate of change is much slower than the trap frequency, the atom is adiabatically cooled from its initial total energy $U_i(0) + E_0$ to $U_{\text{min}}(0) + E$ and will leave

---

[1] Experimentally, this means reducing the FORT's beam power. For the sake of clarity in abbreviation, this will be referred to as the FORT's depth U_{i} and U_{min}.

the trap if this is positive. Again, since there's only one atom in the trap, the outcome of this measurement is that either the atom survived or it was lost.

Reference [17] describes a method, using as a model the adiabatic evolution of a 1D oscillator, of calculating the maximum E_0 for which the atom will remain in the trap, given values for $U_i(0)$ and $U_{min}(0)$. The model should not be expected to exactly describe the dynamics of an atom in a 3D trap, but [17] argues it is nonetheless a reasonable approximation, based on numerical 3D simulations of the atom dynamics during a slow rampdown. One attractive feature of this method is that it allows the distribution of E to be inferred directly from $P_R(U_{min})$, with no assumptions about the distribution of E. In particular, there is no assumption of a thermal state.

As in release and recapture, for each value of U_{min}, the procedure is repeated for N atoms. The probability of survival P_{surv} can then be calculated as

$$P_{surv} = \frac{N_{surv}}{N}, \tag{4.9}$$

where N_{surv} is the number of atoms that survived the lowering of the trap depth.

As the next step towards extracting the atom's temperature from the data, it is necessary to do a conversion from the minimum FORT power P_{min} to E_i, the maximum initial energy an atom can have and still remain in the FORT (E_i is the border between remaining and escaping). This can be done based on the conservation of the 1D action, due to the adiabatic process (page 154 from [68]). Defining the action as $S(E, U) = \int_0^{x_{max}} \sqrt{2m[E - U(x)]}dx$, where x_{max} is the turning point, we can map the energy $E_{esc} = U_{min}$ into the initial energy E_i. As it will be shown afterwards, solving the constant action equation $S(E_i, U_i) = S(E_{esc}, U_{esc})$ for $E_{esc} = U_{esc} = U_{min}$ in the direction of gravity (the most probable axis that the atom will escape), we have a value of E_i for each U_{min}. The atom will only survive this process if its initial energy is less than the E_i set by $E_{esc} = U_{min}$.

First, it is needed to convert the minimum FORT power $P_{\min}$ to $U_{\min}$ using the expression

$$U_{\min} = \beta' \frac{2P_{\min}}{\pi w_0^2}, \tag{4.10}$$

where

$$\beta' = \frac{\Gamma^2 \hbar}{24 I_{sat}} \left(\frac{1}{\delta_1} + \frac{2}{\delta_2} \right), \tag{4.11}$$

with $\Gamma = 2\pi \times 6.065\,\mathrm{MHz}$ the natural decay rate of the D_2 line of $^{87}\mathrm{Rb}$, $I_{sat} = 16.69\,\mathrm{W/m^2}$ the saturation intensity, $\hbar$ the normalized Planck constant, δ_1 and δ_2 the frequency detuning of the FORT beam frequency relative to the D_1 and D_2 transition, respectively [10], and w_0 its $1/e^2$ waist. The previous values give $\beta' \approx 6.17 \times 10^{-36}\,\mathrm{Jm^2W^{-1}}$.

Next, we need to numerically calculate the values of E_i using the 1D conservation of action

$$S(E_\mathrm{i}, U_\mathrm{i}) = S(E_\mathrm{esc}, U_\mathrm{esc}). \tag{4.12}$$

Since $E_\mathrm{esc} = U_\mathrm{esc} = U_{\min}$ and we know every $U_{\min}$, we must find E_i by solving the equation

$$S(E_\mathrm{i}, U_\mathrm{i}) = \int_0^{x_{\max}} \sqrt{2m\left[E_\mathrm{i} - \left(1 - \exp\left[\frac{-2x^2}{w_0^2} \right] \right) U_\mathrm{i} - mgx \right]}\, dx, {}^2 \tag{4.13}$$

where m is the mass of $^{87}\mathrm{Rb}$, g is the gravity acceleration[3] and $x_{\max}$ is found by solving the transcendental equation

$$\left(1 - \exp\left[\frac{-2x_{\max}^2}{w_0^2} \right] \right) U_\mathrm{i} + mgx_{\max} = E_\mathrm{i}. \tag{4.14}$$

---

[2]The zero energy level of the system was chosen to be the minimum FORT potential energy $U(0)$.

[3]Note that gravity only plays an important role when the trap depth is shallow ($\approx 10\,\mu\mathrm{K}$), when the potential energy is notably tilted.

Since we know the right hand side (RHS) of Equation 4.12, we must find numerically E_i that solves the equation

$$\int_0^{x_{\max}} \sqrt{2m\left[E_i - \left(1 - \exp\left[\frac{-2x^2}{w_0^2}\right]\right)U_i - mgx\right]}\, dx = S(E_{\mathrm{esc}}, U_{\mathrm{esc}}), \quad (4.15)$$

where

$$S(E_{\mathrm{esc}}, U_{\mathrm{esc}}) = S(U_{\min}, U_{\min})$$

$$= \int_0^{x_{\max}} \sqrt{2m\left[U_{\min} - \left(1 - \exp\left[\frac{-2x^2}{w_0^2}\right]\right)U_{\min} - mgx\right]}\, dx, \tag{4.16}$$

and

$$\left(1 - \exp\left[\frac{-2x_{\max}^2}{w_0^2}\right]\right)U_{\min} + mgx_{\max} = U_{\min}. \tag{4.17}$$

First, we solve Equation 4.17 for the $x_{\max}$ that will solve 4.16 (the RHS of Equation 4.12). Putting Equation 4.14 into Equation 4.13 (the relation is simpler if we take E_i as a function of $x_{\max}$ than the other way around) and numerically integrating it as a function of $x_{\max}$, we equal this expression to the solved RHS of Equation 4.12 and find the root that will give the value for $x_{\max}$ and then we calculate E_i using Equation 4.14.[4] With this calculation process, we can map every minimum FORT power $P_{\min}$ to the maximum initial energy the atom should have to survive.

To extract a temperature from the data $P_{\mathrm{surv}}(E_i)$, we need to make the assumption that the atom's energy distribution in the FORT is thermal. With this, its normalized Boltzmann energy distribution is

$$f(E) = \frac{1}{(2k_B T)^3} E^2 \exp\left[\frac{-E}{k_B T}\right], \tag{4.18}$$

---

[4]Note that there are two different $x_{\max}$, one for each side of Equation 4.12, we use the one from the RHS to solve the one on the LHS.
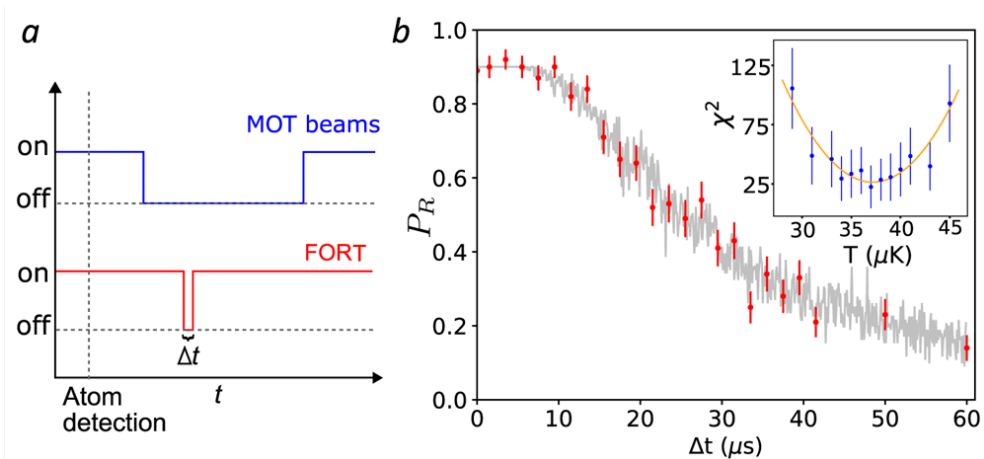
FIGURE 4.2: a) Experimental sequence for MOT beams and the FORT in the release and recapture technique (not to scale). b) Observed recapture fraction P_R as a function of the release time Δt (red circles), each point is the result of 100 trials. Error bars show $\pm$ one standard error of P_R assuming a binomial distribution. Grey points show the recapture fraction observed in a Monte Carlo (MC) simulation with $T_{\text{atom}} = 37\,\mu\text{K}$, and including a Δt-independent 11% probability of losing the atom between recapture and fluorescence detection. Inset: calculated χ^2 value between P_R and MC simulation (blue circles) for different temperatures T. Error bars show $\pm$ one standard error of χ^2 by propagation of error. A least-squares quadratic fit $\chi^2_{\text{fit}}(T)$ (orange curve) finds $T_{\text{atom}} = (37 \pm 2)\,\mu\text{K}$.

where E^2 is the three-dimensional density of states[5]. Therefore, the probability that an atom has an energy less than a certain value E is given by $P_{\text{surv}}(E) = \int_0^E f(E')dE'$. We can then fit the data to

$$P_{\text{surv}}(y) = 1 - \left[1 + y + \frac{y^2}{2}\right]\exp[-y], \qquad (4.19)$$

with $y = E_{\text{i}}/(k_B T)$ and T as the unknown variable.

4.1.4   Experimental implementation: release and recapture

The experimental sequence we used for this technique can be seen in Figure 4.2a, it mostly followed the procedure described in [64]. After the atom is detected in the trap, MOT beams and FORT are kept on for 40 ms for cooling, then the FORT is turned off for Δt and then back on, after 100 ms the MOT beams are turned on again to check by its fluorescence if the atom was recaptured. The wait time of 100 ms is introduced to ensure a temporal separation, by multiple recording time bins (of 20 ms), of the fluorescence counts before and after the release and recapture from the FORT. This avoids possible systematic errors associated with synchronization of the FORT and MOT beams to the data acquisition. We repeat this sequence $N = 100$ times for each value of Δt. The probability of recapture, P_R, is calculated as Equation 4.1. Following the binomial statistics of this probability distribution, the uncertainty σ_R in P_R is given by

$$\sigma_R = \frac{\sqrt{N_R(1 - P_R)}}{N} \tag{4.20}$$

In Figure 4.2b (red circles) we show the results for our typical trap configuration, $w_{\mathrm{FORT}} = 1.6\,\mu\mathrm{m}$ and $P_{\mathrm{FORT}} = 7.0\,\mathrm{mW}$.

To extract a temperature from the experimental results, we make use of the Monte Carlo (MC) simulation described in Section 4.1.1. For our data, the minimum of the $\chi^2_{\mathrm{fit}}(T)$ (see Figure 4.2b inset) is at $T_{\mathrm{atom}} = (37\pm2)\,\mu\mathrm{K}$, where we take the 1-$\sigma$ lower confidence bound on $\partial^2 \chi^2_{\mathrm{fit}}(T)/\partial T^2$.
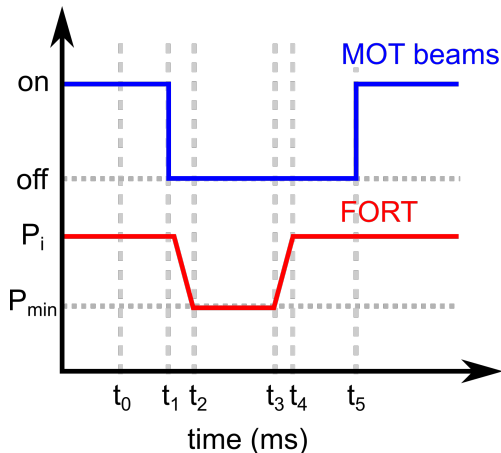
FIGURE 4.3: Experimental time sequence for MOT and FORT beams in the adiabatic lowering of the trap depth technique (not to scale).

4.1.5 Experimental implementation: adiabatic lowering of the trap depth

The experimental sequence is the following (see Figure 4.3): after the atom is detected in the trap (t_0), MOT beams and FORT are kept on for 40 ms (t_1) for cooling; the MOT beams are turned off; the FORT power is then reduced from P_i to P_{min} in 2.5 ms $(t_2 - t_1)$; this value is kept constant for 20 ms $(t_3 - t_2)$ so the atom can leave the trap if it has sufficient energy; after this, the FORT power is ramped back adiabatically to its initial value $(t_4 - t_3)$ and we wait 25 ms $(t_5 - t_4)$ to check if the atom survived this process by turning on the cooler and repumper and observe its fluorescence. The schematics for the experimental sequence and the trap depth during the experiment can be seen in Figure 4.3. Repeating this sequence $N = 100$ times for each value of P_i, the probability of survival is calculated as N_{surv}/N, where N_{surv} is the number of atoms that survived the process, the results can be seen in Figure 4.4.

By following the method described in Section 4.1.3, each P_{min} was mapped to E_i and the resulting curve, Figure 4.5, is fitted by Function 4.19 (normalized

---

[5]The E^2 comes from an analysis in [69], a wrong approach is to consider it to be $\sqrt{E}$, which was what [17] did first and then corrected with an *Erratum* [70].

to 0.8 since that was the averaged survival probability for the points around $E_i/U_i = 1$), from which we extracted $T_{atom} = (35 \pm 3)\,\mu K$ for our typical trap configuration, $w_{FORT} = 1.6\,\mu m$ and $P_{FORT} = 7.0\,mW$. We can see that this results agrees well with the release and recapture measurement method.
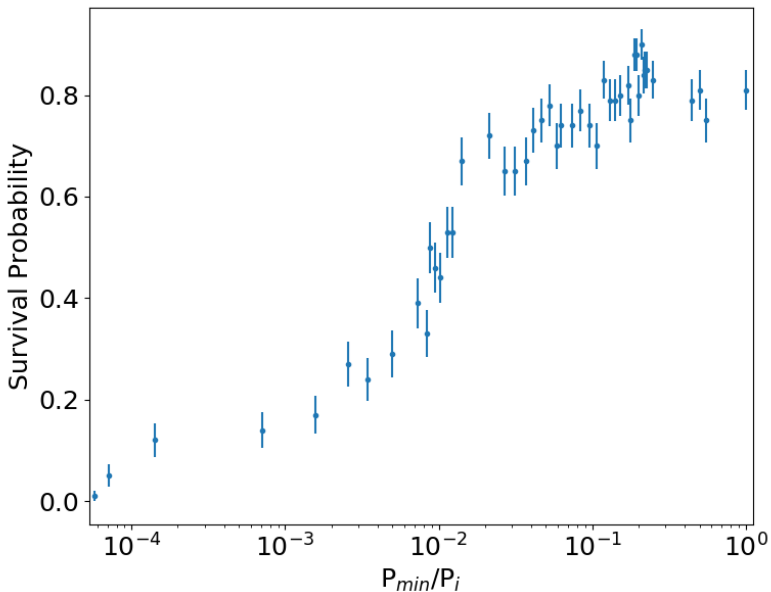

FIGURE 4.4: Observed survival fraction as a function of the ratio between minimum (P_{min}) and initial FORT power (P_i). Uncertainty is calculated following the binomial distribution, in the same way as in Equation 4.20 for the release and recapture measurement.

4.1.6 Quantum jump spectroscopy as a thermometer

We have also made use of the quantum jump spectroscopy technique, described in [25] and annexed to the end of this Thesis, to extract the atom's temperature in the FORT. As previously mentioned at the beginning of this Chapter, the ac Stark shift perceived by the atom is dependent on its instantaneous position in the FORT, and therefore, will be dependent on the atom's temperature. One could then extract the temperature of the atom in the FORT from its
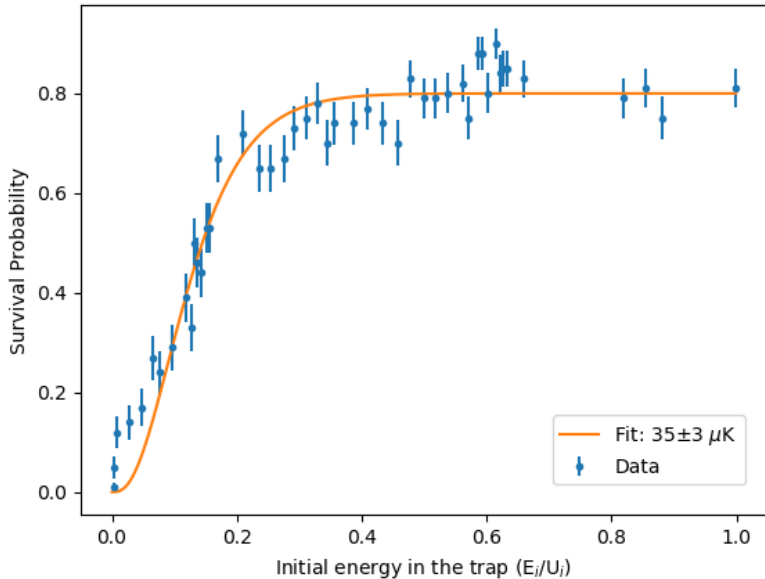
FIGURE 4.5: Same as Figure 4.4 but now the x-axis is a function of the atom's initial energy in the FORT, E_i normalized by the initial potential energy U_i. Curve fit by a weighted non-linear least squares gives $T_{\text{atom}} = (35 \pm 3)\,\mu\text{K}$, with statistical uncertainty given by the fit.

resonant spectrum profile. For this, we note that the instantaneous light shift seen by the atom is

$$\Delta_{eg} = (\delta_e - \delta_g)I_{\text{FORT}}(\mathbf{x}) \tag{4.21}$$

where δ_g, δ_e are the per-intensity light shifts of the ground and excited states, respectively, and $I_{\text{FORT}}(\mathbf{x})$ is the instantaneous intensity of the FORT. The optical potential is therefore

$$V = \alpha\Delta_{eg}, \tag{4.22}$$

where $\alpha \equiv 2\pi\hbar\delta_g/(\delta_e - \delta_g)$. Assuming the atom's center-of-mass coordinate is thermally distributed, the distribution of light shifts f_Δ is given by a Boltzmann distribution $f_\Delta \propto \exp\left[-\beta V\right]\rho(V)$, where $\beta \equiv 1/(k_B T)$ and $\rho(V)$ is the potential density of states.

To determine $\rho(V)$, we note that given $V(\mathbf{x})$, and defining $v(V')$ as the volume of $\mathbf{x}$-space for which $V(\mathbf{x}) < V'$, the potential density of states (PDoS) is $\rho(V) \equiv dv(V')/dV'|_{V'=V}$. Considering a general second-order expansion about the minimum (which we take to be at $\mathbf{r} = \mathbf{0}$), we have $V = V_{\min} + (x^2/a^2 + y^2/b^2 + z^2/c^2)$, where $V_{\min}$ is the trap minimum, x, y, z are spatial coordinates along the principal axes of the quadratic potential, and a, b, c are constants. The volume $v(V')$ is that of an ellipsoid with semi-axis lengths $(a, b, c)\sqrt{(V' - V_{\min})}$, i.e., $v(V') = (4\pi/3)[(V' - V_{\min})]^{3/2}abc$. The PDoS is then

$$\rho(V) = \begin{cases} 2\pi \left(V - V_{\min} \right)^{1/2} abc & V \geq V_{\min} \\ 0 & \text{otherwise} \end{cases}$$

$$= \begin{cases} 2\pi \left(\frac{x^2}{a^2} + \frac{y^2}{b^2} + \frac{z^2}{c^2} \right)^{1/2} abc & V \geq V_{\min} \\ 0 & \text{otherwise} \end{cases} \tag{4.23}$$

The probability density function (PDF) for the potential is thus (for $V > V_{\min}$)

$$f(V) = \frac{\rho(V)e^{-\beta V}}{\int d^3x\, e^{-\beta V(\mathbf{x})}}$$

$$= \frac{2\pi \left(V - V_{\min} \right)^{1/2} abc\, e^{-\beta V}}{\int dx\, dy\, dz\, e^{-\beta(V_{\min}+\frac{x^2}{a^2}+\frac{y^2}{b^2}+\frac{z^2}{c^2})}}$$

$$= \frac{2}{\sqrt{\pi}} \sqrt{V - V_{\min}}\beta^{3/2} e^{-\beta(V-V_{\min})} \tag{4.24}$$

which does not depend on a, b, or c, and thus is independent of the specific form of the quadratic terms in the potential. The spectrum thus depends on $V_{\min}$ and on the temperature via β, but not first or second spatial derivatives of V. With this, we have that the distribution of light shifts can be written as

$$f_\Delta(\Delta) \propto \sqrt{\alpha\Delta - V_{\min}}\, e^{-\beta(\alpha\Delta-V_{\min})}\beta^{3/2} \tag{4.25}$$

for $\alpha\Delta > V_{\min}$, and zero otherwise, see Figure 4.6. The line center reflects the average light shift, which depends strongly on the maximum intensity $I_{\mathrm{FORT}}^{(\max)} \equiv \max_{\mathbf{x}} I_{\mathrm{FORT}}(\mathbf{x})$ and weakly on the temperature T, whereas the line

width depends more strongly on T. Fitting the data of Figure 4.7 and using a bootstrapping procedure to estimate the fitting uncertainties (described in [25]), we find a temperature $T = (36.7 \pm 0.8)\,\mu\text{K}$, in good agreement with the previously independent measurements of the temperature.
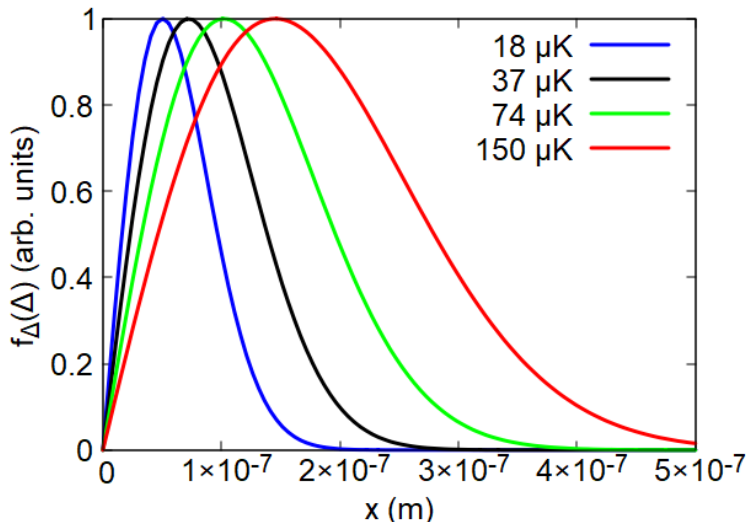

FIGURE 4.6: The light shift distribution given by Equation 4.25 for the single atom in our typical FORT configuration ($P_{\text{FORT}} = 7.1\,\text{mW}$, $w_{\text{FORT}} = 1.65\,\mu\text{m}$) for different values of T (indicated in the inset).

4.2 The release and recapture's sensitivity and precision

In light of what was discussed in Section 2.4, a natural question is if the presented techniques above are sensitive to different temperatures in different axis. In order to check it, we did simulations in Julia to calculate the atom's dynamics in the FORT for the release and recapture experiment with both equal and different temperatures for the different axis. This simulation and results will be described in the next Section.
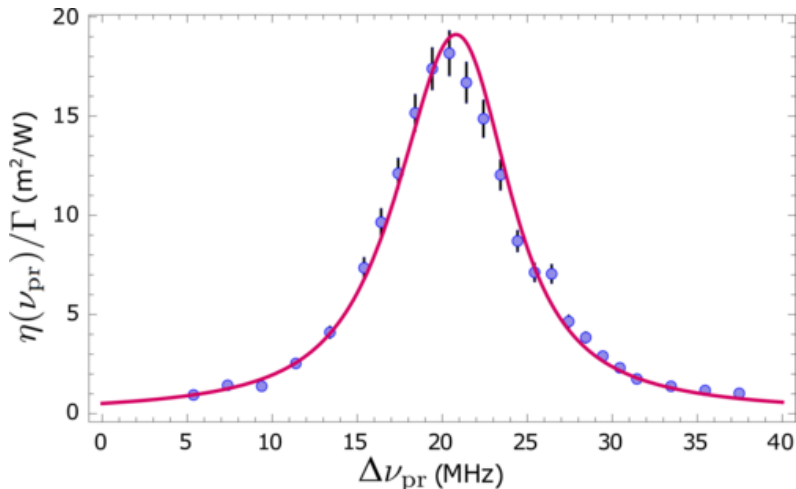
FIGURE 4.7: Quantum jump spectroscopy of the $5S_{1/2}, F = 1 \rightarrow 5P_{3/2}, F' = 2$ transition in individual FORT-trapped atoms. Horizontal axis shows detuning $\Delta\nu_{\mathrm{pr}} \equiv \nu_{\mathrm{pr}} - \nu_{1\rightarrow 2'}$ from the unshifted $\nu_{1\rightarrow 2'}$ transition frequency. The vertical axis shows excitation efficiency $\eta(\nu_{pr})/\Gamma = I_{\mathrm{sat}}^{-1}$ computed via Equation (1) in [25]. Error bars indicate plus/minus one standard error. Curves show a fit with Equation (3) of [25], with FORT intensity at trap center and atom temperature as free parameters. The fit finds $I_{\mathrm{FORT}}^{(\mathrm{max})} = (1.593 \pm 0.005) \times 10^9 \, \mathrm{W\,m^{-2}}$ at trap center and $T = (36.7 \pm 0.8) \, \mu\mathrm{K}$, with r.m.s. statistical uncertainties found by bootstrapping.

4.2.1 Simulating the atom's dynamics in the FORT

For our system, the Hamiltonian is $H = \mathbf{p}^2/2m + V(\mathbf{q}, t)$, where $\mathbf{p}$ is the atom's momentum, $\mathbf{q}$ the spatial coordinates ($q_i = x, y, z$) and m is the ^{87}Rb mass. From Hamilton's equation[6] we have that

$$\frac{\partial H}{\partial q_i} = -\dot{p}_i = \frac{\partial V}{\partial q_i}, \tag{4.26}$$

$$\frac{\partial H}{\partial p_i} = \dot{q}_i = \frac{p_i}{m}. \tag{4.27}$$

---

[6]The motion of the atom in the FORT is governed by classical mechanics because the average kinetic energy of the atom is much higher than $\hbar\omega_F$ in our typical trap.

Therefore, the atom's dynamics is determined by the equations of motion

$$\frac{dp_i}{dt} = -\frac{\partial V}{\partial q_i}, \tag{4.28}$$

$$\frac{dq_i}{dt} = \frac{p_i}{m}. \tag{4.29}$$

Inside the FORT, the potential V is given by

$$V(x, y, z) = \beta' \frac{2P_{FORT}}{\pi w^2(z)} \exp\left[-\frac{2(x^2 + y^2)}{w^2(z)}\right] + mgy, \tag{4.30}$$

with β' defined in Equation 4.11, P_{FORT} the total FORT power, $w(z) = w_{\text{FORT}}\sqrt{1 + z^2/z_{\text{R}}^2}$, $z_{\text{R}} = \pi w_{\text{FORT}}^2/\lambda$ the Rayleigh length, g the gravity acceleration constant and m the ^{87}Rb mass.

Once given the starting conditions (which will be explained afterwards), the ODEs 4.28 and 4.29 are numerically solved in Julia using the `Tsit5()` method [71], with absolute and relative tolerances of 1×10^{-4} and adaptive timestepping, from the initial time $t_i = 0$ (atom released) until the final time $t_f = \Delta t$. After this, we verify if the atom was recaptured by the FORT using the condition

$$E_{\text{tot}} < 0, \tag{4.31}$$

which is the same condition as for the release and recapture's Monte Carlo simulation. We repeat this calculation for a total of N atoms (meaning, N starting conditions), and the probability of being recaptured is again

$$P_{\text{R}} = \frac{N_{\text{R}}}{N}, \tag{4.32}$$

where N_{R} is the number of atoms that were recaptured by the FORT. This is the general calculation that will be performed in the simulation, what will

change from one technique to the other is the shape of $P_{\text{FORT}}(t)$ over time, which is qualitatively described by Figures 4.2(a) and 4.3.

4.2.2   Sensitivity of RR methods to anisotopic temperatures

Until this point we have assumed, as was assumed in prior works, a Boltzmann distribution with a single temperature describing the six degrees of freedom x, y, z, p_x, p_y, and p_z. As we argued in section 2.4, there are reasons to expect that, for a single atom in an optical dipole trap, different motional degrees of freedom will have different "temperatures." In this section we study the degree to which existing temperature-measurement strategies can detect such temperature anisotropy.

We first describe a two-temperature parametrized distribution, with one temperature describing transverse motion and one describing longitudinal motion. We then perform RR simulations to observe qualitatively the effect of these temperatures on the observable $P_R(\Delta t)$ curves. We then apply estimation theory to determine the sensitivity of the RR technique to the two temperatures, identify the optimal value of Δt for representative temperatures, and observe that even when optimized to measure it, the RR technique is far less sensitive to the longitudinal temperature.

4.2.3   Two-temperature parametrized distribution

As the simplest plausible distribution with temperature anisotropy, we consider a phase space distribution composed of two independent Boltzmann distributions, one for the transverse degrees of freedom x, y, p_x and p_y and one for the longitudinal degrees of freedom z and p_z.

These two distributions are parametrized by the "temperatures" $T_x = T_y$ and T_z, respectively[7]. We can write the probability distribution function as

$$
\begin{aligned}
f(\mathbf{q}, \mathbf{p}) &\equiv f_{xy}(x, y, p_x, p_y) f_z(z, p_z) & (4.33) \\
f_{xy}(x, y, p_x, p_y) &\equiv \frac{1}{4\pi^2 T_x^2} \exp\left[-\frac{1}{2T_x}(\tilde{x}^2 + \tilde{y}^2 + \tilde{p}_x^2 + \tilde{p}_y^2)\right] & (4.34) \\
f_z(z, p_z) &\equiv \frac{1}{2\pi T_z} \exp\left[-\frac{1}{2T_z}(\tilde{z}^2 + \tilde{p}_z^2)\right] & (4.35)
\end{aligned}
$$

where the variables with tildes over them are scaled coordinates defined such that the expectations are $E[\tilde{x}^2] = E[\tilde{p}_x^2] = E[\tilde{y}^2] = E[\tilde{p}_y^2] = T_x$ and $E[\tilde{z}^2] = E[\tilde{p}_z^2] = T_z$:

$$
\begin{aligned}
\tilde{q}_\alpha &\equiv q_\alpha \sqrt{\frac{m\omega_\alpha^2}{k_B}} & (4.36) \\
\tilde{p}_\alpha &\equiv p_\alpha \frac{1}{\sqrt{mk_B}} & (4.37)
\end{aligned}
$$

for $\alpha \in \{x, y, z\}$.

4.2.3.1 First observations regarding RR sensitivity to anisotropic temperature

We generate starting conditions according to the PDF of Section 4.2.3, and run RR simulations as described in Section 4.2.1 to obtain estimates of $P_R(\Delta t)$.

Taking $T_x = T_y = T_z = 37\,\mu\text{K}$ as the "typical" condition around which we will vary, we first study the dependence on transverse temperature $T_x = T_y$. That is, we take $T_z = 37\,\mu\text{K}$ and vary $T_x = T_y$ about $37\,\mu\text{K}$, and plot the resulting $P_R(\Delta t)$ curves. The results, shown in Figure 4.8, show a dependence of $P_R(\Delta t)$ on $T_x = T_y$ that resembles that seen in previously in Section 4.1.4.

We then study the dependence on longitudinal temperature T_z. That is, we take $T_x = T_y = 37\,\mu\text{K}$, vary T_z around $37\,\mu\text{K}$, and plot the resulting $P_R(\Delta t)$

---

[7]Due to the cylindrical symmetry of the gaussian-beam FORT potential, we assume equal temperatures for the two transverse directions.
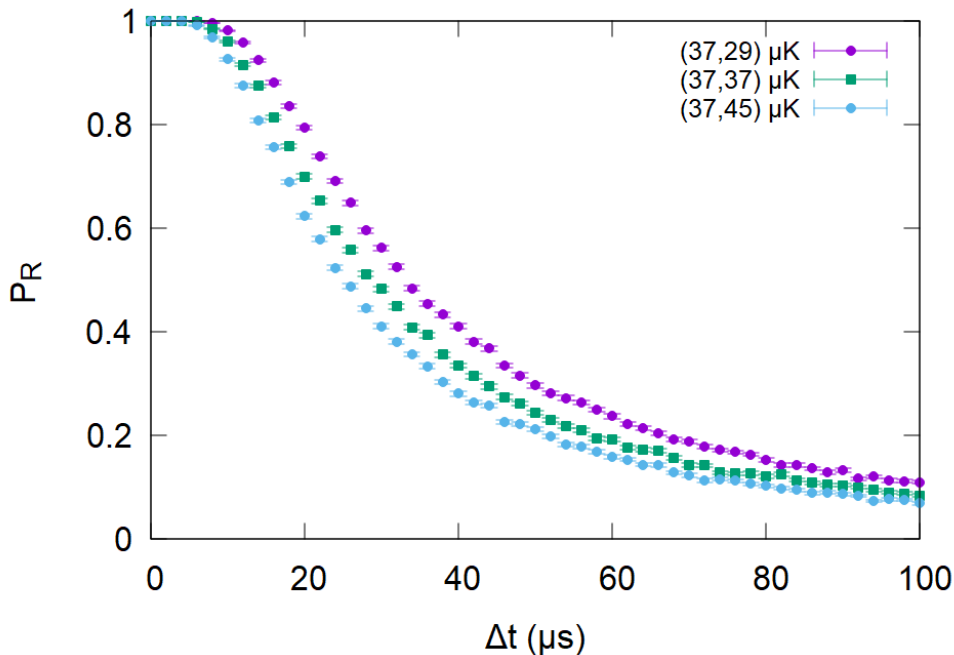
FIGURE 4.8: Simulation results for the recaptured fraction P_R as a function of the release time (Δt) for the release and recapture technique for fixed $T_z = 37\,\mu K$. The inset legend stands for $(T_z, T_{x,y})$. Each point is a set of $N = 10000$ new starting conditions. Error bars show $\pm$ one standard error of P_R assuming a binomial distribution.

curves. The results, shown in Figure 4.9, show a far weaker dependence on T_z than was seen in Figure 4.8.

As can be seen, the release and recapture experiment is at best weakly sensitive to the longitudinal temperature and is mainly measuring the transverse temperature. Meaning that if there was indeed a difference in the axis temperatures, it would be hard to see using the RR technique.

4.2.3.2 Quantitative observations about the RR sensitivity to anisotropic temperature

To understand quantitatively how sensitive the release and recapture experiment is to determine the value of different temperatures in the longitudinal
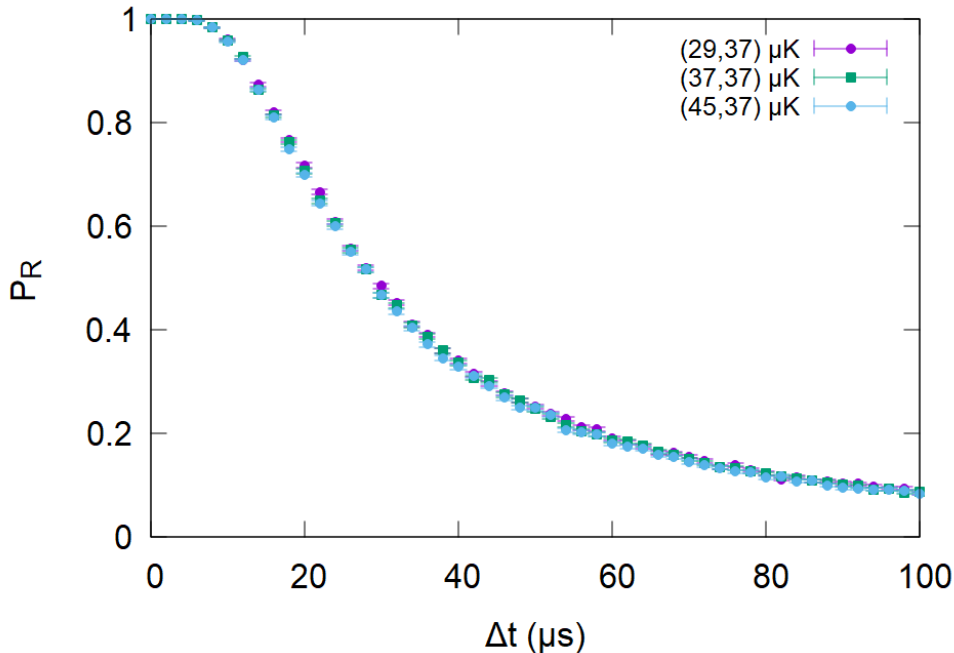
FIGURE 4.9: Simulation results for the recaptured fraction P_R as a function of the release time (Δt) for the release and recapture technique for fixed $T_{x,y} = 37\,\mu K$. The inset legend stands for $(T_z, T_{x,y})$. Each point is a set of $N = 10000$ new starting conditions. Error bars show $\pm$ one standard error of P_R assuming a binomial distribution.

and transversal axis, it is necessary to calculate the uncertainty σ_{T_z} and $\sigma_{T_{x,y}}$ in each respective measured quantity. As described already in Section 4.1.2, under appropriate conditions we can use statistical techniques suitable for normally-distributed variables, in this case the propagation of error formula:

$$\sigma_{T_z} = \left(\frac{\partial P_R}{\partial T_z}\right)^{-1}\Bigg|_{T_{x,y}} \sigma_{P_R}, \qquad (4.38)$$

and

$$\sigma_{T_{x,y}} = \left(\frac{\partial P_R}{\partial T_{x,y}}\right)^{-1}\Bigg|_{T_z} \sigma_{P_R}, \qquad (4.39)$$

where the partial derivative is taken at fixed T_z and $T_{x,y}$, and σ_{P_R} is the uncertainty in the recapture fraction P_R calculated as one standard error assuming a binomial distribution, see Equation 4.6. To calculate these partial
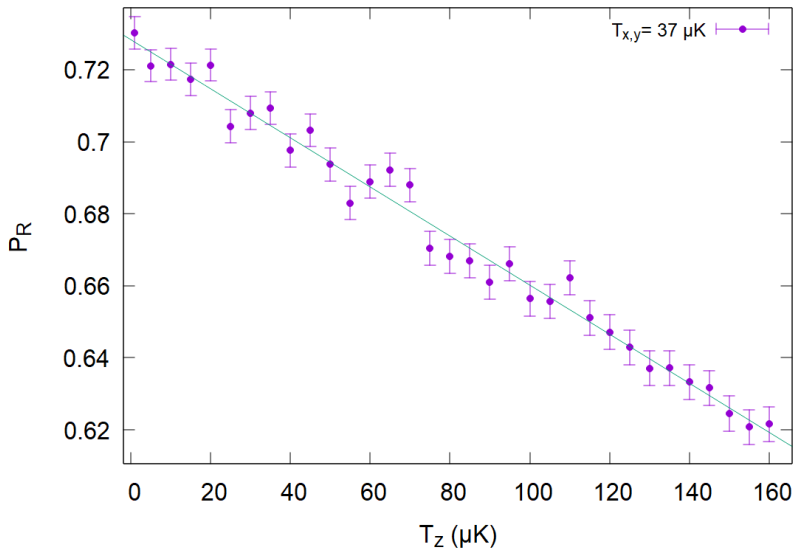
FIGURE 4.10: Simulation results for the recaptured fraction P_R as a function of the longitudinal temperature T_z and fixed $T_{x,y} = 37\,\mu$K and $\Delta t = 20\,\mu$s. Each point is a set of $N = 10000$ new starting conditions. Error bars show $\pm$ one standard error of P_R assuming a binomial distribution. In green is a linear fit to the results, that gives $\partial P_R / \partial T_z = -6.8 \times 10^{-4}\,\mu$K^{-1}.

derivatives, we need to know how P_R depends on its respective temperature. For this, we used the simulation described above to compute $P_R(T_z)$ at fixed $T_{x,y}$ and Δt, and $P_R(T_{x,y})$ at fixed T_z and Δt. We fit the results to a line to extract the slope. We note that this estimates the slope at a specific value of Δt, and the uncertainties σ_{T_z} and $\sigma_{T_{x,y}}$ are Δt-dependent. As described in Section 4.2.3.3 below, it is possible to find an optimal delay Δt that minimizes σ. There it is observed that the release time that minimizes the uncertainty in the temperatures is $\Delta t = 20\,\mu$s.

In Figures 4.10 and 4.11, $P_R(T_z)$ and $P_R(T_{x,y})$ are fitted by a linear function, which gives a constant slope for both cases. With this, we can calculate the uncertainties in Equations 4.38 and 4.39 for a "true temperature" of $T_z, T_{x,y} = 30.0\,\mu$K as

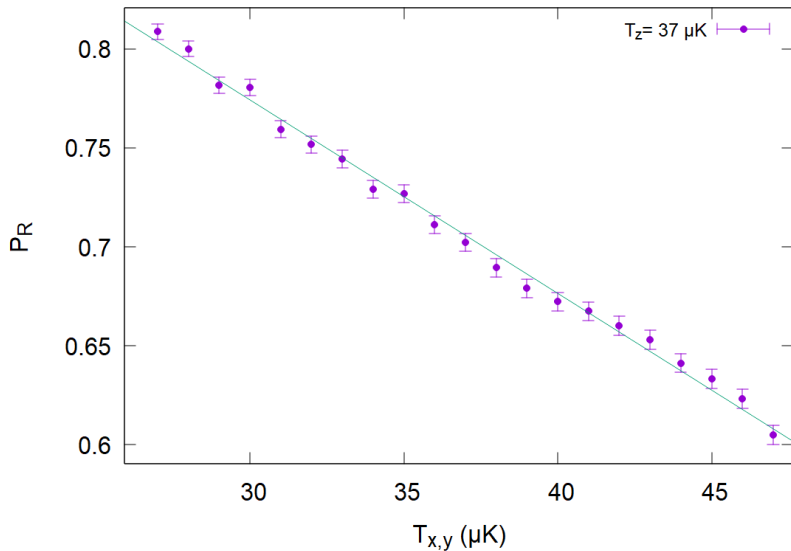$$\sigma_{T_z} = \frac{670\,\mu\text{K}}{\sqrt{N}} \tag{4.40}$$

FIGURE 4.11: Simulation results for the recaptured fraction P_R as a function of the transversal temperatures $T_{x,y}$ and fixed $T_z = 37\,\mu\mathrm{K}$ and $\Delta t = 20\,\mu\mathrm{s}$. Each point is a set of $N = 10000$ new starting conditions. Error bars show $\pm$ one standard error of P_R assuming a binomial distribution. In green is a linear fit to the results, that gives $\partial P_R/\partial T_{x,y} = -9.8 \times 10^{-3}\,\mu\mathrm{K}^{-1}$.

and

$$\sigma_{T_{x,y}} = \frac{40\,\mu\mathrm{K}}{\sqrt{N}}, \tag{4.41}$$

where $\sqrt{N}$ is the number of atoms used in the measurement.

To understand quantitatively the sensitivity of the RR in measuring the longitudinal temperature, we can compare how many atoms would be necessary to achieve the same precision of the transversal temperature using the following relation

$$\frac{640\,\mu\mathrm{K}}{\sqrt{aN}} = \frac{40\,\mu\mathrm{K}}{\sqrt{N}} \qquad \Rightarrow \qquad a \approx 281. \tag{4.42}$$

Therefore, to achieve the same precision of the transversal temperature, it takes 281 times more atoms to measure the longitudinal temperature, concluding that the release and recapture experiment is not as sensitive to the
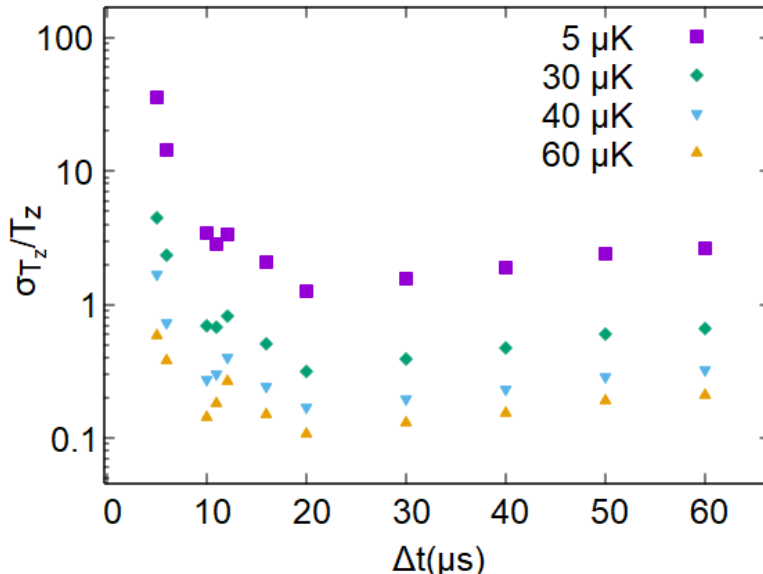
FIGURE 4.12: The relative uncertainty σ_{T_z}/T_z as a function of Δt for different values of T_z (indicated in the inset). Simulations results carried for $N = 10000$ and fixed $T_{x,y} = 37\,\mu\text{K}$.

longitudinal temperature as it is for the transversal, and could in principle detect different temperatures, but at a cost.

4.2.3.3 Optimal choice of Δt

As mentioned earlier, care must be taken in the choice of the release time to achieve the minimum uncertainty in measuring a temperature, be it longitudinal or axial. This happens because P_R and σ_{P_R} are a function of Δt, and therefore the Equations 4.38 and 4.39 will also depend on the release time. To understand this dependence on Δt, we have computed the relative uncertainty σ_{T_z}/T_z for different values of T_z. The results in Figure 4.12 show that for all T_z there is a minimum in the relative uncertainty at $\Delta t \approx 20\,\mu\text{s}$, where $P_R \approx 0.7$. It is also seen that the smaller is T_z, the bigger is the relative uncertainty.
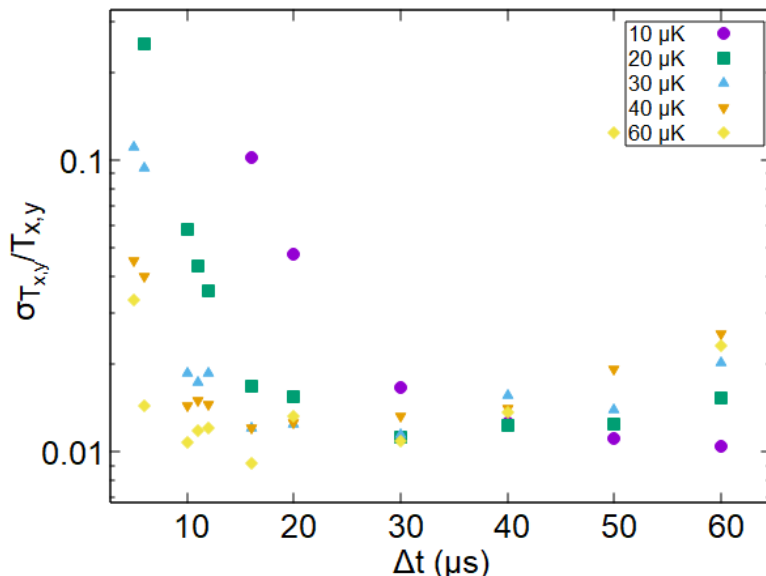
FIGURE 4.13: The relative uncertainty $\sigma_{T_{x,y}}/T_{x,y}$ as a function of Δt for different values of $T_{x,y}$ (indicated in the inset). Simulations results carried for $N = 10000$ and fixed $T_z = 37\,\mu$K.

In the case of measuring $T_{x,y}$, an optimal Δt can be found, as shown in Figure 4.13, but it depends on $T_{x,y}$: the lower $T_{x,y}$, the higher Δt needs to be in order to have the minimum uncertainty possible. Nevertheless, due to the sensitivity of RR to the axial temperatures, this does not affect the uncertainty as strongly as in the case for measuring T_z.

These conclusions were obtained using a two-temperature distribution for the atom at the moment of release, with one temperature describing the longitudinal degrees of freedom and another describing the transverse degrees of freedom. There may be reason to expect that the optical forces present, which include the optical dipole force, polarization gradient cooling, and dipole force fluctuations, may result in a still more complex distribution[8]. Nonetheless, we believe the main conclusions here, that the escape probability is only weakly dependent on the temperature of the longitudinal degrees of freedom, and thus

---

[8]Article in preparation.

that release and recapture is highly inefficient at detecting this temperature, will hold also for other initial distributions.

Chapter 5

Extinction measurement

An important characteristic of any light-matter system is the atom-light interaction strength. For single-pass systems like the one used in this thesis, one natural measure of this interaction strength is the probability p_{abs} for an atom to absorb an incident photon. This is called the "coupling efficiency" in [53]. Another measure is the probability p_{scat} for an incident photon to scatter from the atom, and thus to depart from the neighborhood of the atom in a different mode than it was when it entered. Note that p_{scat} is a lower-bound on p_{abs}, because the photon could be absorbed and then re-emitted into the original mode, a possibility that becomes more likely as the coupling becomes stronger. p_{scat}, which depends on the frequency of the photon, the atom's internal state, and the spatial matching of the input beam to the atom's dipole radiation pattern, can in principle be measured by sending an input beam of known power P_{in} and measuring the scattered power P_{scat}, so that $p_{\text{scat}} = P_{\text{scat}}/P_{\text{in}}$. In this Chapter we describe a simpler measurement of this same quantity, by measuring the extinction of the input beam, i.e., the power that is removed from the input mode by scattering from the atom. The methods used closely follow work done by the Kurtsiefer group at NUS [53, 72].

To illustrate what we measure and how this sets a lower bound to the interaction strength, consider the following (see Figure 5.1): an incoming probe
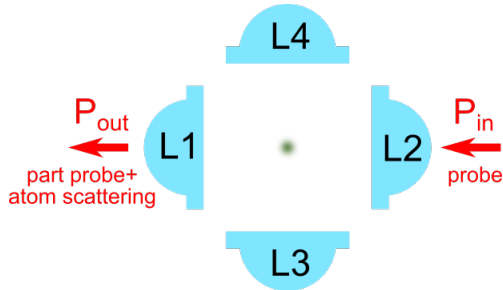
FIGURE 5.1: Scheme for the transmission measurement where we have a total input probe power P_{in} and an output power P_{out}. If the atom is in the FORT (green dot), P_{out} has the remaining part of the probe that was not scattered plus a portion of the total scattered power P_{scat}.

beam (from L2) has an input power P_{in}; after interacting with the atom, some of this light will be scattered, with a total power P_{scat}; a portion of this power is collected by the second lens (L1). The total output power P_{out} is therefore[1]

$$P_{\text{out}} = P_{\text{in}} - P_{\text{scat}} + \sigma P_{\text{scat}}, \tag{5.1}$$

where σ is the portion of the scattered light that is collected by the second lens (L1) APD[2]. Since $p_{\text{scat}} = P_{\text{scat}}/P_{\text{in}}$ and $T = P_{\text{out}}/P_{\text{in}}$ is the transmission ratio, we have that

$$p_{\text{scat}} = \frac{1-T}{1-\sigma}. \tag{5.2}$$

Defining

$$\epsilon = 1 - T \tag{5.3}$$

---

[1]Here the presented argument takes only power into account. A full description of the interference of the incoming and scattered electric fields arrives at the same conclusion, as shown in [73].

[2]This can be estimated considering the overlap between the atom's dipole emission pattern, the high-NA collection lens and the gaussian mode of the L1 optical fiber.

as the extinction, we finally have

$$p_{\text{scat}} = \frac{\epsilon}{1 - \sigma},\tag{5.4}$$

for the single-atom scattering probability. Note that the scattering probability, and therefore strength of interaction, will be always bigger or equal to the extinction ϵ. By measuring the transmission ratio T spectrum, we can extract the extinction ϵ and therefore the lower bound of the interaction strength for our system.

5.1 Extinction measurement with a linearly polarized FORT and σ^+ polarized probe

The experimental system configuration is shown in Figure 5.2. We send a σ^+ polarized probe beam through L2 and a magnetic bias field B_{bias} is applied in the same direction as the propagation of the probe. The probe beam is fully collected by L1, coupled to a single-mode fibre and sent to an APD (D1) and its photon counts are recorded in time bins of 20 ms. The light collected by L3 is also coupled to a single-mode fibre and sent to another APD (D3), and its photon counts are recorded in time bins of 20 ms. At the time this experiment was performed, the setup was using Schäfter and Kirchoof model 60FC-4-A15-02 fibre-to-free-space collimators. Unknown to the experimentalists at that time, that collimator is not well suited for producing TEM$_{00}$ gaussian beams: the beam was later observed to be "donut-shaped," with a local power minimum at the centre. Nonetheless, extinction was still observed, and we report the results here. The collimators were later replaced with Schäfter and Kirchoof model 60FC-4-M15-02.

For this measurement, the FORT has vertical polarization. This is a significant difference relative to Tey et al. [73], which used a circularly-polarized FORT. With a circularly-polarized FORT, the energy eigenstates, including

the ac Stark shifts, are F_Z eigenstates, and a circularly-polarized probe beam can pump the atom to the $|F = 2, m_F = 2\rangle$ stretched state and keep the probe-atom interaction on the closed $|F = 2, m_F = 2\rangle \to |F' = 3, m_{F'} = 3\rangle$ transition. This transition is in effect a two-level system and has maximum transition dipole moment, which maximizes the possible extinction[3]. We now consider what happens when performing an extinction measurement with a linearly polarized FORT. There are two "natural" ways to perform it: with the magnetic field along the FORT polarization direction, or with a magnetic field perpendicular to it. In the former case the field will act to stabilize the magnetic quantum number (in a basis corresponding to a quantization axis along the field and FORT polarization). In the latter case the magnetic field will tend to randomize the magnetic quantum number (in this same basis) between optical pumping events. We study the second of these scenarios.
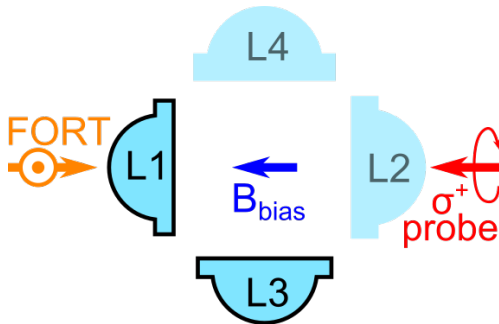

FIGURE 5.2: Experimental configuration scheme for the extinction measurement. The FORT is vertically polarized (pointing out of the plane) in the quantization axis defined by the magnetic bias field B_{bias}. The σ^+ probe is fully collected by L1 and sent to an APD. The atom's fluorescence signal from the cooler and repumper beams is also collected by L3 and sent to an APD.

The probe's frequency was set close to the $F = 2 \to F' = 3$ transition, same as the cooler, and its power was empirically set so as to not heat the atom out of the FORT, in a weak coherent state. Its polarization was σ^+ and its waist at L2 was $w_{\mathrm{probe}} = 1.2\,\mathrm{mm}$. The B_{bias} value was computed to be $B_{\mathrm{bias}} = 3.18\,\mathrm{G}$: the $9\,\mathrm{V}$ of bias applied to each of the x and y compensation

---

[3]Circularly polarized FORTs have other disadvantages, including higher atom temperature and larger ac Stark shifts.

coils pair gave a bias current of 1.78 A, and following the design of the system as mentioned in Section 3.3, this gave for each pair of coils 2.25 G, which summing their amplitudes in quadrature, gave the final bias field strength. When the magnetic bias field was not applied, we had the typical magnetic field compensation values set for the MOT.

The time sequence used (see Figure 5.3) is the following[4]: starting with all the MOT beams on, the detection of an atom in the trap triggers the sequence that starts at t_0; MOT and FORT beams are kept on for $t_1 - t_0 = 40$ ms; cooler beams are turned off for 160 ms while repumper and probe are kept on[5]; the magnetic bias field B_{bias} is applied for $t_2 - t_1 = 140$ ms and later removed; cooler beams are turned on after $t_3 - t_2 = 20$ ms for $t_4 - t_3 = 40$ ms. This sequence, from t_1 to t_4, is repeated seven more times before the cooler beams are turned off at t_5 followed by the FORT being turned off at t_6 ($t_6 - t_5 = 20$ ms) for 2 s. A representative signal from this measurement is shown in Figure 5.4: shown in green, is the photon counts from D3, and in purple is the photon counts from D1.

The photon counts of D3 are used to determine the presence of the atom in the FORT – which also triggers the experimental sequence – using the threshold value of 50 counts/20 ms, indicated by the red dashed line in Figure 5.4. The L1 photon counts from D1 are used to measure the probe transmission when the atom is in the FORT (indicated by the yellow shaded areas) and when it is not in the FORT (indicated by the red shaded area).

If we write the number of detected photons in the ith time bin (TB) as $n_{\text{D1}}^{(i)}$ or $n_{\text{D3}}^{(i)}$, for photons collected by lenses L1 and L3, respectively, then the transmission analysis is done per time bin in the following way: upon the detection of the atom in the FORT $n_{\text{D1}}^{(0)}$, the next photon count $n_{\text{D1}}^{(1)}$ is skipped; the next photon counts are averaged $\bar{n}_{\text{atom}} = \sum_{i=2}^{i=6} n_{\text{D1}}^{(i)}/5$, which is the probe transmission photon count in D1 in the presence of the atom; the next photon count is

---

[4]All the timings here are multiples of the Arduino Due time bin acquisition of 20 ms, so the analysis can be done in a well defined manner.

[5]This is because we want to avoid power fluctuations on the probe by turning on/off its AOM.
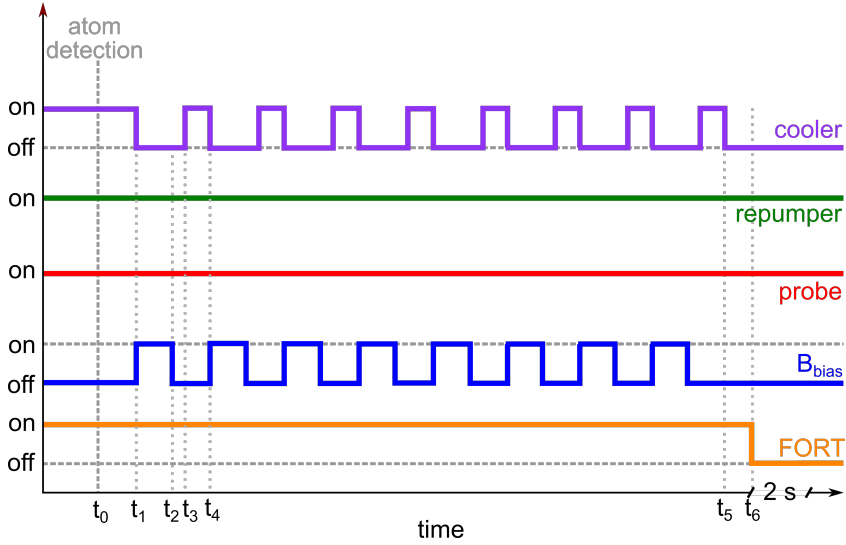
FIGURE 5.3: Time sequence for the transmission measurement. Not to scale. Details in the text.
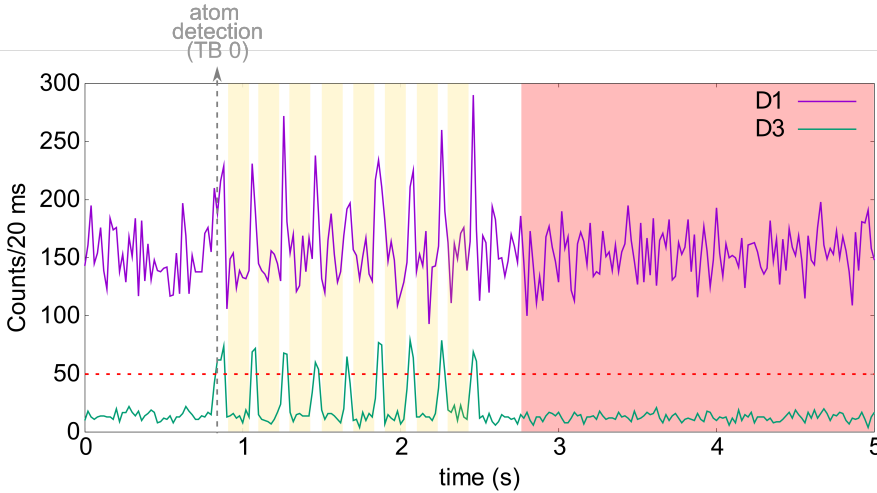

FIGURE 5.4: A representative signal of D3 (L3) and D1 (L1) photon counts for the probe transmission measurement, the atom detection is defined as the time bin (TB) 0. A background of 350 counts was subtracted from the D1 signal for visualization purposes. The transmission ratio T is calculated as the ratio between the D1 counts when the atom is in the FORT (yellow shaded area) and when it's not in the FORT (red shaded area).

skipped and this analysis is repeated for as long as the atom is in the FORT (determined by the threshold value $n_{D3} > 35$). The uncertainty in $\bar{n}_{atom}$,

σ_{atom}, is the standard deviation of all the recorded counts $n_{\mathrm{D1}}^{(i)}$ when the atom was in the FORT. The probe transmission photon counts in D1 without the atom is $\bar{n} = \sum_{i=85}^{i=174} n_{\mathrm{D1}}^{(i)}/90$, the uncertainty of $\bar{n}$, $\sigma_{\bar{n}}$, is the standard deviation of all the recorded counts $n_{\mathrm{D1}}^{(i)}$ when the atom was not in the FORT. The transmission ratio for each time sequence T_i is computed as

$$T_i = \frac{\bar{n}_{\mathrm{atom}}}{\bar{n}}, \tag{5.5}$$

with an uncertainty σ_i calculated as

$$\sigma_i = \sqrt{\left(\frac{1}{\bar{n}}\right)^2 \sigma_{\mathrm{atom}}^2 + \left(\frac{\bar{n}_{\mathrm{atom}}}{\bar{n}^2}\right)^2 \sigma_{\bar{n}}^2}, \tag{5.6}$$

by propagation of error. Repeating the time sequence of Figure 5.3 for 200 trials, we compute the transmission ratio T at a given frequency of the probe as the average of all N computed T_i

$$T = \bar{T}_i = \frac{\sum_{i=1}^{N} T_i}{N}, \tag{5.7}$$

with an uncertainty σ calculated as

$$\sigma = \frac{\sqrt{\sum_{i=1}^{N} \sigma_i^2}}{N} \tag{5.8}$$

by propagation of error.

Scanning the frequency of the probe around the resonance, we have the spectrum of the transmission ratio, which can be seen in Figure 5.5. Fitting the data to a Lorentzian function, we can extract the maximum extinction value at resonance: $\epsilon = (2.76 \pm 1.00)\%$, which is the lower bound of the atom-light interaction strength in our system in its typical configuration.

One of the aspects of the transmission spectrum showed in Figure 5.5 is that its FWHM, $\Gamma_{\mathrm{ext}} = 2\pi \times (14.7 \pm 1.7)\,\mathrm{MHz}$, is much larger than the natural linewidth of the $^{87}\mathrm{Rb}$ D_2 transition, $\Gamma_0 = 2\pi \times 6.065\,\mathrm{MHz}$. What can explain
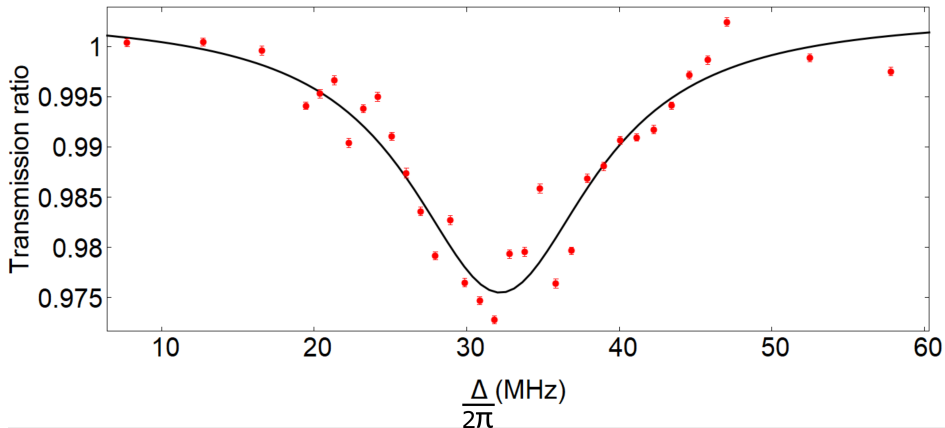
FIGURE 5.5: Transmission ratio (T, calculated as in Eqn. 5.7) as a function of the detuning (Δ) from the D_2 unshifted closed transition of ^{87}Rb. Error bars calculated as in Eqn. 5.8. A Lorentzian fit to the data gives a resonance at $\Delta_{\text{ext}} = (32.2 \pm 0.3)\,\text{MHz}$, an extinction of $\epsilon = 2.76 \pm 1.00\%$ and a FWHM of $\Gamma_{\text{ext}} = 2\pi \times (14.7 \pm 1.7)\,\text{MHz}$, where the statistical uncertainties come from the 1-σ fit confidence level. A background of 0.03% appears due to the FORT light reflection into the L1 optical path.

such discrepancy is the probe laser linewidth of $2\,\text{MHz}$, the movement of the atom inside the FORT due to extra heating from the probe (that leads to a stronger position-dependent ac-Stark shift[6]), and the fact that we were not able to do optical pumping[7]. The minimum of of the transmission curve is at $\Delta_{\text{ext}} \equiv (\omega - \omega_0) = 2\pi \times (32.2 \pm 0.3)\,\text{MHz}$, which is the detuning of the probe frequency, ω, from the D_2 unshifted closed transition of ^{87}Rb, ω_0.

As mentioned before, given the FORT and probe polarization, and the magnetic bias direction, we were not able to do optical pumping. This is because the quantization axis (QA) that diagonalizes the hamiltonian H_S of the ac-Stark effect (in the m_F basis) is in the direction of the FORT's polarization, x, while the QA that diagonalizes the hamiltonian H_Z for the Zeeman shift is

---

[6]Taking into account the losses in the path between the atom and L1's APD, the actual probe input was ≈ 2500 photons per $20\,\text{ms}$, and taking the found interaction strength of 2.76% , could lead to an increase in temperature of $25\,\mu\text{K}$ per $20\,\text{ms}$ (given that the recoil temperature is $\approx 362\,\text{nK}$ [31]).

[7]Power broadening in this measurement is neglected, since $I_{\text{in}} \approx 0.0004 I_{\text{sat}}$

in the direction of the magnetic bias field, z (which is also the FORT's propagation direction). This means that it's not possible to find a m_F basis that diagonalizes at the same time the hamiltonian $H = H_S + H_Z$ for the ground and excited states. Therefore, it is convenient to use different QAs to address the ground and excited states, since the first is more affected by the Zeeman shift while the second by the ac-Stark shift. Consider for example that the atom is in the ground state $|F = 2, m_F = 2\rangle$ (QA along z), if the ac-Stark shift splitting of the excited states is larger than the decay rate and the excitation bandwidth (this is the case in the experiment), a σ^+ photon from the probe (QA along z) can, by energy conservation, only excite $|F' = 3, m_{F'}\rangle$, $|F' = 3, -m_{F'}\rangle$, or a superposition of these (QA along x), for some value of $m_{F'}$. This is not the same as exciting $|F' = 3, m_{F'} = 3\rangle$ (QA along z), because that state is a superposition of all the m'_F levels (QA along x). In this sense, the excitation process does not conserve the atomic angular momentum of the atom + probe light, but rather transfers some angular momentum to the FORT. This results in non-cycling transitions, with contributions from all the possible m_F and $m_{F'}$ (QA along z and x, respectively), which reduces the atom-light interaction efficiency, reflecting in the extinction value, broadening the transmission spectrum and changing the resonance shift. Therefore, the found value for ϵ is taken as the lower bound of the interaction strength in our system.

Chapter 6

Parametric excitation of a single atom

Parametric excitation (PE) is a phenomenon that happens when a parameter, typically the resonance frequency, of a harmonic oscillator is modulated at or at near twice the oscillator's mean resonant frequency. As an example, one can consider a pendulum of length L in a gravitational acceleration g and thus angular frequency, for small excursions, of $\omega_0 = \sqrt{g/L}$. If the length or the gravity is modulated at angular frequency $2\omega_0$, e.g., if $L(t) = L_0\left[1 + \delta L \cos(2\omega_0 t + \phi)\right]/2$, the oscillator will experience parametric amplification (PA). PA is a phase-sensitive amplification effect, in which oscillation with a certain phase relationship to the parametric modulation ($\phi \approx \pi/2$, see Figure 6.1) will grow exponentially, while oscillation with a phase 90 degrees different from this will decay exponentially.

For a thermal ensemble of atoms, in which the oscillation phases are random, PA implies a net increase of energy (hence the name parametric *excitation* in this context), because while some atoms lose amplitude and thus energy, this loss is more than overcome by other atoms' gain of energy, due to the exponential nature of the amplification. This effect can be observed in trapped ensembles, where the modulation of the trap frequency at twice its resonant
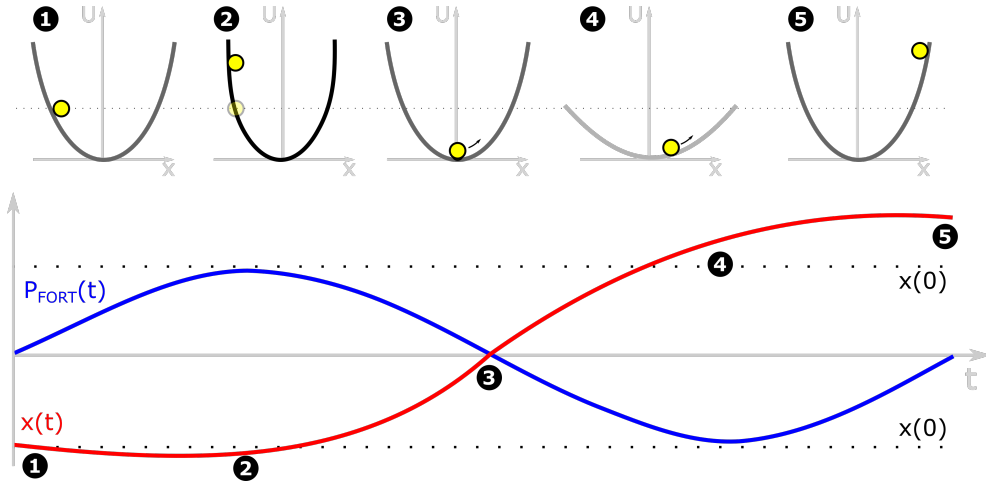
FIGURE 6.1: Illustration of parametric amplification (PA) in a harmonic trap. Top curves represent the potential energy U as a function of position x for different t. Bottom curves represent the one-dimensional amplitude of motion of the atom inside the trap as a function of time ($x(t) = x_{\max} \cos(\omega_\perp t)$, in red) and the applied modulation to the FORT power as a function of time ($P_{\mathrm{FORT}}(t) = P_{\mathrm{FORT}} + \cos(\omega_\perp t + \phi)$, in blue), amplitudes not to scale. Correspondence between top and bottom curves indicated by the numbers. For PA to happen, there needs to be be a phase difference of $\phi \approx \pi/2$ between $x(t)$ and $P_{\mathrm{FORT}}(t)$. On resonance, the period of modulation $t_{\mathrm{mod}} = 1/\nu_{\mathrm{mod}}$ is half of the atom's oscillation period $t_{\mathrm{osc}} = 2\pi/\omega_\perp$.

value manages to heat a fraction of the atoms out of the trap. This effect has been used to measure FORT resonant frequencies [74, 75], by measuring the fluorescence of an ensemble – and the number of atoms – as a function of the modulation frequency. Specifically, a minimum in the curve of atom number versus modulation frequency is expected to occur at the second harmonic of a trap frequency.

An extension of this methodology has been applied to single atoms in a FORT, with the same goal [76–78]. In this extension, the survival probability was measured after a certain modulation time. As in the ensemble case, the minima of the curve of survival probability versus modulation frequency were taken to indicate the second harmonics of the trap frequencies.

PE is an interesting technique for FORT characterization because it can selectively excite longitudinal and axial motion. For the single atom trap, this could be used to test the sensitivity of temperature measurement techniques regarding different temperatures along different axes. As an example, one could use PE to excite the longitudinal axis and perform a RR measurement and compare the results against the RR performed on atoms that had been prepared in the same way, but without PE. If no significant difference is observed, one would have experimental evidence that RR is insensitive to the longitudinal temperature. In this Chapter, we will describe the simulations and experiments we have done using PE to address another effect, the phase-space distribution distortion, and how this could be used as a cooling or heating technique.

6.1 PE simulation implementation

To understand the effects of parametric excitation on the phase-space distribution of the atoms, we have performed simulations as described in Section 4.2.1, with the difference that the FORT power is sine-modulated with an amplitude of 20% ($P_{\text{FORT}} = 10.1\,\text{mW}$) at $\nu_{\text{mod}} = 117\,\text{kHz}$, for $n = 7$ or $n = 7.5$ cycles, followed by an un-modulated "wait time" δt, as qualitatively described in the yellow shaded area of Figure 6.2.

Repeating the above simulation sequence for $N = 10000$ starting conditions (shown in Figure 6.3 for $T_{x,y,z} = 37\,\mu\text{K}$) we can construct the phase-space distributions at the end of the "wait time" δt, as a function of the number of modulation cycles applied to the FORT power. The results are shown in Figure 6.4 and Figure 6.5. From these graphs, it is seen that as n increases, the shape of the distribution becomes more distorted, towards an S shape, which is due to the anharmonicity of the potential, since atoms that have a larger amplitude of oscillation will experience the "softer" steepness of the trap shape, and therefore will have a slower oscillation period and consequently will lag behind the atoms that have smaller oscillation amplitude. If the atoms are
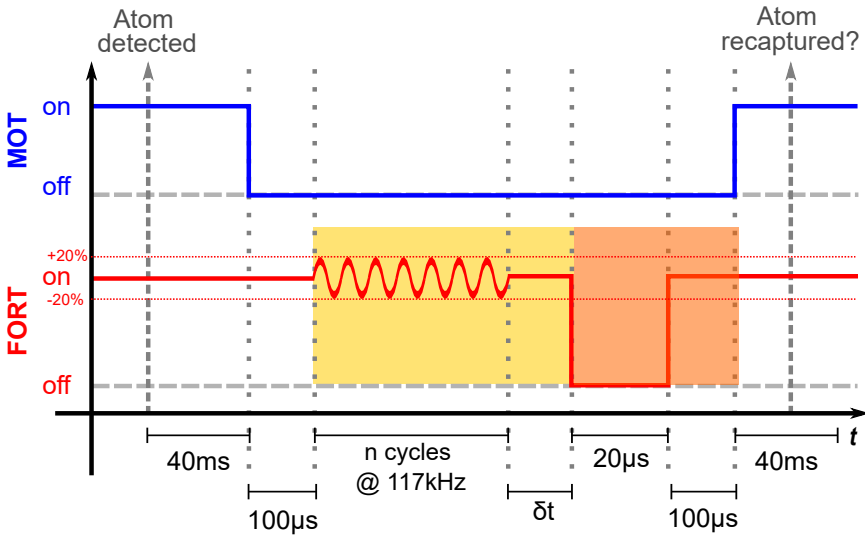
73

FIGURE 6.2: Experimental sequence for MOT beams and the FORT in the parametric excitation measurement (not to scale). The number n of cycles applied can be an integer ($n = 7$) or a half-integer ($n = 7.5$). Yellow and orange shaded areas describe the FORT power implemented in the simulations, for details, see text.

driven for many cycles, $n > 10$, the shape evolves to something more evenly distributed and sparse.

We'll focus now on the cases $n = 7$ and $n = 7.5$, shown in Figure 6.6. Besides the S shape, the points within the solid ellipse curve (which I'll refer to as "central points"), are either squeezed in momentum or position, i.e., one of their variances (Δp_f^2, Δx_f^2), is lowered, when compared to the starting conditions variances (Δp_i^2, Δx_i^2). In the case of $n = 7$ and $\delta t = 1\,\mu\mathrm{s}$, the central points are squeezed in momentum, $\Delta p_\mathrm{f}^2 < \Delta p_\mathrm{i}^2$, which can be understood as an effect of cooling, where there is a reduction of the mean kinetic energy due to the PA, in a similar way as in "delta kick cooling" [79]. The opposite effect, heating, is observed for $\delta t = 4.92\,\mu\mathrm{s}$, where the central points are squeezed in position, $\Delta x_\mathrm{f}^2 < \Delta x_\mathrm{i}^2$, and $\Delta p_\mathrm{f}^2 > \Delta p_\mathrm{i}^2$. Conversely, if the FORT is modulated for $n = 7.5$ cycles, it can be seen that the previous observations
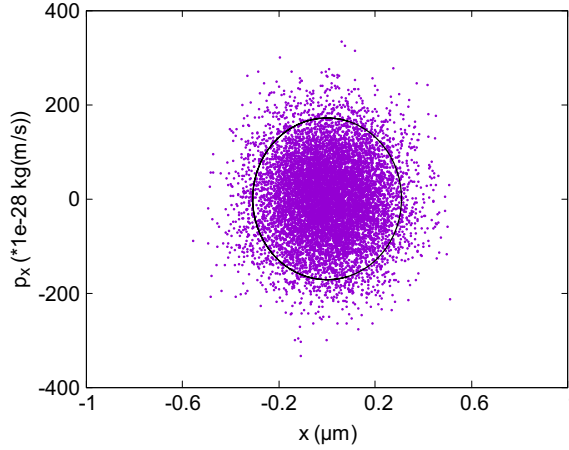
FIGURE 6.3: Phase-space distribution (x coordinate) for $N = 10000$ starting conditions for $T_{x,y,z} = 37\,\mu$K. Solid ellipse indicates the region defined by two times the standard deviations ($\Delta p = \sqrt{mk_BT}$, $\Delta x = \sqrt{k_BT/(m\omega_\perp^2)}$) of a thermal distribution.

are interchanged, and furthermore, the distribution is more spread along the momentum axis, which indicates a stronger propensity to the heating effect.

One must notice that the new phase-space distributions after δt no longer represent a thermal one, and therefore assigning a temperature to it assuming such distribution is not correct. However, to quantify the heating or cooling effect of PE plus the "wait time" δt, we therefore define a "kinetic temperature" $T_{\rm k}$ as

$$T_{\rm k} = \frac{\Delta p_{\rm f}^2}{mk_B}, \tag{6.1}$$

where $\Delta p_{\rm f}^2$ is the standard deviation of the momentum distribution m is the ^{87}Rb mass and k_B is the Boltzmann constant. This $T_{\rm k}$ is a "temperature" related to the $x-$coordinate assuming the equipartition theorem where each degree of freedom contributes equally to the total mean kinetic energy given by $(3/2)k_BT_{\rm k}$. On Table 6.1 it is shown the values of $T_{\rm k}$ for various n, and to see graphically how they are related, the same data is plotted in Figure 6.7. Note that for the integer cycles, $n \leqslant 7$, there is a reduction in the kinetic temperature, whereas for half-integer cycles it always increases.
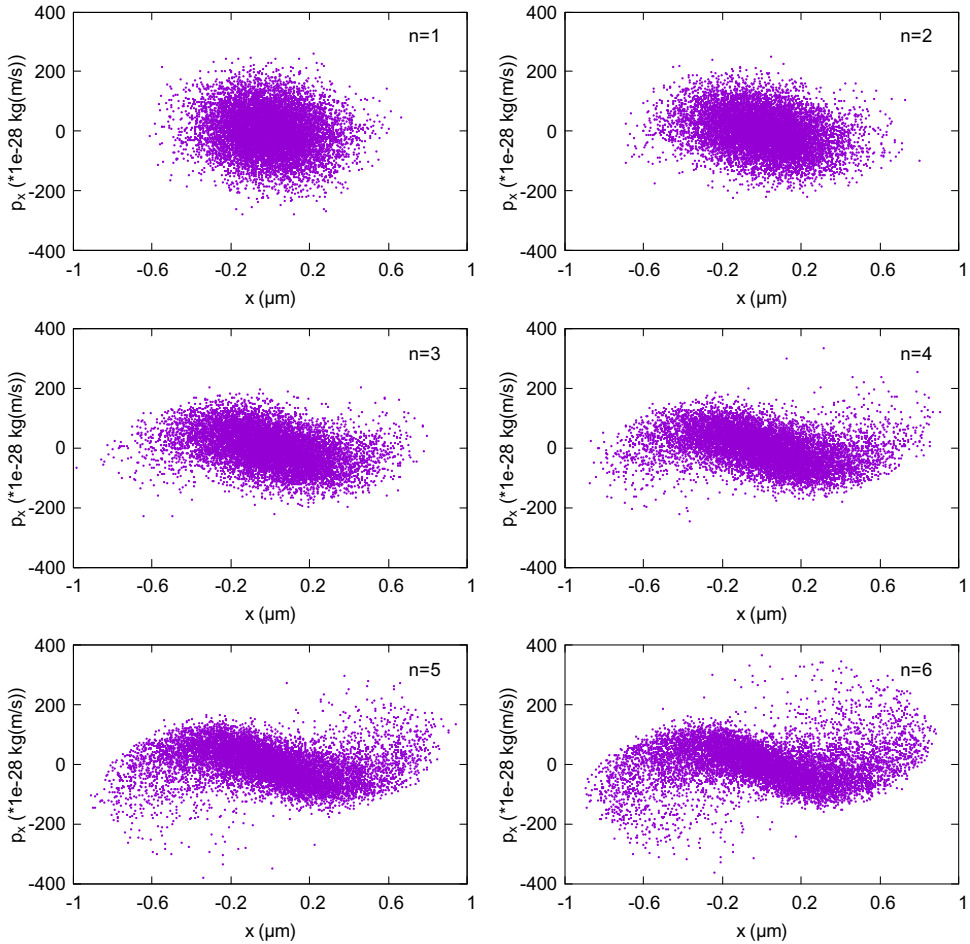
75

FIGURE 6.4: Phase-space distribution (x coordinate) for a modulation of n cycles indicated in the inset and "wait time" $\delta t = 1\,\mu$s.

Since experimentally we cannot have access to the phase-space distribution, it is necessary to translate the squeezing into a laboratory observable. For this, we have added release and recapture into the simulations. The FORT depth as a function of time used then is the one described in the yellow and orange shaded areas of Figure 6.2, with a release time of $20\,\mu$s. Repeating this new sequence for $N = 10000$ starting conditions and $T_{x,y,z} = 37\,\mu$K, we have computed the recapture fraction P_{R} as a function of δt, shown in Figure 6.8 for both number of cycles $n = 7$ and $n = 7.5$. As discussed before, there is a different behavior between them, which is translated into a phase
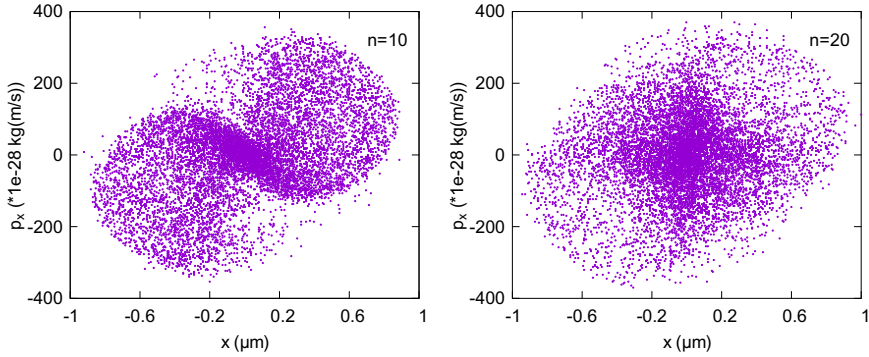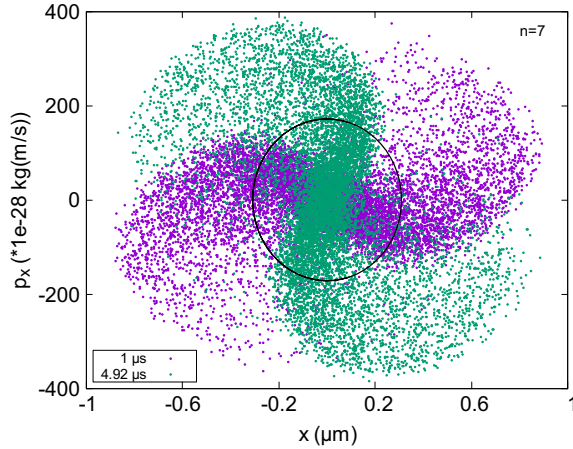
FIGURE 6.5: Phase-space distribution (x coordinate) for a modulation of n cycles indicated in the inset and "wait time" $\delta t = 1\,\mu$s.

n	$\Delta p_\mathrm{f}(kg \times m/s)$	$T_\mathrm{k}\ (\mu K)$	n	$\Delta p_\mathrm{f}(kg \times m/s)$	$T_\mathrm{k}\ (\mu K)$
0	86.62	37.6	0	86.62	37.6
1	75.64	28.7	1.5	97.71	47.9
2	68.02	23.2	2.5	112.13	63.1
3	62.88	19.8	3.5	129.26	83.8
4	60.75	18.5	4.5	147.43	109.1
5	63.29	20.1	5.5	164.26	135.4
6	71.55	25.7	6.5	177.87	158.8
7	84.38	35.7	7.5	186.55	174.7
10	128.40	82.7	10.5	181.45	165.2
20	120.70	73.1	20.5	157.03	123.8

TABLE 6.1: Standard deviation of the momentum distribution, Δp_f, and kinetic temperature, T_k, for $\delta = 1\,\mu$s, $\nu_\mathrm{mod} = 117\,$kHz and n modulation cycles.

change. For $n = 7$, P_R starts high, reaching even $P_\mathrm{R}(n = 7, \delta t = 1\,\mu\mathrm{s}) = 0.793 \pm 0.004$, a higher value than $P_\mathrm{R}(n = 0, \delta t = 1\,\mu\mathrm{s}) = 0.750 \pm 0.004$, where no modulation was applied. For $n = 7.5$, the opposite behavior is observed, with the recapture probability being as low as $P_\mathrm{R}(n = 7.5, \delta t = 1\,\mu\mathrm{s}) = 0.219 \pm 0.004$. In light of what was discussed previously and in Chapter 4, $P_\mathrm{R}(n = 7, \delta t = 1\,\mu\mathrm{s}) > P_\mathrm{R}(n = 0, \delta t = 1\,\mu\mathrm{s})$ indicates that there is a squeezing in the kinetic temperature, since more atoms were recaptured than in the case of no modulation, which agrees with the T_k predicted in Table 6.1.

(a) Phase-space distribution (x coordinate) for a modulation of $n = 7$ cycles and wait time δt indicated in the inset. Solid ellipse indicates the region defined by two times the standard deviations ($\Delta p = \sqrt{mk_B T}, \Delta x = \sqrt{k_B T/(m\omega_\perp^2)}$) of a thermal distribution before parametric excitation is applied.
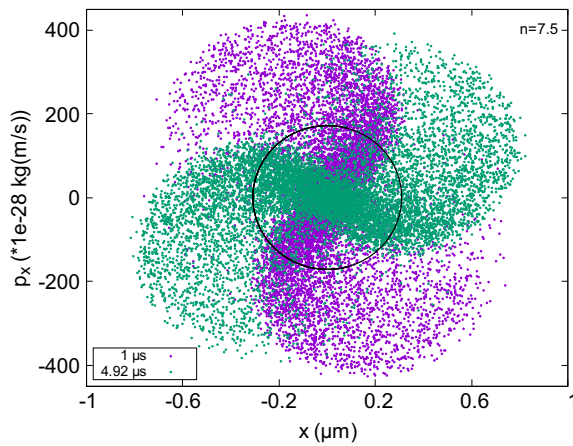
(b) Phase-space distribution (x coordinate) for a modulation of $n = 7.5$ cycles and wait time δt indicated in the inset. Solid ellipse indicates the region defined by two times the standard deviations ($\Delta p = \sqrt{mk_B T}, \Delta x = \sqrt{k_B T/(m\omega_\perp^2)}$) of a thermal distribution before parametric excitation is applied.

FIGURE 6.6

An interesting remark is to check which apparent temperature[1] would the

---

[1]Note again that this is just a remark, since we cannot assign a "true temperature" to a phase-space distribution that is not a thermal one.
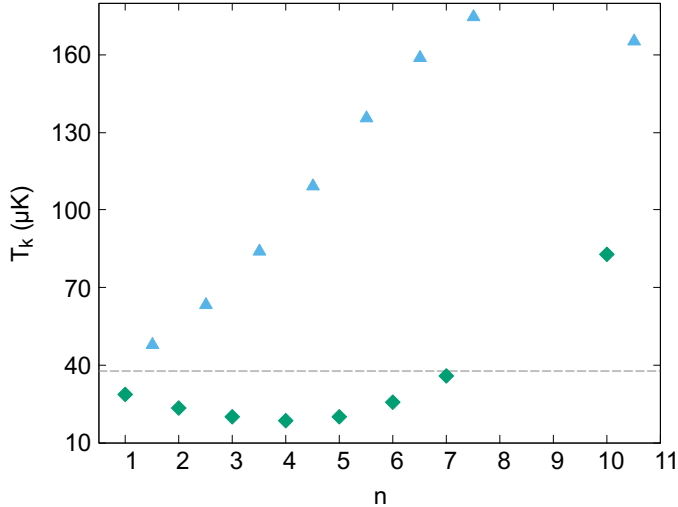
FIGURE 6.7: "Kinetic temperature" T_k as a function of the n number of modulation cycles applied to the FORT power. Dashed gray line is $T_k = 37.6\,\mu$K. Points below and above this line indicate the reduction and increase effects, respectively, on the kinetic temperature.

n	$\delta t(\mu s)$	P_R	σ_{P_R}	T (μK)
0	1.00	0.750	0.004	35.8 ± 0.3
7	1.00	0.793	0.004	31.5 ± 0.3
7.5	1.00	0.219	0.004	174 ± 2
0	4.92	0.750	0.004	35.8 ± 0.3
7	4.92	0.265	0.004	143 ± 2
7.5	4.92	0.666	0.005	44.0 ± 0.4

TABLE 6.2: Recapture fraction P_R for the simulated PE of the FORT at $\nu_{\mathrm{mod}} = 117\,$kHz $(N = 10000)$ for n cycles, "wait time" δt and release time $\Delta t = 20\,\mu$s. The last column shows their respective apparent temperature T extracted from the fitting method of Section 4.1.2.

release and recapture (RR) fitting tool, described in Section 4.1.2, give if one applied it to the previous results. For this, we make use again of the Monte Carlo simulation together with the χ^2 analysis, which gives the apparent temperatures T presented in Table 6.2 for different values of n and δt. A comparison between T_k and T for $n = 7$ shows that the RR would predict a
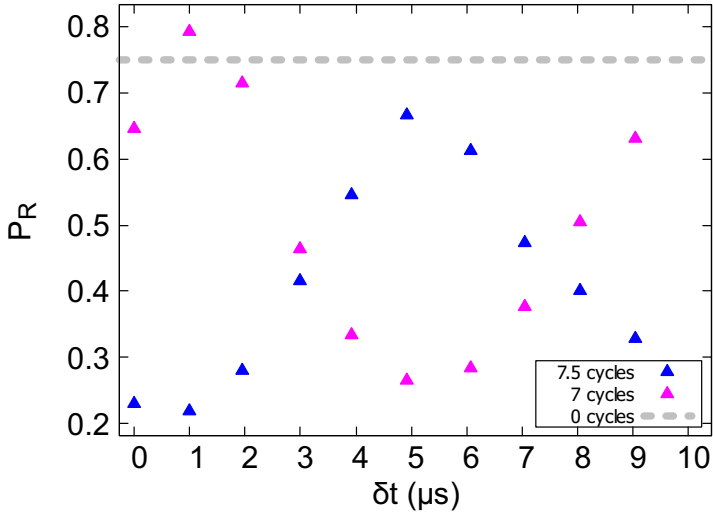
FIGURE 6.8: Recapture fraction P_R for the simulated parametric excitation of the FORT as a function of the "wait time" δt and release time $\Delta t = 20\,\mu\mathrm{s}$. The inset indicates the number of cycles applied in the modulation. Error bars are smaller than the size of the points. $P_{\mathrm{R,n=0}} = 0.750 \pm 0.004$ for no applied modulation.

lower temperature, while for $n = 7.5$ RR gives the same value. Additionally, we have seen in simulation results presented in Table 6.3 that the apparent temperature T depends on the release time Δt, which once again shows that a thermal distribution does not accurately describes the atom's position and momentum distribution after PA.

6.2 PE experimental implementation

To experimentally verify the simulated results of Figure 6.8, we have performed the sequence shown in Figure 6.2: after an atom detection, the MOT and FORT beams are kept on for $40\,\mathrm{ms}$; MOT beams are turned off and the FORT beam is kept on for another $100\,\mu\mathrm{s}$; the FORT power is sinusoidally modulated at $\nu_\mathrm{mod} = 117\,\mathrm{kHz}$ with an amplitude of $\approx 20\%$ for $n = 7$ or $n = 7.5$ cycles (we accomplish this by modulating the amplitude of the radio frequency signal

n	$\delta t(\mu s)$	$\Delta t(\mu s)$	P_{R}	$\sigma_{P_{\mathrm{R}}}$	T (μK)
0	1.96	20	0.750	0.004	35.8 ± 0.3
7	1.96	20	0.859	0.003	25.4 ± 0.2
7.5	1.96	20	0.242	0.004	159 ± 2
0	1.96	30	0.521	0.005	35.9 ± 0.4
7	1.96	30	0.765	0.004	18.8 ± 0.2
7.5	1.96	30	0.137	0.003	153 ± 3

TABLE 6.3: Recapture fraction P_{R} for the simulated PE of the FORT at resonance 124.77 kHz ($N = 10000$) for n cycles, "wait time" δt and release time Δt. The last column shows their respective apparent temperature T extracted from the fitting method of Section 4.1.2.

that feeds the AOM and consequently the power of the first diffraction order); the modulation is turned off and the FORT is kept on for a variable "wait time" δt; the FORT is then turned off for $20\,\mu$s and back on; after $100\,\mu$s the MOT beams are turned back on and we check if the atom was recaptured. The FORT power used for this experiment was $P_{\mathrm{FORT}} = 10.1\,$mW, but everything else was kept under the same typical conditions as described in chapter 3.

Repeating the above sequence $N = 250$ times for a fixed δt, we can estimate the recapture probability P_{R} in the same way as Equation 4.1. We have measured P_{R} as a function of the "wait time" δt, for integer and half-integer cycles, and the results are shown in Figure 6.9. The phase change between them was indeed observed, as predicted by the simulation results, however, the amplitude for P_R was not reproduced. Moreover, the experimental results are phase-shifted when compared to the simulated ones. Nonetheless, the experimental results agree qualitatively with the simulation predictions and show that P_{R} is dependent on δt and n.

One reason that could explain why experiment and simulation do not agree is that actually the FORT waist, $w_{\mathrm{FORT}} = (1.65 \pm 0.02)\,\mu$m, is not the one we extracted from the quantum jump spectroscopy described in [25]. This could explain the mismatch of amplitude and phase from the simulated results. To check this hypothesis, we have run the same simulations but with a new waist

value of $w_{\mathrm{FORT}} = 1.61\,\mu$m. This value is outside the uncertainty reported in [25], but it is not an unreasonable value. It can be seen in Figure 6.10 that with this new waist, there is a better agreement between simulation and experimental results in phase and amplitude. The simulation results also showed a high sensitivity of the phase to the FORT waist, which is an indication that this can be a good technique to measure its value. Another way to check the value of the waist is to use another technique to measure its value, such as the double release and recapture, as in [10].
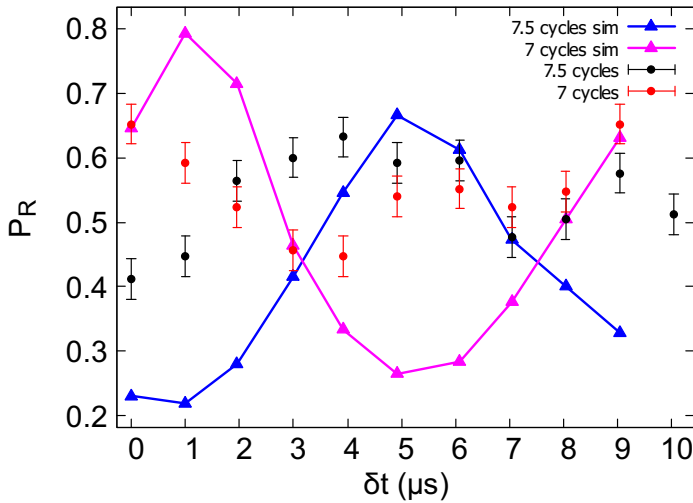
FIGURE 6.9: Experimental (black and red) and simulated (blue and magenta) recapture fraction P_{R} for PE as a function of the "wait time" δt. Error bars show $\pm$ one standard error of P_{R} assuming a binomial distribution. $P_{\mathrm{R}} = 0.79 \pm 0.03$ (experimental) for no applied modulation.
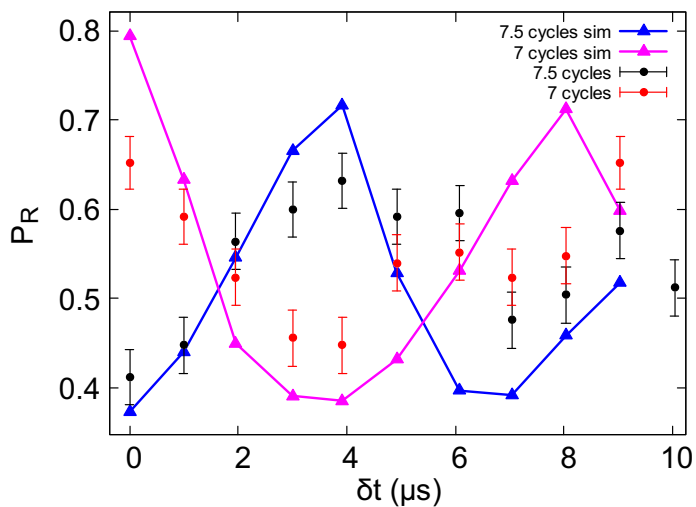
FIGURE 6.10: Experimental (black and red, same as in Figure 6.9) and simulated (blue and magenta) recapture fraction P_R for PE as a function of the "wait time" δt. For the simulated results, a new waist $w_{FORT} = 1.61\,\mu m$ was used. Error bars show $\pm$ one standard error of P_R assuming a binomial distribution.

Chapter 7

Conclusions

In this Thesis, it was studied, with simulations and experiments, the dynamics of a single-atom in a FORT. Given that for our typical trap configuration the atomic dynamics in the FORT can be treated classically, we have simulated such dynamics with the programming language Julia. The experimental setup we have in our laboratory for the single-atom trap follows a Maltese cross configuration, where four lenses are aligned along the cardinal axes and the optical dipole trap is a single-beam FORT. In particular, we've discussed the concept of the single-atom temperature and presented reasons to consider that its distribution in this system could differ from a single-temperature Boltzmann one due to the asymmetry in the confining potential and the unbalanced forces from cooler beams and the FORT itself, which can lead to an anisotropic temperature distribution.

Two of the available techniques to measure the atom's temperature in a FORT were implemented in our experimental setup: the release and recapture (RR) and the adiabatic lowering of the trap depth. It was shown that both results agreed. We have also discussed with simulations results the sensitivity of the release and recapture technique to a possible anisotropic temperature distribution, and it was shown that RR is largely insensitive to the temperature associated with the longitudinal axis of the FORT. We also found that to measure

this longitudinal temperature with the same sensitivity as for the transverse ones, we need 281 more trials, a relevant result to be considered if measurement time is limited. Furthermore, if one wants to do such a measurement, we saw in the simulation results that there is an optimum release time, of 20 μs, to achieve minimum uncertainty in this temperature. Accurately measuring the single-atom temperature in the FORT is crucial for determining the distribution of the ac Stark shift experienced by the atom, the approximations that can be done regarding the trapping potential and furthermore, is pertinent to the atom-light interaction strength since it was shown that it is limited by the residual motion of the atom [80] and that the center-of-mass motion can determine and limit the achievable single-photon excitation probability [81].

We have also measured the interaction strength between a tightly focused probe beam and the atom. Having the FORT linearly polarized, and with a bias magnetic field along the trap axis, and thus orthogonal to the FORT polarization, we observed an extinction of $\epsilon = 2.76 \pm 1.00\%$ for our typical trap configuration. We take this as a lower bound of the light-atom coupling efficiency, and note that due to a collimator that was not diffraction limited, and the orthogonal directions of FORT polarization and bias magnetic field, this number can probably be improved in the future.

Lastly, the parametric excitation (PE) of the single-atom in a FORT was discussed, where we have presented simulations results that show that the modulation of the FORT power can be used to manipulate the phase-space of the atom and be used to decrease or increase its kinetic energy, effectively heating or cooling it, respectively. We have also implemented the parametric excitation experimentally, where we observed the change in phase – predicted by the simulation results – that an integer or half-integer number of modulation cycles causes in the recapture probability of the atom after a certain release time, which proved the manipulation of the phase-space distribution by parametric excitation.

Parametric excitation that is applied for a short time (order of μs) also shows

the potential to be a more precise technique for the trap frequency measurement, since the atom, for a few modulations cycles, still explores the harmonic approximated shape of the FORT. Therefore, by combining the parametric excitation with the release and recapture, one can have a recapture probability as a function of modulation frequency which could show a dip at the FORT frequency.

Furthermore, to have experimental evidence that release and recapture, for temperature measurement, is insensitive to the longitudinal temperature, we could use PE to excite the longitudinal motion and observe if the release and recapture results are affected by it. With the Maltese cross geometry, we have access to the visualization of the atomic cloud from two perspectives, parallel and orthogonal to the FORT axis, which allows the implementation of time-of-flight techniques [82] to measure the longitudinal temperature and therefore have a direct observation of the possible anisotropic temperature distribution of the atom in the FORT.

Future opportunities offered by the system presented in this Thesis include the study of the unconventional quantum correlations of light emitted by a single atom [22]; the atom as a sensitive and precise photo-detector; and the atomic Hong-Ou-Mandel effect, where the atom acts as a beam splitter for two incoming photons.

Appendix A

"Quantum jump spectroscopy of a single neutral atom for precise subwavelength intensity measurements"

In this Appendix, we reproduce the paper "Quantum jump spectroscopy of a single neutral atom for precise subwavelength intensity measurements" by Lorena C. Bianchet, Natalia Alves, Laura Zarraoa, Tomas Lamich, Vindhiya Prakash and Morgan W. Mitchell, published in Physical Review Research, volume 4, pages L042026 1-6 in November 2022 [25], and cited in Section 4.1.6.

Quantum jump spectroscopy of a single neutral atom for precise subwavelength intensity measurements

Lorena C. Bianchet [1,*] Natalia Alves [1] Laura Zarraoa [1] Tomas Lamich [1]
Vindhiya Prakash [1] and Morgan W. Mitchell [1,2]

[1]*ICFO - Institut de Ciencies Fotoniques, The Barcelona Institute of Science and Technology, 08860 Castelldefels, Barcelona, Spain*
[2]*ICREA - Institució Catalana de Recerca i Estudis Avançats, 08010 Barcelona, Spain*

We present precise, subwavelength optical intensity measurements using a single trapped ^{87}Rb atom as a sensor. The intensity is measured by the scalar ac Stark shift it produces on the $F = 1 \rightarrow F' = 2$ hyperfine transition of the D_2 line, chosen for its $F' = F + 1$ structure and very small tensor polarizability. To boost signal and reduce measurement-induced perturbations, we use a quantum jump spectroscopy technique in which a single absorbed photon on a transition of interest induces the scattering of hundreds of photons on a bright closed transition. The method greatly reduces systematic effects associated with the atomic state, optical polarization, probe power, and atom heating, and gives the atomic temperature as a second spectroscopic observable. We demonstrate the method by measuring the intensity at the focus of an optical tweezer.

Individual trapped ions and neutral atoms can be positioned with submicrometer precision, and have been used to detect a variety of environmental perturbations, including static [1] and oscillating [2] magnetic fields, static electric fields [3], and microwaves [4]. Measurement of optical intensity, which in many scenarios varies on micrometer scales, is a natural application for such sensors [5,6]. Subwavelength (also known as super-resolving) measurements of both resonant [5] and off-resonant light [6,7] have been demonstrated. Single atoms and ions are also ideal for metrology referenced to unchanging atomic properties, e.g., polarizabilities that can be calculated with high precision [8,9]. Single trapped atoms thus offer a route to precision radiometry with high spatial resolution.

Off-resonance light, which for any given atom constitutes the vast majority of the optical spectrum, can be detected by the ac Stark shifts it produces on observable spectral lines. For example, single neutral ^{87}Rb atoms in far-off-resonance traps (FORTs) have been used to quantify ac Stark shifts by monitoring fluorescence on the $F = 2 \rightarrow F' = 3$ cooling transition of the D_2 line [6,7,10]. While this strong, closed transition is convenient, it is not naturally suited for precision intensity measurement because it, like other strong closed transitions, has large vector and tensor polarizabilities. This implies (1) that a scalar ac Stark shift to be detected will necessarily be accompanied by a broadening or splitting of the resonance fluorescence line [7] and (2) that the resonance fluorescence intensity will depend on the polarization of the excitation light, the atomic Zeeman state, and, via the FORT intensity distribution, also the atomic position. These atomic attributes are easily perturbed by the resonance fluorescence process itself, which modifies the atom's internal state through optical pumping, and its position through recoil effects [7]. All these factors complicate the interpretation of the acquired spectra.

Here we introduce a single-atom probing method that greatly reduces these systematic effects, through the use of an open transition and "quantum jump" readout [11–15] to amplify the resulting signal at very low probe power levels. We apply the technique to measure the intensity distribution seen by an atom in an optical tweezer, i.e., a strongly focused FORT [16], of the sort used to study quantum light-matter interactions [17–22], nonclassical atom interference effects [10,23–25], Rydberg-atom-based quantum information processing [26], quantum simulation [27,28] and computation [6,29,30], manipulation of cold molecules for quantum information and searches for physics beyond the standard model [31–34], and also optomechanics and quantum optomechanics with levitated nanoparticles [35–37]. In this application, the method reveals both the trap-center intensity with high precision and also the atom temperature, both of which are subject to considerable systematic uncertainty when measured by other methods [38].

The method, illustrated in Fig. 1, is a spectroscopic probe of the open $1 \rightarrow 2'$ transition of the D_2 line, i.e., $5S_{1/2}F = 1 \rightarrow 5P_{3/2}F' = 2$ (for brevity, we indicate the ground and excited hyperfine states of this transition with unprimed and primed symbols) that, rather than detecting fluorescence on this transition, detects the induced state change using quantum jump physics, previously studied with ions [11,12], molecules [13], cavity-bound photons [14], and quantum dots [15]. A weak probe beam, tuned near the $1 \rightarrow 2'$ transition, can promote the atom to the $F = 2$ "bright" ground state by a resonant Raman transition. From there, counterpropagating cooler beams drive resonance fluorescence on the closed $2 \rightarrow 3'$ transition, Rayleigh scattering hundreds of photons on average
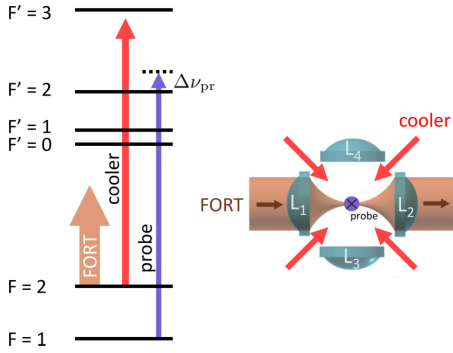
*lorena.bianchet@alumni.icfo.eu

FIG. 1. Principle of the quantum jump spectroscopy method. Left: Relevant levels of ^{87}Rb $5S_{1/2} \rightarrow 5P_{3/2}$, D_2 transition. Resonance fluorescence is produced on the closed $2 \rightarrow 3'$ hyperfine transition from the $F = 2$ "bright" state, whereas the $F = 1$ "dark" state does not fluoresce. A probe beam with a frequency detuning of $\Delta\nu_{\rm pr}$ from the $1 \rightarrow 2'$ transition can cause Raman transitions to the bright state, resulting in a "quantum jump": a burst of resonance fluorescence that greatly amplifies the effect of the single-photon scattering event that caused the jump. The resonance fluorescence also cools the atom's center-of-mass motion, returning it to a probe-independent state before the next probe absorption. Right: Geometry of the experiment, viewed from above. Four in-vacuum high-numerical-aperture lenses (L_1 to L_4) collect resonance fluorescence, and also serve to produce the strongly focused FORT. The repumper propagates together with the four horizontal cooler beams. A circularly polarized probe beam propagates in the vertical direction (perpendicular to the plane of the figure), together with the fifth and sixth cooler beams (not shown).

before the atom spontaneously falls back to the $F = 1$ "dark" ground state. The probe and cooler beams are on continuously, so the atom stochastically emits bursts of resonance fluorescence at an average rate set by the rate of $1 \rightarrow 2'$ excitation. The probe detuning is scanned across the $1 \rightarrow 2'$ line to reveal the ac Stark shifted spectrum of that transition. We refer to this method as *quantum jump spectroscopy*.

In this method, resonance fluorescence acts as a high-gain amplifier, scattering many cooler photons for each $1 \rightarrow 2' \rightarrow 2$ Raman transition. The amplification gain depends on properties of the cooler light, magnetic fields, trap geometry, and detection efficiencies, all of which can be held constant as the probe frequency is scanned. In addition, the resonance fluorescence process returns the atom to the $F = 1$ state with an internal and center-of-mass state determined by the resonance fluorescence process, erasing any probe-induced heating or optical pumping. Finally, the $1 \rightarrow 2'$ transition has a very small tensor susceptibility. Together, these features reduce systematic effects relative to earlier methods [6,7,10], leading to an easier data interpretation with more precise results.

To demonstrate intensity measurement by quantum jump spectroscopy, we employ a Maltese cross single atom trap [38,39], in which a magneto-optical trap (MOT) with cooler light red-detuned by $6\gamma_0 \approx 2\pi \times 36$ MHz from the unshifted $2 \rightarrow 3'$ transition is used to load the FORT, and also provides cooler light for the quantum jump spectroscopy. The MOT repumper is stabilized near the $1 \rightarrow 1'$ transition.
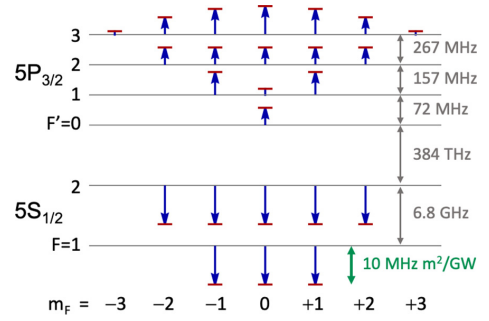

FIG. 2. Level shifts for the D_2 line of ^{87}Rb under linearly polarized illumination at 852 nm, computed as in [9]. Red lines above/below blue arrows show shifted Zeeman sublevels corresponding to the m_F labels below. Blue arrows show the ac Stark shifts per intensity (scale in green at lower right), relative to the unshifted hyperfine levels (grey horizontal lines). Hyperfine level spacings are not to scale.

The FORT light is linearly polarized and stabilized to the Cs D_2 line at 852.1 nm, with an input power of $P_{\rm FORT} = 6.8(2)$ mW, measured with a power meter before the chamber window. The FORT has an intensity at focus, estimated from the input power and beam waist prior to focusing, of $I_{\rm FORT}^{\rm (max)} \approx 1.6 \times 10^9$ W m^{-2} (and thus trap depth $\approx 740\ \mu$K) [38]. As shown in Fig. 2, this implies a light shift of ≈ 20 MHz on the $1 \rightarrow F'$ transitions. We note that the $F' = 2$ state experiences negligible tensor light shifts ($\Delta E_2^{(2)}/h \approx m_F^2 \times 9.5 \times 10^{-4}$ MHz), in comparison with the ones of the $F' = 1$ ($\Delta E_1^{(2)}/h \approx m_F^2 \times 6.63$ MHz) and $F' = 3$ ($\Delta E_3^{(2)}/h \approx m_F^2 \times -2.49$ MHz) states, where m_F is the magnetic quantum number. As a consequence, the transitions to those states are shifted by up to 9.9 MHz, an amount larger that the linewidth of the atomic transition itself. The $1 \rightarrow 2'$ transition frequency thus depends on the atom's position, but negligibly on the atom's internal state.

A circularly polarized probe beam with up to 800 nW of power in a collimated beam with 2 mm $1/e^2$ diameter and tunable over 30 MHz on the blue side of the unshifted $1 \rightarrow 2'$ transition with a double-pass AOM, is sent along the downward vertical direction, copropagating with one of the MOT cooler beams. Fluorescence is collected by three high-numerical-aperture (high-NA) lenses (L_1, L_2 and L_4, henceforth L_i) surrounding the trap center, coupled into single-mode fibers, registered with separate avalanche photodiodes (APDs) and counted in 20 ms time bins.

To acquire fluorescence signals versus probe intensity and versus detuning, we implemented the sequence shown in Fig. 3 (upper): starting from an empty FORT, the MOT beams (cooler and repumper) are turned on to allow an atom to be trapped. Prior to the atom's arrival, the background count rate is recorded.

Arrival of an atom is determined when the detected count in channel L_1 is above 50 photons per bin. After this "trigger" event, repumper and cooler remain on for 60 ms to cool the trapped atom. The repumper is then turned off for 300 ms, leaving cooler and probe on, to record probe-and-cooler
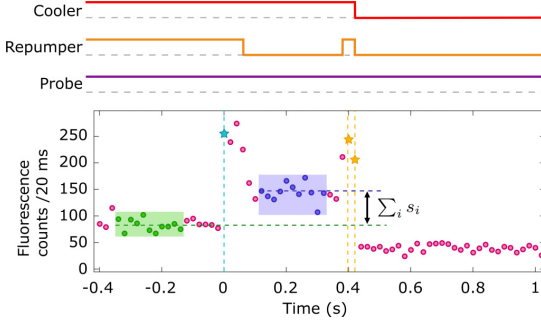
FIG. 3. Sequence and representative fluorescence signal from a single atom. The upper portion shows time sequence of the cooler, repumper, and probe light. Dashed lines indicate the respective zero levels. The lower portion shows observed fluorescence counts in 20 ms bins, obtained by pooling counts from Li collected channels. First detection of an atom in the trap (cyan star) triggers the rest of the sequence, and is taken as the time origin (cyan line). Purple points d_i are used to calculate s_i, the rate of atom fluorescence collected by channel i, green points b_i are used to calculate background due to laser scattering, and counts marked with yellow stars (and yellow lines) are used to verify atom survival.

induced fluorescence. The repumper is then turned on again for 60 ms, to check if the atom is still trapped. The cooler and repumper are then turned off. The atom is allowed to leave by turning off the FORT and cooling beams, and the cycle repeats. The probe is on at constant power and frequency during this whole sequence.

As illustrated in Fig. 3 (lower), we record detections d_i (shown in purple) and background counts b_i (shown in green) from each trapped atom for a total time of 220 ms divided in 11 time bins, where i indicates collection through lens L_i. For any given probe detuning and power, we measure 20 trials like the one shown in Fig. 3. About 65% of the atoms survive. We pool the resulting d_i and b_i values, to have $N \approx 200$ values of each kind.

To extract a signal value and error from these data, we assume b_i and d_i have means c_i and $s_i + c_i$ respectively, where c_i is the mean background rate and s_i is the mean atom scattering collected by each channel. Thus, s_i is estimated as the sample mean of $\{d_i - b_i\}$. We estimate $\sigma_{i,d}^2$ and $\sigma_{i,b}^2$ as the sample variances of $\{d_i\}$ and $\{b_i\}$, from which we estimate $\sigma_{s_i}^2 = \sigma_{i,d}^2 + \sigma_{i,b}^2$. Error estimates are propagated from these variances.

Representative pooled fluorescence signals $\sum_i s_i$ as a function of probe intensity I_{pr} and detuning $\Delta\nu_{pr}$ are shown in Fig. 4. We note that, with ≈ 13 atoms per point (requiring less than 6 s of measurement), the technique resolves detunings in steps of $\gamma_0/2$, where γ_0 is the natural linewidth of the D_2 transition, and also probe intensity differences of order 10 mW m^{-2}, three orders of magnitude below $I_0 = 16.69$ W m^{-2}, the saturation intensity of the D_2 line [40].

The fluorescence signals of Fig. 4 show a saturation with intensity that can be understood as follows: The probe drives the $1 \to 2$ transition with a rate, i.e., probability per unit time, of $R_{1\to2} = P_1 I_{pr}\eta(\nu_{pr})$, where P_F is the probability to be in
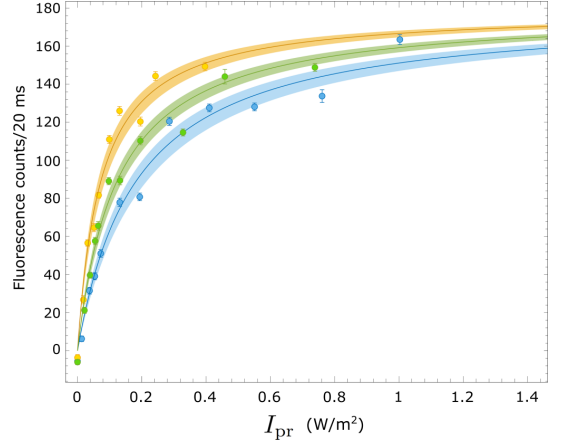

FIG. 4. Collected resonance fluorescence rates as a function of probe intensity I_{pr} and detuning $\Delta\nu_{pr}$. The vertical axis shows the net collected signal $\sum_i s_i$ added over L_i, where $s_i = \langle d_i - b_i \rangle$ is averaged over 11 time bins per atom, acquired in 220 ms (20 ms per time bin), and over 11 to 19 atoms. Upper (orange), middle (green), and lower (blue) curves show detunings $\Delta\nu_{pr} = \gamma_0/2$, γ_0, and $3\gamma_0/2$, respectively, from the frequency $\nu_{1\to2'}$ of the unshifted $1 \to 2'$ transition. Error bars show plus/minus one standard error of the mean. Curves show fits with $\sum_i s_i = \sum_i s_i^{(max)} I_{pr}/(I_{pr} + I_{sat})$, with $\sum_i s_i^{(max)} = 179$ counts/20 ms (found by averaging best-fit values for $\sum_i s_i^{(max)}$ of the individual detunings) and best-fit values $1/I_{sat} = \eta(\nu_{1\to2'} + \Delta\nu_{pr})/\Gamma = 13.6(2.2)$, $8.1(1.0)$, and $5.4(9)$ m^{2}W^{-1} for $\Delta\nu_{pr} = \gamma_0/2$, γ_0 and $3\gamma_0/2$, respectively. Shaded bands show the 95% confidence interval.

state F, I_{pr} is the probe intensity, and $\eta(\nu_{pr})$ is the efficiency of $1 \to 2$ excitation at probe frequency ν_{pr}, i.e., the spectral function we seek to measure. The reverse transition happens with rate $R_{2\to1} = \Gamma P_2$, where Γ depends on the characteristics of the cooler and the $2 \to F'$ transitions, but is independent of the probe.

Defining the saturation power $I_{sat} \equiv \Gamma/\eta(\nu_{pr})$, assuming steady-state, i.e., $R_{1\to2} = R_{2\to1}$, and a fluorescence emission rate $\propto P_2$, the rate of collected fluorescence via the ith channel is

$$s_i = s_i^{(max)} \frac{I_{pr}}{I_{pr} + I_{sat}}, \tag{1}$$

where $s_i^{(max)}$ is the atom's maximum fluorescence rate times the channel's collection efficiency.

To measure the spectral function $\eta(\nu_{pr})$, we first measure fluorescence s_i versus I_{pr} and fit with Eq. (1) to obtain values for $s_i^{(max)}$, as shown in Fig. 4. We then set a probe frequency ν_{pr}, adjust I_{pr} to achieve $s_i/s_i^{(max)} \approx 1/3$ (a condition that minimizes statistical uncertainty in the spectral function), record I_{pr} and s_i for 30 trials, average weighted by $\sigma_{s_i}^{-2}$, and compute $\eta(\nu_{pr}) = I_{sat}^{-1}$ using Eq. (1). Repeating for a range of ν_{pr} we obtain spectra such as that shown in Fig. 5. We note that line broadening due to saturation is automatically compensated in
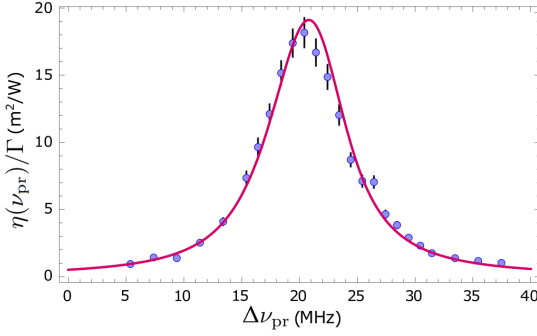
FIG. 5. Quantum jump spectroscopy of the $5S_{1/2}, F = 1 \rightarrow 5P_{3/2}, F' = 2$ transition in individual FORT-trapped atoms. The horizontal axis shows detuning $\Delta\nu_{pr} = \nu_{pr} - \nu_{1\rightarrow 2'}$ from the unshifted $\nu_{1\rightarrow 2'}$ transition frequency. The vertical axis shows excitation efficiency $\eta(\nu_{pr})/\Gamma = I_{sat}^{-1}$ computed via Eq. (1). Sequences in which the atom escapes the trap are excluded in postselection. Each point represents the average of 30 atoms. Error bars indicate plus/minus one standard error. Background counts, measured with no atom in the trap, have been subtracted. Curves show a fit with Eq. (3), with FORT intensity at trap center and atom temperature as free parameters. The fit finds $I_{FORT}^{(max)} = 1.593(5) \times 10^9$ W m^{-2} at trap center and $T = 36.7(8)$ μK, with rms statistical uncertainties found by bootstrapping. These values are in good agreement with independent estimates by physical optics calculation and release-and-recapture temperature measurement, respectively [38].

this method, and that the probe intensity is always well below the $1 \rightarrow 2'$ saturation intensity.

Via light shifts, this spectrum gives information on both the FORT intensity and thus beam shape, and on the atomic center-of-mass spatial distribution and thus atom temperature. If the probe laser instantaneous frequency is ν, and the instantaneous light-shift is $\Delta_{eg} = (\delta_e - \delta_g)I_{FORT}(\mathbf{x})$, where δ_e, δ_g are the per-intensity light shifts of the excited and ground state, respectively, and $\mathbf{x}$ is the instantaneous position of the atom, then the instantaneous efficiency of excitation is

$$\eta \propto f_{nat}(\nu_{eg} + \Delta_{eg} - \nu), \qquad (2)$$

where $\nu_{eg} = (E_e - E_g)/2\pi\hbar$ is the unshifted line center and $f_{nat}(\nu) \propto 1/[(\gamma_0/2)^2 + (2\pi\nu)^2]$ is the natural line shape function. Averaging over the distribution of light shifts $f_\Delta(\Delta_{eg})$, and the probe laser's line-shape function $f_{pr}(\delta)$, with $\delta \equiv \nu - \nu_{pr}$, we obtain

$$\eta(\nu_{pr}) \propto \int d\delta\, d\Delta_{eg}\, f_{nat}(\nu_{eg} + \Delta_{eg} - \nu_{pr} - \delta)f_{pr}(\delta)f_\Delta(\Delta_{eg}), \qquad (3)$$

i.e., the convolution of $f_{nat}(\nu)$ with $f_{pr}(\delta)$ and $f_\Delta(-\Delta_{eg})$.

To relate this to the atom temperature, we note that the optical potential is $V = \alpha\Delta_{eg}$, where $\alpha \equiv 2\pi\hbar\delta_g/(\delta_e - \delta_g)$. Assuming the atom's center-of-mass coordinate is thermally distributed, f_Δ is given by a Boltzmann distribution $f_\Delta \propto \exp[-\beta V]\rho(V)$, where $\beta \equiv 1/k_B T$ and $\rho(V)$ is the potential density of states. If the potential is quadratic with minimum

V_{min}, this gives

$$f_\Delta(\Delta) \propto \sqrt{\alpha\Delta - V_{min}}\, e^{-\beta(\alpha\Delta - V_{min})}\beta^{3/2} \qquad (4)$$

for $\alpha\Delta > V_{min}$, and zero otherwise [41].

The line center reflects the average light shift, which depends strongly on the maximum intensity $I_{FORT}^{(max)} \equiv \max_{\mathbf{x}} I_{FORT}(\mathbf{x})$ and weakly on the temperature T, whereas the line width depends more strongly on T. Fitting the data of Fig. 5, and using a bootstrapping procedure to estimate the fitting uncertainties, we find $I_{FORT}^{(max)} = 1.593(5) \times 10^9$ W m^{-2} and a temperature $T = 36.7(8)$ μK. The reduced χ^2 of this fit is 3.8, which suggests that there are other perturbations roughly comparable to these statistical uncertainties. Relating the obtained value of $I_{FORT}^{(max)}$ with the waist w of the FORT beam, defined as the $1/e^2$ radius of intensity, and assuming the Gaussian beam relation $I_{FORT}^{(max)} = 2P_{FORT}/\pi w^2$ with FORT power $P_{FORT} = 6.8(2)$ mW, the waist is $w = 1.65(2)$ μm, in good agreement with prior estimates [38]. The implied rms width of the center-of-mass distribution is 0.184 μm in the radial directions and 1.58 μm in the longitudinal, so the atom samples the FORT intensity distribution with subwavelength transverse resolution.

Although a full systematic error analysis is beyond the scope of this work, we note that the Zeeman shift of the $1 \rightarrow 2'$ transition is $B(\gamma_{2'}m' - \gamma_1 m)/2\pi$, where B is the magnetic field strength, $\gamma_1/2\pi = -0.7$ MHz G^{-1} and $\gamma_{2'}/2\pi = 0.93$ MHz G^{-1} are the $F = 1$ and $F' = 2$ gyromagnetic ratios, respectively, and m, m' are the corresponding magnetic quantum numbers [40]. The magnitude of the transition shift is thus at most $B \times 2.56$ MHz G^{-1}. The measured magnetic field fluctuations of the laboratory are $B \lesssim 10$ mG [42], implying line shifts and broadening due to Zeeman shifts below 26 kHz. Using a pulsed probe synchronized to the ac power line could reduce this by more than an order of magnitude [42]. Vector light shifts due to elliptically-polarized FORT light can be analyzed similarly. The shift is $\Delta I(\gamma_{2'}^{(opt)}m' - \gamma_1^{(opt)}m)$, where ΔI is the difference in intensity between σ_+ and σ_- polarization components (quantization axis along the FORT propagation direction), and $\gamma_1^{(opt)} = -4.1 \times 10^{-10}$ MHz m^{2}W^{-1} and $\gamma_{2'}^{(opt)} = -1.49 \times 10^{-9}$ MHz m^{2}W^{-1} are the calculated vector light shift coefficients for our FORT wavelength [9]. In our geometry, the circularly polarized probe drives simultaneously the $m' = m$ and $m' = m \pm 1$ transitions in the ratio 2:1:1, implying a transition-averaged shift of at most $\Delta I \times 1.08 \times 10^{-9}$ MHz m^{2}W^{-1}. Assuming $\Delta I = 0.013 \times I_{FORT}^{(max)} = 2.0 \times 10^7$ W m^{-2}, corresponding to the maximum ΔI of a beam with linear polarization extinction ratio 10^5:1, we find a maximum vector light shift of 22 kHz for the transition. For comparison, the 5×10^6 W m^{-2} statistical uncertainty of $I_{FORT}^{(max)}$ corresponds to a scalar transition light shift of 70 kHz. Line broadening is quadratic in the dispersion of such shifts, and is negligible here.

We note possible extensions of the technique: first, the method could be implemented stepwise, with sequential state preparation, probing, and readout. This would remove noise associated with the stochastic $1 \leftrightarrow 2$ jumps in the continuous implementation. Second, circularly or elliptically polarized fields could be measured without state-dependent shifts, if

the atom is optically pumped to a specific $F = 1, m_F$ state [43]. Third, the spectroscopy could be performed with the probe tuned to the $1 \rightarrow 1'$ transition. On this transition, the excitation efficiency will be strongly Zeeman-state and probe-polarization dependent, due to selection rules and strong tensor light shifts of the $F' = 1$ state, as shown in Fig. 2. These features enable internal-state-selective detection with the same advantages of high gain and low perturbation that we have demonstrated using the $1 \rightarrow 2'$ transition.

Conclusion. We have proposed and demonstrated the use of a single neutral ^{87}Rb atom for precision, subwavelength sensing of optical intensity, implemented by a quantum jump spectroscopy technique. A very low intensity probe near the $F = 1 \rightarrow F' = 2$ hyperfine transition of the D_2 line drives "quantum jumps," i.e., resonant Raman transitions, into the $F = 2$ ground state. A second laser near the $F = 2 \rightarrow F' = 3$ cycling transition induces a burst of resonance fluorescence for each Raman transition, greatly amplifying the detectable signal. By scanning the probe frequency, the spectrum of $F = 1 \rightarrow F' = 2$ excitation is measured, indicating the distribution of ac Stark shifts on this transition, which suffers negligible broadening from tensor light shifts. From this spectrum we obtain the intensity at trap center and the atom's temperature.

The technique can be extended to perform Zeeman-state-selective readout.

[1] T. Ruster, H. Kaufmann, M. A. Luda, V. Kaushal, C. T. Schmiegelow, F. Schmidt-Kaler, and U. G. Poschinger, Entanglement-Based dc Magnetometry with Separated Ions, Phys. Rev. X **7**, 031050 (2017).

[2] S. Kotler, N. Akerman, Y. Glickman, A. Keselman, and R. Ozeri, Single-ion quantum lock-in amplifier, Nature (London) **473**, 61 (2011).

[3] M. J. Biercuk, H. Uys, J. W. Britton, A. P. VanDevender, and J. J. Bollinger, Ultrasensitive detection of force and displacement using trapped ions, Nat. Nanotechnol. **5**, 646 (2010).

[4] M. Wahnschaffe, H. Hahn, G. Zarantonello, T. Dubielzig, S. Grondkowski, A. Bautista-Salvador, M. Kohnen, and C. Ospelkaus, Single-ion microwave near-field quantum sensor, Appl. Phys. Lett. **110**, 034103 (2017).

[5] G. R. Guthöhrlein, M. Keller, K. Hayasaka, W. Lange, and H. Walther, A single ion as a nanoscopic probe of an optical field, Nature (London) **414**, 49 (2001).

[6] E. Deist, J. A. Gerber, Y.-H. Lu, J. Zeiher, and D. M. Stamper-Kurn, Superresolution Microscopy of Optical Fields Using Tweezer-Trapped Single Atoms, Phys. Rev. Lett. **128**, 083201 (2022).

[7] C.-Y. Shih and M. S. Chapman, Nondestructive light-shift measurements of single atoms in optical dipole traps, Phys. Rev. A **87**, 063408 (2013).

[8] M. S. Safronova, C. J. Williams, and C. W. Clark, Relativistic many-body calculations of electric-dipole matrix elements, lifetimes, and polarizabilities in rubidium, Phys. Rev. A **69**, 022509 (2004).

[9] S. Coop, S. Palacios, P. Gomez, Y. N. M. de Escobar, T. Vanderbruggen, and M. W. Mitchell, Floquet theory for atomic light-shift engineering with near-resonant polychromatic fields, Opt. Express **25**, 32550 (2017).

[10] A. M. Kaufman, B. J. Lester, C. M. Reynolds, M. L. Wall, M. Foss-Feig, K. R. A. Hazzard, A. M. Rey, and C. A. Regal,

Two-particle quantum interference in tunnel-coupled optical tweezers, Science **345**, 306 (2014).

[11] P. O. Schmidt, T. Rosenband, C. Langer, W. M. Itano, J. C. Bergquist, and D. J. Wineland, Spectroscopy using quantum logic, Science **309**, 749 (2005).

[12] A. H. Myerson, D. J. Szwer, S. C. Webster, D. T. C. Allcock, M. J. Curtis, G. Imreh, J. A. Sherman, D. N. Stacey, A. M. Steane, and D. M. Lucas, High-Fidelity Readout of Trapped-Ion Qubits, Phys. Rev. Lett. **100**, 200502 (2008).

[13] T. Basché, S. Kummer, and C. Bräuchle, Direct spectroscopic observation of quantum jumps of a single molecule, Nature (London) **373**, 132 (1995).

[14] S. Gleyzes, S. Kuhr, C. Guerlin, J. Bernu, S. Deléglise, U. Busk Hoff, M. Brune, J.-M. Raimond, and S. Haroche, Quantum jumps of light recording the birth and death of a photon in a cavity, Nature (London) **446**, 297 (2007).

[15] A. N. Vamivakas, C. Y. Lu, C. Matthiesen, Y. Zhao, S. Fält, A. Badolato, and M. Atatüre, Observation of spin-dependent quantum jumps via quantum dot resonance fluorescence, Nature (London) **467**, 297 (2010).

[16] N. Schlosser, G. Reymond, I. Protsenko, and P. Grangier, Sub-poissonian loading of single atoms in a microscopic dipole trap, Nature (London) **411**, 1024 (2001).

[17] Y.-S. Chin, M. Steiner, and C. Kurtsiefer, Nonlinear photon-atom coupling with 4Pi microscopy, Nat. Commun. **8**, 1200 (2017).

[18] S. A. Aljunid, M. K. Tey, B. Chng, T. Liew, G. Maslennikov, V. Scarani, and C. Kurtsiefer, Phase Shift of a Weak Coherent Beam Induced by a Single Atom, Phys. Rev. Lett. **103**, 153601 (2009).

[19] V. Leong, M. A. Seidler, M. Steiner, A. Cerè, and C. Kurtsiefer, Time-resolved scattering of a single photon by a single atom, Nat. Commun. **7**, 13716 (2016).

[20] A. Asenjo-Garcia, M. Moreno-Cardoner, A. Albrecht, H. J. Kimble, and D. E. Chang, Exponential Improvement in Photon Storage Fidelities Using Subradiance and "Selective Radiance" in Atomic Arrays, Phys. Rev. X **7**, 031024 (2017).

[21] J. Perczel, J. Borregaard, D. E. Chang, H. Pichler, S. F. Yelin, P. Zoller, and M. D. Lukin, Topological Quantum Optics in Two-Dimensional Atomic Arrays, Phys. Rev. Lett. **119**, 023603 (2017).

[22] A. Albrecht, L. Henriet, A. Asenjo-Garcia, P. B. Dieterle, O. Painter, and D. E. Chang, Subradiant states of quantum bits coupled to a one-dimensional waveguide, New J. Phys. **21**, 025003 (2019).

[23] B. J. Lester, Y. Lin, M. O. Brown, A. M. Kaufman, R. J. Ball, E. Knill, A. M. Rey, and C. A. Regal, Measurement-Based Entanglement of Noninteracting Bosonic Atoms, Phys. Rev. Lett. **120**, 193602 (2018).

[24] A. M. Kaufman, B. J. Lester, M. Foss-Feig, M. L. Wall, A. M. Rey, and C. A. Regal, Entangling two transportable neutral atoms via local spin exchange, Nature (London) **527**, 208 (2015).

[25] A. Glicenstein, G. Ferioli, N. Šibalić, L. Brossard, I. Ferrier-Barbut, and A. Browaeys, Collective Shift in Resonant Light Scattering by a One-Dimensional Atomic Chain, Phys. Rev. Lett. **124**, 253602 (2020).

[26] M. Saffman, T. G. Walker, and K. Mølmer, Quantum information with Rydberg atoms, Rev. Mod. Phys. **82**, 2313 (2010).

[27] H. Bernien, S. Schwartz, A. Keesling, H. Levine, A. Omran, H. Pichler, S. Choi, A. S. Zibrov, M. Endres, M. Greiner, V. Vuletić, and M. D. Lukin, Probing many-body dynamics on a 51-atom quantum simulator, Nature (London) **551**, 579 (2017).

[28] H. Labuhn, D. Barredo, S. Ravets, S. de Léséleuc, T. Macrì, T. Lahaye, and A. Browaeys, Tunable two-dimensional arrays of single Rydberg atoms for realizing quantum Ising models, Nature (London) **534**, 667 (2016).

[29] B. M. Spar, E. Guardado-Sanchez, S. Chi, Z. Z. Yan, and W. S. Bakr, Realization of a Fermi-Hubbard Optical Tweezer Array, Phys. Rev. Lett. **128**, 223202 (2022).

[30] J. T. Wilson, S. Saskin, Y. Meng, S. Ma, R. Dilip, A. P. Burgers, and J. D. Thompson, Trapping Alkaline Earth Rydberg Atoms Optical Tweezer Arrays, Phys. Rev. Lett. **128**, 033201 (2022).

[31] S. Burchesky, L. Anderegg, Y. Bao, S. S. Yu, E. Chae, W. Ketterle, K.-K. Ni, and J. M. Doyle, Rotational Coherence Times of Polar Molecules in Optical Tweezers, Phys. Rev. Lett. **127**, 123202 (2021).

[32] W. B. Cairncross, J. T. Zhang, L. R. B. Picard, Y. Yu, K. Wang, and K.-K. Ni, Assembly of a Rovibrational Ground State Molecule in an Optical Tweezer, Phys. Rev. Lett. **126**, 123402 (2021).

[33] L. Caldwell and M. R. Tarbutt, Enhancing Dipolar Interactions between Molecules Using State-Dependent Optical Tweezer Traps, Phys. Rev. Lett. **125**, 243201 (2020).

[34] M. Weyland, S. S. Szigeti, R. A. B. Hobbs, P. Ruksasakchai, L. Sanchez, and M. F. Andersen, Pair Correlations and Photoassociation Dynamics of Two Atoms in an Optical Tweezer, Phys. Rev. Lett. **126**, 083401 (2021).

[35] U. Delic, M. Reisenbauer, D. Grass, N. Kiesel, V. Vuletic, and M. Aspelmeyer, Cavity Cooling of a Levitated Nanosphere by Coherent Scattering, Phys. Rev. Lett. **122**, 123602 (2019).

[36] J. Schäfer, H. Rudolph, K. Hornberger, and B. A. Stickler, Cooling Nanorotors by Elliptic Coherent Scattering, Phys. Rev. Lett. **126**, 163603 (2021).

[37] D. Windey, C. Gonzalez-Ballestero, P. Maurer, L. Novotny, O. Romero-Isart, and R. Reimann, Cavity-Based 3D Cooling of a Levitated Nanoparticle via Coherent Scattering, Phys. Rev. Lett. **122**, 123601 (2019).

[38] L. Bianchet, N. Alves, L. Zarraoa, N. Bruno, and M. Mitchell, Manipulating and measuring single atoms in the Maltese cross geometry, Ver. 2, Open Res. Eur. **1** (2021).

[39] N. Bruno, L. C. Bianchet, V. Prakash, N. Li, N. Alves, and M. W. Mitchell, Maltese cross coupling to individual cold atoms in free space, Opt. Express **27**, 31042 (2019).

[40] D. A. Steck, Rubidium 87 D Line Data, revision 2.2.2, available online at http://steck.us/alkalidata, 9 July 2021.

[41] We note that $f_\Delta \propto \exp[-\beta V]\rho(V)$ depends on V_{min} and on T, but not on derivatives $\partial_i V$ or $\partial_i \partial_j V$, $i, j \in \{x, y, z\}$. This makes the result insensitive to details of the potential shape, provided the temperature is well below the trap depth. We have also performed the analysis assuming $I_{FORT}(\mathbf{x})$ describes an ideal Gaussian beam, and found $I_{FORT}^{(max)}$ and T that agree with the quadratic approximation to within statistical uncertainty.

[42] N. Behbood, F. M. Ciurana, G. Colangelo, M. Napolitano, M. W. Mitchell, and R. J. Sewell, Real-time vector field tracking with a cold-atom magnetometer, Appl. Phys. Lett. **102**, 173504 (2013).

[43] M. K. Tey, Z. Chen, S. A. Aljunid, B. Chng, F. Huber, G. Maslennikov, and C. Kurtsiefer, Strong interaction between light and a single trapped atom without the need for a cavity, Nat. Phys. **4**, 924 (2008).

Bibliography

[1] R. Frisch. Experimenteller nachweis des einstein-schen strahlungsrückstoßes. *Z. Physik*, 86:42–48, 1933. doi:10.1007/BF01340182.

[2] A. Ashkin. Acceleration and trapping of particles by radiation pressure. *Phys. Rev. Lett.*, 24:156–159, Jan 1970. doi:10.1103/PhysRevLett.24.156.

[3] E. L. Raab, M. Prentiss, Alex Cable, Steven Chu, and D. E. Pritchard. Trapping of neutral sodium atoms with radiation pressure. *Phys. Rev. Lett.*, 59:2631–2634, Dec 1987. doi:10.1103/PhysRevLett.59.2631.

[4] W. Paul and M. Raether. Das elektrische massenfilter. *Z. Physik*, 140:262–273, 1955. doi:https://doi.org/10.1007/BF01328923.

[5] H. G. Dehmelt. *Bull. Am. Phys. Soc.*, 7, 1962.

[6] H. G. Dehmelt. *Bull. Am. Phys. Soc.*, 8, 1963.

[7] N. Schlosser, G. Reymond, and I. et al. Protsenko. Sub-poissonian loading of single atoms in a microscopic dipole trap. *Nature*, 411:1024–1027, 2001. doi:10.1038/35082512.

[8] J. Beugnon, M. Jones, and J. et al. Dingjan. Quantum interference between two single photons emitted by independently trapped atoms. *Nature*, 440:779–782, 2006. doi:10.1038/nature04628.

[9] M. P. A. Jones, J. Beugnon, A. Gaëtan, J. Zhang, G. Messin, A. Browaeys, and P. Grangier. Fast quantum state control of a

single trapped neutral atom. *Phys. Rev. A*, 75:040301, Apr 2007. doi:10.1103/PhysRevA.75.040301.

[10] Y. R. P. Sortais, H. Marion, C. Tuchendler, A. M. Lance, M. Lamare, P. Fournet, C. Armellin, R. Mercier, G. Messin, A. Browaeys, and P. Grangier. Diffraction-limited optics for single-atom manipulation. *Phys. Rev. A*, 75:013406, Jan 2007. doi:10.1103/PhysRevA.75.013406.

[11] J. Beugnon, C. Tuchendler, and H. et al. Marion. Two-dimensional transport and transfer of a single atomic qubit in optical tweezers. *Nature Phys*, 3:696–699, 2007. doi:10.1038/nphys698.

[12] Meng Khoon Tey, Zilong Chen, Syed Abdullah Aljunid, Brenda Chng, Florian Huber, Gleb Maslennikov, and Christian Kurtsiefer. Strong interaction between light and a single trapped atom without the need for a cavity. *Nature Phys*, 4:924–927, 2008. doi:https://doi.org/10.1038/nphys1096.

[13] V. Leong, M. Seidler, and M. et al. Steiner. Time-resolved scattering of a single photon by a single atom. *Nat Commun*, 7, 2016. doi:10.1038/ncomms13716.

[14] YS. Chin, M. Steiner, and C. Kurtsiefer. Nonlinear photon-atom coupling with 4pi microscopy. *Nat Commun*, 8, 2017. doi:10.1038/s41467-017-01495-3.

[15] F. Nogrette, H. Labuhn, S. Ravets, D. Barredo, L. Béguin, A. Vernier, T. Lahaye, and A. Browaeys. Single-atom trapping in holographic 2d arrays of microtraps with arbitrary geometries. *Phys. Rev. X*, 4:021034, May 2014. doi:10.1103/PhysRevX.4.021034.

[16] H. Labuhn, D. Barredo, and S. et al. Ravets. Tunable two-dimensional arrays of single rydberg atoms for realizing quantum ising models. *Nature*, 534:667–670, 2016. doi:10.1038/nature18274.

[17] Wolfgang Alt, Dominik Schrader, Stefan Kuhr, Martin Müller, Victor Gomer, and Dieter Meschede. Single atoms in a

standing-wave dipole trap. *Phys. Rev. A*, 67:033403, Mar 2003. doi:10.1103/PhysRevA.67.033403.

[18] M. Martinez-Dorantes, W. Alt, J. Gallego, S. Ghosh, L. Ratschbacher, and D. Meschede. State-dependent fluorescence of neutral atoms in optical potentials. *Phys. Rev. A*, 97:023410, Feb 2018. doi:10.1103/PhysRevA.97.023410.

[19] A. M. Kaufman, B. J. Lester, and C. A. Regal. Cooling a single atom in an optical tweezer to its quantum ground state. *Phys. Rev. X*, 2:041014, Nov 2012. doi:10.1103/PhysRevX.2.041014.

[20] A. M. Kaufman, B. J. Lester, C. M. Reynolds, M. L. Wall, M. Foss-Feig, K. R. A. Hazzard, A. M. Rey, and C. A. Regal. Two-particle quantum interference in tunnel-coupled optical tweezers. *Science*, 345(6194):306–309, 2014. doi:10.1126/science.1250057.

[21] A. Kaufman, B. Lester, and M. et al. Foss-Feig. Entangling two transportable neutral atoms via local spin exchange. *Nature*, 527:208–211, 2015. doi:10.1038/nature16073.

[22] D. Goncalves, M. W. Mitchell, and D. E. Chang. Unconventional quantum correlations of light emitted by a single atom in free space. *Phys. Rev. A*, 104:013724, Jul 2021. doi:10.1103/PhysRevA.104.013724.

[23] Natalia Bruno, Lorena C. Bianchet, Vindhiya Prakash, Nan Li, Natália Alves, and Morgan W. Mitchell. "Maltese cross coupling to individual cold atoms in free space". *Opt. Express*, 27(21):31042–31052, Oct 2019. doi:10.1364/OE.27.031042.

[24] Antoine Glicenstein, Giovanni Ferioli, Ludovic Brossard, Yvan R. P. Sortais, Daniel Barredo, Florence Nogrette, Igor Ferrier-Barbut, and Antoine Browaeys. Preparation of one-dimensional chains and dense cold atomic clouds with a high numerical aperture four-lens system. *Phys. Rev. A*, 103:043301, Apr 2021. doi:10.1103/PhysRevA.103.043301.

[25] Lorena C. Bianchet, Natalia Alves, Laura Zarraoa, Tomas Lamich, Vindhiya Prakash, and Morgan W. Mitchell. Quantum jump spectroscopy of a single neutral atom for precise subwavelength intensity measurements. *Phys. Rev. Research*, 4:L042026, Nov 2022. doi:10.1103/PhysRevResearch.4.L042026.

[26] Dongmin Yu, Han Wang, Jin-Ming Liu, Shi-Lei Su, Jing Qian, and Weiping Zhang. Multiqubit toffoli gates and optimal geometry with rydberg atoms. *Phys. Rev. Appl.*, 18:034072, Sep 2022. doi:10.1103/PhysRevApplied.18.034072.

[27] A. Asenjo-Garcia, M. Moreno-Cardoner, A. Albrecht, H. J. Kimble, and D. E. Chang. Exponential improvement in photon storage fidelities using subradiance and "selective radiance" in atomic arrays. *Phys. Rev. X*, 7:031024, Aug 2017. doi:10.1103/PhysRevX.7.031024.

[28] Harold J. Metcalf and Peter van der Straten. *Laser Cooling and Trapping*. Springer, New York, 2002.

[29] C. J. Foot. *Atomic Physics*. Oxford University Press, Oxford, 2005.

[30] Rudolf Grimm, Matthias Weidemüller, and Yurii B. Ovchinnikov. Optical dipole traps for neutral atoms. 1999. doi:10.48550/ARXIV.PHYSICS/9902072.

[31] Daniel A. Steck. Rubidium 87 d line data. *Available online at http://steck.us/alkalidata*, (revision 2.2.2,9 July 2021).

[32] Daniel A. Steck. *Quantum and Atom Optics*. PhD thesis, available online at http://steck.us/teaching (revision 0.13.16, 23 December 2022).

[33] Simon Coop, Silvana Palacios, Pau Gomez, Y. Natali Martinez de Escobar, Thomas Vanderbruggen, and Morgan W. Mitchell. Floquet theory for atomic light-shift engineering with near-resonant polychromatic fields. *Opt. Express*, 25(26):32550–32559, Dec 2017. doi:10.1364/OE.25.032550.

[34] N. Schlosser, G. Reymond, and P. Grangier. Collisional blockade in microscopic optical dipole traps. *Phys. Rev. Lett.*, 89:023005, Jun 2002. doi:10.1103/PhysRevLett.89.023005.

[35] A. Fuhrmanek, R. Bourgain, Y. R. P. Sortais, and A. Browaeys. Light-assisted collisions between a few cold atoms in a microscopic dipole trap. *Phys. Rev. A*, 85:062708, Jun 2012. doi:10.1103/PhysRevA.85.062708.

[36] L.D. Landau and E.M. Lifshitz. *Statistical Physics: Volume 5*. Number v. 5. Elsevier Science, 2013. ISBN 9780080570464.

[37] Steven Chu, J. E. Bjorkholm, A. Ashkin, and A. Cable. Experimental observation of optically trapped atoms. *Phys. Rev. Lett.*, 57:314–317, Jul 1986. doi:10.1103/PhysRevLett.57.314.

[38] Steven Chu, L. Hollberg, J. E. Bjorkholm, Alex Cable, and A. Ashkin. Three-dimensional viscous confinement and cooling of atoms by resonance radiation pressure. *Phys. Rev. Lett.*, 55:48–51, Jul 1985. doi:10.1103/PhysRevLett.55.48.

[39] P. D. Lett, W. D. Phillips, S. L. Rolston, C. E. Tanner, R. N. Watts, and C. I. Westbrook. Optical molasses. *J. Opt. Soc. Am. B*, 6(11):2084–2107, Nov 1989. doi:10.1364/JOSAB.6.002084.

[40] J. Dalibard and C. Cohen-Tannoudji. Laser cooling below the doppler limit by polarization gradients: simple theoretical models. *J. Opt. Soc. Am. B*, 6(11):2023–2045, Nov 1989. doi:10.1364/JOSAB.6.002023.

[41] Juha Javanainen. Numerical experiments in semiclassical laser-cooling theory of multistate atoms. *Phys. Rev. A*, 46:5819–5835, Nov 1992. doi:10.1103/PhysRevA.46.5819.

[42] P. D. Lett, W. D. Phillips, S. L. Rolston, C. E. Tanner, R. N. Watts, and C. I. Westbrook. Optical molasses. *J. Opt. Soc. Am. B*, 6(11):2084–2107, Nov 1989. doi:10.1364/JOSAB.6.002084.

[43] Wolfgang Ketterle, Alex Martin, Michael A. Joffe, and David E. Pritchard. Slowing and cooling atoms in isotropic laser light. *Phys. Rev. Lett.*, 69:2483–2486, Oct 1992. doi:10.1103/PhysRevLett.69.2483.

[44] J. Dalibard and C. Cohen-Tannoudji. Laser cooling below the doppler limit by polarization gradients: simple theoretical models. *J. Opt. Soc. Am. B*, 6(11):2023–2045, Nov 1989. doi:10.1364/JOSAB.6.002023.

[45] Johan Jersblad, Harald Ellmann, Kristian Støchkel, Anders Kastberg, Laurent Sanchez-Palencia, and Robin Kaiser. Non-gaussian velocity distributions in optical lattices. *Phys. Rev. A*, 69:013410, Jan 2004. doi:10.1103/PhysRevA.69.013410.

[46] Y. Sortais, S. Bize, C. Nicolas, A. Clairon, C. Salomon, and C. Williams. Cold collision frequency shifts in a ^{87}Rb atomic fountain. *Phys. Rev. Lett.*, 85:3117–3120, Oct 2000. doi:10.1103/PhysRevLett.85.3117.

[47] T.W. Hodapp, C. Gerz, and C. et al. Furtlehner. Three-dimensional spatial diffusion in optical molasses. *Appl. Phys. B*, 60:135–143, 1995.

[48] J. Dalibard and C. Cohen-Tannoudji. Dressed-atom approach to atomic motion in laser light: the dipole force revisited. *Journal of the Optical Society of America B*, (11):1707–1720. doi:10.1364/JOSAB.2.001707.

[49] F. Le Kien, P. Schneeweiss, and A. Rauschenbeutel. Dynamical polarizability of atoms in arbitrary light fields: general theory and application to cesium. *European Physical Journal D*, 67:92, May 2013. doi:10.1140/epjd/e2013-30729-x.

[50] Simon Coop, Silvana Palacios, Pau Gomez, Y. Natali Martinez de Escobar, Thomas Vanderbruggen, and Morgan W. Mitchell. Floquet theory for atomic light-shift engineering with near-resonant polychromatic fields. *Optics Express*, 25(26):32550–32559, 2017. doi:10.1364/OE.25.032550.

[51] T. Vanderbruggen and M. W. Mitchell. Near-resonant optical forces beyond the two-level approximation for a continuous source

of spin-polarized cold atoms. *Phys. Rev. A*, page 033410, Mar . doi:10.1103/PhysRevA.87.033410.

[52] M. Martinez-Dorantes. *Fast non-destructive internal state detection of neutral atoms in optical potentials.* PhD thesis, Rheinischen Friedrich Wilhelms Universitaet Bonn, 2016.

[53] M. Tey, Z. Chen, and S. *et al* Aljunid. Strong interaction between light and a single trapped atom without the need for a cavity. *Nature Phys*, 4: 924–927, 2008.

[54] F. Nogrette, H. Labuhn, S. Ravets, D. Barredo, L. Béguin, A. Vernier, T. Lahaye, and A. Browaeys. Single-atom trapping in holographic 2d arrays of microtraps with arbitrary geometries. *Phys. Rev. X*, 4:021034, May 2014. doi:10.1103/PhysRevX.4.021034.

[55] N. Schlosser, G. Reymond, and I. *et al* Protsenko. Sub-poissonian loading of single atoms in a microscopic dipole trap. *Nature*, 411:1024–1027, 2001.

[56] LC Bianchet, N Alves, L Zarraoa, N Bruno, and MW Mitchell. Manipulating and measuring single atoms in the maltese cross geometry [version 1; peer review: 2 approved]. *Open Research Europe*, 1(102), 2021. doi:10.12688/openreseurope.13972.1.

[57] L.C. Bianchet. *A versatile system for the study of light-matter interactions at the level of individual particles.* PhD thesis, 2022.

[58] J. Gallego, W. Alt, T. Macha, M. Martinez-Dorantes, D. Pandey, and D. Meschede. Strong purcell effect on a neutral atom trapped in an open fiber cavity. *Phys. Rev. Lett.*, 121:173603, Oct 2018. doi:10.1103/PhysRevLett.121.173603.

[59] Y. Natali Martinez de Escobar, Silvana Palacios Álvarez, Simon Coop, Thomas Vanderbruggen, Krzysztof T. Kaczmarek, and Morgan W. Mitchell. Absolute frequency references at 1529 and 1560nm using modulation transfer spectroscopy. *Opt. Lett.*, 40(20):4731–4734, Oct 2015. doi:10.1364/OL.40.004731.

[60] D J McCarron, S A King, and S L Cornish. Modulation transfer spectroscopy in atomic rubidium. *Measurement Science and Technology*, 19 (10):105601, aug 2008. doi:10.1088/0957-0233/19/10/105601.

[61] Ducloy, M. and Bloch, D. Theory of degenerate four-wave mixing in resonant doppler-broadened systems - i. angular dependence of intensity and lineshape of phase-conjugate emission. *J. Phys. France*, 42(5):711–721, 1981. doi:10.1051/jphys:01981004205071100.

[62] Silvana Palacios Álvarez. High-coherence light source at 780 nm, for 87rb trapping and cooling experiments. Master's thesis, 2012.

[63] Y. Natali Martinez de Escobar, Silvana Palacios Álvarez, Simon Coop, Thomas Vanderbruggen, Krzysztof T. Kaczmarek, and Morgan W. Mitchell. Absolute frequency references at 1529 and 1560 nm using modulation transfer spectroscopy. *Opt. Lett.*, 40(20):4731–4734, Oct 2015. doi:10.1364/OL.40.004731.

[64] C. Tuchendler, A. M. Lance, A. Browaeys, Y. R. P. Sortais, and P. Grangier. Energy distribution and cooling of a single atom in an optical tweezer. *Phys. Rev. A*, 78:033425, Sep 2008. doi:10.1103/PhysRevA.78.033425.

[65] Yue-Sum Chin, Matthias Steiner, and Christian Kurtsiefer. Polarization gradient cooling of single atoms in optical dipole traps. *Phys. Rev. A*, 96: 033406, Sep 2017. doi:10.1103/PhysRevA.96.033406.

[66] A. M. Kaufman, B. J. Lester, and C. A. Regal. Cooling a single atom in an optical tweezer to its quantum ground state. *Phys. Rev. X*, 2:041014, Nov 2012. doi:10.1103/PhysRevX.2.041014.

[67] Bevington P. R. and Robinson D. K. *Data Reduction and Error Analysis for the Physical Sciences*. McGrawHill, NY, 3rd edition, 2003.

[68] L. D. Landau and E.M. Lifshitz. *Mechanics*. Course of Theoretical Physics. Butterworth-Heinemann, Oxford, 3 edition, 1976.

[69] Vanderlei Bagnato, David E. Pritchard, and Daniel Kleppner. Bose-einstein condensation in an external potential. *Phys. Rev. A*, 35:4354–4358, May 1987. doi:10.1103/PhysRevA.35.4354.

[70] Wolfgang Alt, Dominik Schrader, Stefan Kuhr, Martin Müller, Victor Gomer, and Dieter Meschede. Erratum: Single atoms in a standing-wave dipole trap [phys. rev. a 67, 033403 (2003)]. *Phys. Rev. A*, 71:019905, Jan 2005. doi:10.1103/PhysRevA.71.019905.

[71] Ch. Tsitouras. Runge–kutta pairs of order 5(4) satisfying only the first column simplifying assumption. *Computers Mathematics with Applications*, 62(2):770–775, 2011. ISSN 0898-1221. doi:https://doi.org/10.1016/j.camwa.2011.06.002.

[72] Tey Meng Khoon. *Interfacing Light and a Single Quantum System with a Lens*. PhD thesis, 2008.

[73] Meng Khoon Tey, Gleb Maslennikov, Timothy C H Liew, Syed Abdullah Aljunid, Florian Huber, Brenda Chng, Zilong Chen, Valerio Scarani, and Christian Kurtsiefer. Interfacing light and single atoms with a lens. *New Journal of Physics*, 11(4):043011, apr 2009. doi:10.1088/1367-2630/11/4/043011.

[74] S. Friebel, C. D'Andrea, J. Walz, M. Weitz, and T. W. Hänsch. Co_2-laser optical lattice with cold rubidium atoms. *Phys. Rev. A*, 57:R20–R23, Jan 1998. doi:10.1103/PhysRevA.57.R20.

[75] Jinwei Wu, Raymond Newell, Marc Hausmann, David J. Vieira, and Xinxin Zhao. Loading dynamics of optical trap and parametric excitation resonances of trapped atoms. *Journal of Applied Physics*, 100(5):054903, 2006. doi:10.1063/1.2266164.

[76] Chung-Yu Shih and Michael S. Chapman. Nondestructive light-shift measurements of single atoms in optical dipole traps. *Phys. Rev. A*, 87:063408, Jun 2013. doi:10.1103/PhysRevA.87.063408.

[77] CY Shih. *Characterizing single atom dipole traps for quantum information applications.* PhD thesis, 2013.

[78] L Brossard. *Study of light-induced dipolar interactions in cold atoms assemblies.* PhD thesis, 2020.

[79] Hubert Ammann and Nelson Christensen. Delta kick cooling: A new method for cooling atoms. *Phys. Rev. Lett.*, 78:2088–2091, Mar 1997. doi:10.1103/PhysRevLett.78.2088.

[80] Yue-Sum Chin, Matthias Steiner, and Christian Kurtsiefer. Quantifying the role of thermal motion in free-space light-atom interaction. *Phys. Rev. A*, 95:043809, Apr 2017. doi:10.1103/PhysRevA.95.043809.

[81] N. Trautmann, G. Alber, and G. Leuchs. Efficient single-photon absorption by a trapped moving atom. *Phys. Rev. A*, 94:033832, Sep 2016. doi:10.1103/PhysRevA.94.033832.

[82] A Fuhrmanek, A M Lance, C Tuchendler, P Grangier, Y R P Sortais, and A Browaeys. Imaging a single atom in a time-of-flight experiment. *New Journal of Physics*, 12(5):053028, may 2010. doi:10.1088/1367-2630/12/5/053028.